Published in final edited form as:
J Theor Biol. 2010 June 21; 264(4): 1254–1278. doi:10.1016/j.jtbi.2010.02.036.

Three-Dimensional Multispecies Nonlinear Tumor Growth–II: Tumor Invasion and Angiogenesis

H.B. Frieboes[a,b], **F. Jin**[a,b], **Y.-L. Chuang**[a], **S.M. Wise**[c], **J.S. Lowengrub**[b,d,1], and **V. Cristini**[a,e,f,g,2]

[a]School of Health Information Sciences, The University of Texas Health Science Center, Houston, TX 77054, USA

[b]Mathematics Department, University of California, Irvine, CA 92697-3875, USA

[c]Department of Mathematics, University of Tennessee, Knoxville, TN

[d]Biomedical Engineering Department, University of California, Irvine, CA

[e]Department of Biomedical Engineering, The University of Texas Health Science Center, Houston, TX

[f]Department of Biomedical Engineering, The University of Texas, Austin, TX

[g]Department of Systems Biology, The University of Texas M.D. Anderson Cancer Center, Houston, TX

Abstract

We extend the diffuse interface model developed in Wise et al. (2008) to study nonlinear tumor growth in 3D. Extensions include the tracking of multiple viable cell species populations through a continuum diffuse-interface approach, onset and aging of discrete tumor vessels through angiogenesis, and incorporation of individual cell movement using a hybrid continuum-discrete approach. We investigate disease progression as a function of cellular-scale parameters such as proliferation and oxygen/nutrient uptake rates. We find that heterogeneity in the physiologically complex tumor microenvironment, caused by non-uniform distribution of oxygen, cell nutrients, and metabolites, as well as phenotypic changes affecting cellular-scale parameters, can be quantitatively linked to the tumor macro-scale as a mechanism that promotes morphological instability. This instability leads to invasion through tumor infiltration of surrounding healthy tissue. Models that employ a biologically-founded, multiscale approach, as illustrated in this work, could help to quantitatively link the critical effect of heterogeneity in the tumor microenvironment with clinically observed tumor growth and invasion. Using patient tumor-specific parameter values, this approach may provide a predictive tool to characterize the complex *in vivo* tumor physiological characteristics and clinical response, and thus lead to improved treatment modalities and prognosis.

[1]Corresponding author: lowengrb@math.uci.edu. [2]Corresponding author: Vittorio.Cristini@uth.tmc.edu.

Keywords

cancer; invasion; metastasis; computer simulation; three dimensional model

1 Introduction

Tumor invasion involves an excess of proliferative, anti-apoptotic, and promigratory signals by cancer cells. Collective cell motion (Friedl and Wolf, 2003) emerges from the forces and mechanisms that regulate individual cell motion and synchronization, suggesting that there is more to a tumor than the sum of its parts. An important element is the tumor microvasculature, which tends to be highly disorganized (Hashizume et al., 2000; Jain, 2001a), resulting in considerable heterogeneity in delivery of cell substrates (i.e., oxygen, nutrients, and growth factors) and metabolite removal (Jain, 1988, 1990). This causes acute and chronic hypoxia and acidosis (Vaupel et al., 2001; Höckel et al., 2001; Harris, 2002), both of which correlate with poor clinical outcome and increased risk of metastasis independent of treatment (Höckel et al., 1996, 1999; Brizel et al., 1996, 1997; Sundfor et al., 1998; Erler et al., 2006), may select for tumor cells that are more apoptosis resistant (Graeber et al., 1996; Yu et al., 2002), induce angiogenesis (Harris, 2002; Shweiki et al., 1992; Forsythe et al., 1996), and increase invasiveness (J. et al., 1994; Young et al., 1988; Young and Hill, 1990; Cairns et al., 2001; Postovit et al., 2002; Rofstad and Halsør, 2002; Rofstad et al., 2002; DeJaeger et al., 2001; Gatenby et al., 2006). In turn, both collective (Friedl and Wolf, 2003) and individual cell (Polette et al., 1998; Tester et al., 2000; Putz et al., 1999) migration strategies affect the resulting tissue-scale invasive patterns and metastasis (Friedl and Wolf, 2003; Keller et al., 2006; Sierra, 2005; van Kempen et al., 2003; Wolf and Friedl, 2006; Kopfstein and Christofori, 2006; Yamaguchi et al., 2005; Elvin and Garner, 2005; Sahai, 2005; Friedl, 2004; Friedl et al., 2004; Condeelis et al., 2005; Ridley et al., 2003).

Tumor morphology and invasiveness are also affected by therapeutic intervention. Chemotherapy may select for cells genetically resistant to subsequent treatment by targeting cell species that are sensitive to the drug. The remaining cell population may then aggressively proliferate and migrate without competition for nutrient and oxygen from drug-sensitive cells (Tannock, 2001). Drug therapy may also stimulate tumor morphological instability by non-uniform drug application due to intra-tumoral diffusion gradients, exposing some tumor cells to sub-optimal drug concentrations and thus introducing variability in their therapeutic response (Durand, 2001).

Further, recent studies have found that antiangiogenic therapy, which deprives a tumor of oxygen and nutrients by blocking the formation of neovasculature, can exacerbate hypoxic conditions and lead to increased cell motility. Tumor cohesion is thus decreased and invasiveness is increased. For example, systemic treatment with vascular endothelial growth factor receptor-2 (VEGFR-2) antibody inhibited angiogenesis of glioblastoma (brain tumors) in an animal model and decreased tumor volume, but increased tumor invasion along the host microvasculature (Kunkel et al., 2001). In other cases, anti-angiogenic therapy dramatically increased the number and total area of small satellite tumors clustered around a primary mass (Lamszus et al., 2003; Rubenstein et al., 2000), as shown in Fig. 1, and some of which contained (cuffed) a central core of vessels. In contrast, tumors treated with combined anti-angiogenic/anti-invasive therapy showed a well-defined tumor-host interface and decreased peripheral vessel recruitment (Bello et al., 2004). However, pharmacological cell adhesion inhibitors are being employed in anti-invasive therapy (McLean et al., 2005; Yin et al., 2006; Lockett et al., 2006; Lah et al., 2006; Eble and Haier, 2006; Hayot et al., 2006; Derycke et al., 2005; Huang et al., 2005; Andersen et al., 2005; Bauer et al., 2005)

with inconsistent results (Lah et al., 2006), perhaps partly due to drug-induced plasticity (Friedl and Wolf, 2003; Wolf and Friedl, 2006) (such as an epithelial-to-mesenchymal transition).

Even in an environment where cell substrates are spatially nearly uniform, as in well vascularized regions of tissue, tumor morphological instability may ensue if tumor cell adhesiveness is low (Cristini et al., 2003, 2005; Macklin and Lowengrub, 2007). Tumor invasion may thus occur without recourse to angiogenesis. For example, glioblastoma spheroids *in vitro* surrounded by plentiful nutrients and oxygen were observed to develop sub-spheroids on their peripheral surface, as in Fig. 2 (Frieboes et al., 2006). These sub-spheroids could recursively divide into further sub-spheroids, as predicted by both the two- and three-dimensional simulations in Part I of this paper and previous work (Zheng et al., 2005; Cristini et al., 2005; Macklin and Lowengrub, 2007). The instability seems to be triggered by subsets of tumor cells favored for proliferation by their proximity to cell substrates, which leads to inhomogeneity in the profile of oxygen and nutrients in the microenvironment as well as hypoxic regions in the interior of the tumor.

Tumor morphology may be affected when the tumor cell population undergoes genetic and epigenetic changes. Main gene categories that can affect tumor cell survival and proliferation include oncogenes and tumor suppressor genes. An oncogene may enhance nutrient uptake and cell proliferation while a malfunctioning tumor suppressor gene can affect apoptosis by decreasing the rate of cell death (Benjamin et al., 2003). Such mutations are known to occur in tumors over long periods of time, as cells with these phenotypes are favored for survival (Benjamin et al., 2003). Beyond tumor morphology effects originating in particular genetic and epigenetic changes, however, heterogeneity in cell substrates may also be introduced when a more aggressive subset of cells, existing among other tumor cells, expresses oncogenes or tumor suppressor genes whose collective effect yields an increase in nutrient uptake. This heterogeneity can dramatically affect tumor invasiveness. For example, Fig. 2 shows mammary epithelial cells that have activated the oncogene HER2/neu (encoding the protein ErbB-2, human epidermal growth factor receptor) (Debnath et al., 2002). Here, growth entails a complex morphology in which excess proliferation and luminal filling lead to a tumor mass composed of multiple acinar structures (Debnath and Brugge, 2005). Recent work (Bearer et al., 2009) has quantitatively tied the dramatic effects that heterogeneity in the microenvironment due to genetic and epigenetic changes may have on tumor invasiveness *in vivo*. An important implication is that phenotypic changes affecting proliferation and consumption of cell substrates can introduce sufficient heterogeneity in the microenvironment to dramatically increase morphological instability beyond individual cellular-scale effects, thus driving the cancer to invade even more aggressively.

A key aspect of the complexity of cancer progression and treatment is the coupling of processes occurring across a variety of time and length scales in three physical dimensions. From a modeling perspective, this coupling must be addressed if key tumor dynamics are to be better understood. Although molecular mechanisms and cell-scale migration dynamics are well described, a deeper understanding may be provided by multiscale models that integrate tumor proliferation and invasion with microvascular effects and microenvironmental substrate gradients (e.g., Sinek et al. (2004); Cristini et al. (2005); Anderson et al. (2006); Macklin and Lowengrub (2007); Frieboes et al. (2006, 2007); Gatenby et al. (2007);Macklin et al. (2009); Sinek et al. (2009); Frieboes et al. (2009); Bearer et al. (2009)). This approach could help to quantify and elucidate the links of 3D tumor tissue architecture (e.g., morphology) with growth, invasion, and the underlying phenotypic/microenvironmental characteristics. Building on previous studies (e.g., Byrne and Chaplain (1995, 1996); Seftor et al. (2002); Ambrosi and Preziosi (2002); Alarcón et al. (2003); Araujo and McElwain (2004); Alarcón et al. (2005); Jiang et al. (2005); Ribba et al.

(2006)), multiscale systems modeling complex biological processes such as cancer have been developed. For further reference see the recent reviews by Quaranta et al. (2005); Hatzikirou et al. (2005); Nagy (2005); Abbott et al. (2006); Byrne et al. (2006); Fasano et al. (2006); Roose et al. (2007); Friedman et al. (2007); Sanga et al. (2007); Anderson and Quaranta (2008); Quaranta et al. (2008); Bellomo et al. (2008); Cristini et al. (2008); Deisboeck et al. (2009); Zhang et al. (2009); Lowengrub et al. (2010). In addition, Kim et al. (2007); Stolarska et al. (2009); Bearer et al. (2009); and Lowengrub et al. (2010) have presented frameworks for building multiscale cancer models capable of integrating a hierarchy of processes at varying length and time scales. These latter approaches involve hybrid models combining continuum representation of tumor tissue with individual representations of tumor cells through discrete models.

This is the second paper in a two-part series in which we develop a diffuse interface model of multispecies tumor growth and tumor-induced angiogenesis. In the first paper (Part I, Wise et al. (2008)), we presented simulations of unstable avascular tumor growth in one, two and three dimensions and demonstrated that these techniques now make large-scale three-dimensional simulations of tumors with complex morphologies computationally feasible. This helps to address the modeling challenge of capturing the complexity of the *in vivo* tumor system and its microenvironment in 3D. We focused on tumors consisting of viable and necrotic cells and made several simplifying assumptions regarding the interaction of the cell and host species. This work builds on past studies of multiphase mixture models (Ward and King, 1997; Please et al., 1998; Ward and King, 1999; Please et al., 1999; Breward et al., 2002; Ambrosi and Preziosi, 2002; Breward et al., 2002, [2003]; Byrne et al., 2003; Byrne and Preziosi, 2003; Franks et al., 2003a,[b]; Roose et al., 2003; Araujo and McElwain, 2005a,[b]; Chaplain et al., 2006; Tosin, 2008; Ambrosi and Preziosi, 2009; Ambrosi et al., 2009; Preziosi and Tosin, 2009b,a; Tracqui, 2009) as well as on our multiscale models of tumor growth and angiogenesis (Cristini et al., 2003; Sinek et al., 2004; Zheng et al., 2005; Cristini et al., 2005; Frieboes et al., 2006; Sanga et al., 2006; Li et al., 2007; Frieboes et al., 2007; Sanga et al., 2007; Macklin and Lowengrub, 2007; Macklin et al., 2009; Sinek et al., 2009; Cristini et al., 2009). In the diffuse approach, a continuum model of adhesion is introduced by replacing sharp interfaces with narrow transition layers that arise due to differential adhesive forces among the cell-species (see Part I, Wise et al. (2008)). This approach can more realistically represent tissue interfaces and clonogenic heterogeneity where the physical boundaries between different tissue and cell types may not be well delineated. The model can also describe the dependence of cell-cell and cell-matrix adhesion on cell phenotype and genotype (e.g., expression of E-cadherins and integrins), as well as the dependence on local microenvironmental conditions.

In this paper we study the 3D nonlinear coupling between multispecies tumor invasion and tumor-induced angiogenesis. We examine the effect of variable cell-cell adhesion due to changes in cell phenotype and microenvironmental conditions (e.g., oxygen levels), and focus on the morphological instabilities that may underlie invasive phenotypes. In addition, we incorporate a discrete description of individual cells in the continuum model to develop a hybrid continuum-discrete approach capable of describing transitions from collective to individual behavior, and vice-versa. Specifically, we investigate: *(i)* effects of cell substrate gradients in the 3-D microenvironment, *(ii)* effects of cells consuming oxygen/nutrient and proliferating at different rates, as occurs due to phenotypic variation and application of drug therapy, and *(iii)* effects of cell chemotaxis (cell migration up gradients of soluble chemical factors), as may occur due to local depletion of cell substrates. We take model parameters to be consistent with glioblastoma growth (Zheng et al., 2005; Frieboes et al., 2006), which is known to be highly invasive.

In the avascular growth stage, linking the effect of cell substrate gradients to the tumor scale, the model predicts the resulting morphological instability to be in the form of clusters growing off the main tumor mass (Frieboes et al., 2006), e.g., as observed experimentally for human brain cancer in Fig. 2. Under vascularized conditions, the simulation results suggest that a tumor may undergo an even more dramatic instability (Sinek et al., 2004; Zheng et al., 2005; Cristini et al., 2005; Frieboes et al., 2007; Sinek et al., 2009; Bearer et al., 2009) than that encountered *in vitro*. The model predicts the *in vivo* instability to be in the form of elongation and growth of invasive fingers of tumor cells infiltrating the nutrient-rich areas of the host tissue, in agreement with clinical observations (Bearer et al., 2009). In both avascular and vascular scenarios, the model postulates that cell adhesion has a key role in the wave-length and magnitude of the morphological instability. The incorporation of transitions from collective to individual cell behavior under hypoxic conditions in the model may lead to palisading cells (i.e., moving in “single file”) from hypoxic to normoxic regions, consistent with clinical observations Bearer et al. (2009), and to the development of complex, multifocal tumor morphologies (e.g., Rubenstein et al. (2000)).

This paper is organized as follows. In §2 we summarize the diffuse interface model of Wise et al. (2008); please refer to Part I for the full description. In §3 we describe the modeling of the three-dimensional tumor vasculature created through angiogenesis. In §4 we present a hybrid continuum-discrete scheme to simulate individual cell migration while maintaining a continuum description for the bulk tumor. In §5 we investigate the effects of varying degrees of oxygen/nutrient uptake, proliferation, and chemotaxis on cell substrate heterogeneity, tumor morphology, and invasion. This is achieved in part by modeling a tumor cell population containing two different phenotypes. In §6 we summarize the results and discuss future work.

2 Diffuse Interface Model

In this section we summarize the non-dimensional model from Wise et al. (2008) and simplify it to consider two viable tumor cell species. We extend the model to take into account the effects of chemotaxis.

2.1 Mass conservation

The dependent variables in a (N + 1)-species model are:

- the volume fractions of the water, tumor and host cell species, $\phi_0, \ldots, \phi_N$,
- the densities of the components $\rho_0, \ldots, \rho_N$,
- the extra-cellular fluid pressure q,
- the cell-to-cell (solid) pressure p, and
- the component velocities $\mathbf{u}_0, \ldots, \mathbf{u}_N$.

It is assumed that there are no voids (i.e., the mixture is saturated) and thus $\sum_{i=0}^{N} \phi_i = 1$. Further, it is assumed that the densities are constant, i.e., independent of temperature, pressure, etc. Without loss of generality,

- $i = 0$ is identified as the water fluid component
- $i = 1..N - 1$ are identified as the tumor species components
- $i = N$ is identified as the host cell component

The volume fractions of the components are assumed to be continuous in a domain Ω, which contains both the tumor and host domains. The volume fractions obey the mass conservation (advection-reaction-diffusion) equations

$$\rho_i \left(\frac{\partial \phi_i}{\partial t} + \nabla \cdot (\mathbf{u}_i \phi_i) \right) = - \nabla \cdot \mathbf{J}_i + S_i, \tag{1}$$

where $\mathbf{J}_i$ are fluxes that account for the mechanical interactions among the cell species. The source terms S_i account for inter-component mass exchange as well as gains due to proliferation of cells and loss due to cell lysing.

The density of the mixture is defined as $\rho = \sum_{i=0}^{N} \rho_i \phi_i$. The mass averaged velocity of the mixture is then defined as $\mathbf{u} = 1/\rho \sum_{i=0}^{N} \rho_i \phi_i \mathbf{u}_i$. Summing Eq. (1), the mass of the mixture is conserved only if

$$0 = \sum_{i=0}^{N} \mathbf{J}_i = \sum_{i=0}^{N} S_i. \tag{2}$$

These conditions are posed as consistency constraints for the fluxes and sources. Note that $\sum_{i=0}^{N} \mathbf{J}_i$ could be taken as constant; without loss of generality, this constant is chosen as zero.

2.2 Adhesion energy

To motivate the constitutive laws for the fluxes $\mathbf{J}_i$ and the velocities $\mathbf{u}_i$, an energy of each component E_i is introduced that includes the effects to be considered. To describe the energy associated with the interactions among the different components, an approach from continuum thermodynamics (e.g., see Rowlinson and Widom (1982); Landau (1984)) is followed that introduces the Helmholtz free energy of component interactions (e.g. adhesion). As explained in Wise et al. (2008), the following weakly nonlocal model of the Helmholtz free energy of the i^{th} component can be obtained:

$$E_i = \int \left(F_i(\phi_0, \ldots \phi_N) + \sum_{j=0}^{N} \frac{\bar{\varepsilon}_{ij}^2}{2} |\nabla \phi_j|^2 \right) d\mathbf{x}, \tag{3}$$

where the first term models the bulk energy of the components due to local interactions while the second (gradient energy) term models longer range interactions among the components. Here, $\bar{\varepsilon}_{ij}$ are non-negative constants, such that $\bar{\varepsilon}_{ij}^2$ has units of energy per unit length. The total energy is then $E = \sum_i E_i$. We note that Armstrong et al. (2006), and later Gerisch and Chaplain (2008), considered a nonlocal model of adhesion in related work.

2.3 Constitutive laws for fluxes and velocities

We assume that the volume fraction of water is constant in time and space, which means that the volume fraction of the solid components is also constant, i.e., $\sum_{i=1}^{N} \phi_i = \phi_S$. As indicated in Part I, thermodynamically consistent fluxes may be taken to be as in the generalized Fick's law (Wise et al., 2008):

$$\mathbf{J}_i = -\bar{M}_i \nabla\left(\frac{\delta E}{\delta \phi_i} - \frac{\delta E}{\delta \phi_N}\right), 1 \le i < N-1, \tag{4}$$

and $\mathbf{J}_N = -\sum_{i=1}^{N-1} \mathbf{J}_i$. Mobility $\bar{M}_i > 0$, and $\frac{\delta E}{\delta \phi_i}$ are variational derivatives of the total energy E given by

$$\frac{\delta E}{\delta \phi_i} = \sum_{j=0}^{N}\left(\frac{\partial F_j}{\partial \phi_i} - \nabla \cdot (\bar{\varepsilon}_{ji}^2 \nabla \phi_i)\right), 1 \le i < N. \tag{5}$$

The resulting generalized Darcy laws for the velocities of the components are

$$\mathbf{u}_0 = -\bar{k}_0 \nabla\left(\frac{\delta E}{\delta \phi_0} + q\right), \tag{6}$$

$$\mathbf{u}_i = -\bar{k}\left(\nabla p - \sum_{j=1}^{N} \frac{\delta E}{\delta \phi_j} \nabla \phi_j\right) - \bar{k}_i \nabla\left(\frac{\delta E}{\delta \phi_i} - \frac{1}{\phi_S^{\sim} \sum_{j=1}^{N} \phi_j \frac{\delta E}{\delta \phi_j} + \frac{p}{\phi_S^{\sim}}}\right), i = 1..N, \tag{7}$$

where q is the water pressure and p is the solid pressure. The terms dependent on $\delta E/\delta \phi_j$ represent the excess force due to adhesion and arise from cell-cell and cell-host interactions. The coefficients $\bar{k}_0$, $\bar{k}$, and $\bar{k}_i$ are positive definite motility matrices, reflecting the response of the water and cell species, respectively, to pressure gradients. These motilities contain the combined effects of cell-cell and cell-matrix adhesion.

The constitutive laws (4), (6), and (7) guarantee that in the absence of mass sources, the adhesion energy is non-increasing in time as the fields evolve.

2.4 Model simplification

The model may be simplified by assuming that tumor cells prefer to adhere to one another rather than to the host, and that no distinction is made between the adhesive properties of the viable and dead cells. Accordingly, in Eq. (3), the total energy is taken to be:

$$E = \sum_{i=0}^{N} E_i = \int_{\Omega} \left(f(\phi_T) + \frac{\bar{\varepsilon}^2}{2} |\nabla \phi_T|^2\right) d\mathbf{x}, \tag{8}$$

where f is a double-well bulk energy with minima at $\phi_T = \tilde{\phi}_S$ and $\phi_T = 0$, giving rise to a well-delineated phase separation of the tumor ($\phi_T \approx \phi_S$) and host tissues ($\phi_T \approx 0$). The energy density f may be written as the difference of the two convex functions

$$f(\phi_T) = f_c(\phi_T/\phi_S^{\sim}) - f_e(\phi_T/\phi_S^{\sim}). \tag{9}$$

For example, we may take

$$f_c(\phi)=\alpha_1\left((\phi-1/2)^4+1\right) \text{ and } f_e(\phi)=\alpha_2(\phi-1/2)^2, \tag{10}$$

where α_1 and α_2 are functions of an overall energy scale $\bar{E} > 0$ that describe the strength of adhesion (attraction) of tumor cells to the host tissue and to each other, respectively. Note that the adhesive properties between the tumor cells and the host may be changed by varying the values of α_1 and α_2. For example, if $\alpha_2 = 0$ then the adhesion between the host and the tumor would lead to diffusion-like spread of tumor cells into the surrounding microenvironment.

From the flux constitutive Eq. (4) and the adhesion energy Eq. (8), the adhesion fluxes may be determined. Recalling that the densities of the components are matched, and taking the mobilities $\bar{M}_i = \bar{M}\phi_i$, where $\bar{M}$ is a positive constant, the fluxes become (Wise et al., 2008):

$$\mathbf{J}_i=-\bar{\mathrm{M}}\phi_i\nabla\frac{\delta E}{\delta\phi_i}, 1\le i<N-1 \tag{11}$$

where it is used that the energy does not depend explicitly on ϕ_N. The terms $\delta E/\delta\phi_i$ are given by

$$\mu=\frac{\delta E}{\delta\phi_i}=\frac{\delta E}{\delta\phi_\mathrm{T}}=f'(\phi_\mathrm{T})-\bar{\varepsilon}^2\nabla^2\phi_\mathrm{T}, \tag{12}$$

where it is used that $\phi_\mathrm{T}=\sum_{i=1}^{N-1}\phi_i$.

From the velocity constitutive equation Eq. (7) and the adhesion energy Eq. (8), the component velocities are:

$$\mathbf{u}_0=-\bar{\mathrm{k}}_0\nabla q, \tag{13}$$

$$\mathbf{u}_i=-\left(\bar{\mathrm{k}}+\frac{\bar{\mathrm{k}}_i}{\phi_\mathrm{S}}\right)\left(\nabla p-\frac{\delta E}{\delta\phi_\mathrm{T}}\nabla\phi_\mathrm{T}\right)-\bar{\mathrm{k}}_i\frac{\phi_\mathrm{N}}{\phi_\mathrm{S}\nabla\frac{\delta E}{\delta\phi_\mathrm{T}}}, \tag{14}$$

$$\mathbf{u}_\mathrm{N}=-\left(\bar{\mathrm{k}}+\frac{\bar{\mathrm{k}}_\mathrm{N}}{\phi_\mathrm{S}}\right)\left(\nabla p-\frac{\delta E}{\delta\phi_\mathrm{T}}\nabla\phi_\mathrm{T}\right)+\bar{\mathrm{k}}_\mathrm{N}\frac{\phi_\mathrm{T}}{\phi_\mathrm{S}\nabla\frac{\delta E}{\delta\phi_\mathrm{T}}}, \tag{15}$$

where it is used that the energy does not explicitly depend on ϕ_0 and ϕ_N and $1 \le i < N - 1$.

As a further simplifying assumption, we take the host and cell motilities to be $\bar{k}_i = \bar{k}_N = 0$ which is consistent with assuming the cells are tightly packed and that they move together. Consequently, defining the velocity of the solid components to be

$$\mathbf{u}_S = -\bar{k}\left(\nabla p - \frac{\delta E}{\delta \phi_T}\nabla \phi_T\right), \tag{16}$$

$\mathbf{u}_i = \mathbf{u}_N = \mathbf{u}_S$ is obtained. Note that the motility $\bar{k} > 0$ may be a function of ϕ_i and other variables. In particular, if $\bar{k} = \bar{k}(\phi_i)$, the individual components may respond to the pressure and adhesive forces differently, but mixtures of the components will tend to move together.

The constitutive choices (11), (13), and (16) guarantee that in the absence of mass sources, the adhesion energy is non-increasing as the fields evolve, while the total tumor mass is conserved.

2.5 Mass exchange terms

2.5.1 Tumor Cell Species—We identify two viable and one dead tumor cell species in the general framework described above. The species are labeled, respectively, by the subscripts *V* (original viable phenotype), *M* (mutated viable phenotype, derived from the original species), and *D* (dead, derived from both viable species). The species *M* represents a phenotypic change, which could be of genetic or epigenetic in origin (here, we loosely use the term "mutation" to generically denote this change). The corresponding source terms in Eq. (1) are then defined:

$$S_V = \bar{\lambda}_V^m n\phi_V - \bar{\lambda}_V^a \phi_V - \bar{\lambda}_V^n \mathcal{H}(n_V^* - n)\phi_V - \mathcal{M}^{V\to M}(\phi_V) \tag{17}$$

$$S_M = \bar{\lambda}_M^m n\phi_M - \bar{\lambda}_M^a \phi_M - \bar{\lambda}_M^n \mathcal{H}(n_M^* - n)\phi_V + \mathcal{M}^{V\to M}(\phi_V) \tag{18}$$

$$S_D = \bar{\lambda}_V^a \phi_V + \bar{\lambda}_M^a \phi_M + \bar{\lambda}_V^n \mathcal{H}(n_V^* - n)\phi_V + \bar{\lambda}_M^n \mathcal{H}(n_M^* - n)\phi_M - \bar{\lambda}_D^l \phi_D, \tag{19}$$

$$S_T = S_V + S_M + S_D = \bar{\lambda}_V^m n\phi_V + \bar{\lambda}_M^m n\phi_M - \bar{\lambda}_D^l \phi_D, \tag{20}$$

where ϕ_V, ϕ_M, ϕ_D and ϕ_T are the volume fractions of original viable species, mutated viable species, dead species, and total tumor species, respectively. The dead species includes tumor tissue that has undergone apoptosis or necrosis. Dead species are assumed not to consume cell substrates. The rate constants for the original viable species are $\bar{\lambda}_V^m, \bar{\lambda}_V^a, \bar{\lambda}_V^n$, denoting mitosis, apoptosis and necrosis, and are $\bar{\lambda}_M^m, \bar{\lambda}_M^a, \bar{\lambda}_M^n$ for the mutated species.

The source terms S_V and S_M quantitatively specify tumor volume change of each viable phenotype due to mitosis, apoptosis, and necrosis. Both species proliferate proportionally to the level *n* of substrate concentration, generically representing the concentration of cell substrates (oxygen, glucose, growth factors), and both species undergo necrosis when the *n* drops below a certain threshold (n_V^* for the original and n_M^* for the mutated species). $\mathcal{H}(x)$ is the modified Heaviside function, $\mathcal{H}(x) = xH(x)$, activated as the level of *n* drops below the cell viability threshold specific to each phenotype. Dead species accumulate from apoptosis and necrosis by both viable species, and transition into water with a rate constant $\bar{\lambda}_D^l$.

$\mathcal{M}^{V\to M}$ is a transfer function modeling the mutation of the original to the mutated viable species (Section 2.8).

2.5.2 Cell substrates—In the host, the net cell substrate uptake is negligible compared to the uptake by tumor cells; thus, the host tissue is modeled at equilibrium as a first approximation. Substrates uptaken by the host tissue are assumed to be replaced by supply from the normal vasculature. This may not be the case in the tumor, where not only the uptake exceeds the supply, but the uptake may also be higher than that of the host (Ramanathan et al., 2005; Esteban and Maxwell, 2005). Hence, the diffusion equation for the cell substrate concentration n is:

$$\frac{\partial n}{\partial t}=\nabla\cdot\left(\bar{\mathrm{D}}\left(\phi_{\mathrm{T}}\right)\nabla n\right)+\bar{\mathrm{T}}_{\mathrm{source}}, \tag{21}$$

where $\bar{D}$ is the diffusion coefficient. This coefficient can be different in the host (D_H) and tumor (D_T) domains:

$$\bar{\mathrm{D}}(\phi_{\mathrm{T}})=\bar{\mathrm{D}}_{\mathrm{H}}(1-Q\left(\phi_{\mathrm{T}}/\bar{\phi}_{\mathrm{S}}\right))+\bar{\mathrm{D}}_{\mathrm{T}}Q\left(\phi_{\mathrm{T}}/\bar{\phi}_{\mathrm{S}}\right), \tag{22}$$

where Q is an interpolation function such that $Q(0) = 0$ and $Q(1) = 1$. Here, $Q(x) = x^2(3 - 2x)$.

The source term $\bar{T}_{source}$ includes uptake and supply of cell substrates:

$$\bar{\mathrm{T}}_{source}=\bar{\mathrm{T}}_{uptake}+\bar{\mathrm{T}}_{supply} \tag{23}$$

The substrate uptake for both viable tumor species is given by

$$\bar{\mathrm{T}}_{uptake}=\sum_{i}-\bar{\nu}_{i}^{\mu}n\phi_{i}/\bar{\phi}_{S}=-\bar{\nu}_{V}^{\mu}n\phi_{V}/\bar{\phi}_{S}-\bar{\nu}_{M}^{\mu}n\phi_{M}/\bar{\phi}_{S}, \tag{24}$$

where $\bar{\nu}_{V}^{\mu}$ and $\bar{\nu}_{M}^{\mu}$ are the corresponding uptake rates.

Due to the presence of a capillary network in the tumor and host tissues, a supply of cell substrates is incorporated as in (Cristini et al., 2003; Zheng et al., 2005; Frieboes et al., 2007; Macklin et al., 2009). $\bar{T}_{supply}$ is the capillary-to-tissue transfer function and may vary depending on the differences in cell substrate and pressure levels between the capillaries and the surrounding tissue. For the capillary-to-tissue transfer, the simple model is used

$$\bar{\mathrm{T}}_{supply}=\bar{\nu}_{ves}\phi_{ves}\mathscr{P}\left(p_{ves}\right)\left(\bar{\mathrm{n}}_{\mathrm{C}}-n\right) \tag{25}$$

where $\bar{\nu}_{ves}$ is the cell substrate supply rate coefficient, ϕ_{ves} is the density of the vasculature network, $\bar{n}_C$ is the substrate concentration in the capillaries, and $\mathscr{P}(p)$ is the dependency of the substrate supply on the pressure p of the tumor tissue on the vessel, i.e., $\mathscr{P}(p_{ves}) = (p_{crush} - p)_+$ (taking the positive part) and p_{crush} is the threshold pressure for cell substrate exchange from the capillaries. Although in the simulations herein $\mathscr{P} = 1$, the effect of substrate delivery impairment is considered as part of the vessel shutdown due to pressure from tumor cell proliferation (Section 3.4). The density of the vasculature network ϕ_{ves} can be further divided into the preexisting and tumor-induced capillaries

$$\phi_{ves}=\phi_{ves\_pre}+\phi_{ves\_angio}. \quad (26)$$

($\bar{T}_{supply}$ was $\bar{T}_C$ in Eq. (39) in Part I). For simplicity, the preexisting capillary network may be both in the tumor and the host,

$$\phi_{ves\_pre}=\bar{\phi}^{N}_{ves\_pre}(1-Q(\phi_T/\phi_S))+\bar{\phi}^{T}_{ves\_pre}Q(\phi_T/\phi_S) \quad (27)$$

where $\bar{\phi}^{N}_{ves\_pre}$ and $\bar{\phi}^{T}_{ves\_pre}$ are the preexisting capillary density in the host and tumor domains, respectively. The function ϕ_{ves_angio} prescribes the density of the tumor-induced vasculature (Section 3.5).

2.5.3 Extracellular matrix—As discrete tumor cells (see Section 4) and vascular endothelial cells (see Section 3) migrate through the extracellular matrix (ECM), they release matrix-degrading enzymes (MDEs) that degrade the ECM, thereby releasing matrix macro-molecules such as fibronectin. The cells also remodel the ECM by producing these molecules. These proteins are used as a chemical factor in the haptotaxis (i.e., motion up gradients of bound matrix proteins) by tumor cells invading the host, as well as by endothelial tip cells moving towards the tumor. MDEs may also be released by trailing endothelial cells but we do not model this here. The change in time of the fibronectin concentration f can be modeled by the following simple equation:

$$\frac{\partial f}{\partial t}=-R_f m f+R_{f,tumor}\sum_{i=1}^{N-1}\phi_i+R_{f,ves}\phi_{tip} \quad (28)$$

where R_f is a non-negative degradation rate constant, m is the MDE concentration, and $R_{f,tumor}$ and $R_{f,ves}$ are production rate constants by viable tumor and endothelial tip cells, respectively. ϕ_{tip} is the subset of ϕ_{ves_angio} (Eq. 26) representing the leading endothelial cells at the tip of the capillaries induced by angiogenesis.

The MDEs are produced by tumor and endothelial cells, diffuse through the tissue, and decay. The equation governing this evolution is given by:

$$\frac{\partial m}{\partial t}=\nabla\cdot(D_m\nabla m)+R_{m,tumor}\sum_{i=1}^{N-1}\phi_i+R_{m,ves}\phi_{tip}-R_m m \quad (29)$$

where D_m is the diffusion coefficient, $R_{m,tumor}$ and $R_{m,ves}$ are the MDE generating rate constants for viable tumor and endothelial cells, respectively, and R_m is the positive decay rate constant (assumed to be the same for both tumor and endothelial cells).

Although the rate constants $R_{f,tumor}$ and $R_{m,tumor}$ are assumed equal for all viable tumor species, they could easily be specified differently in the equations above.

2.6 Nondimensional equations

Space and time are nondimensionalized using the diffusion length and mitosis time scales (Cristini et al., 2003):

$$\mathscr{L}=(\bar{D}_T/\bar{\nu}_U)^{\frac{1}{2}} \text{ and } \mathscr{T}=\bar{\lambda}_M^{-1}, \tag{30}$$

and the characteristic tumor pressure is introduced

$$\bar{p}_T=\mathscr{L}^2\frac{\bar{\lambda}_M}{\bar{k}}, \tag{31}$$

where $\bar{k}$ is a characteristic value of the motility k. The field variables are made dimensionless by the replacements as indicated in Wise et al. (2008). In particular, the solid volume fractions are now bounded above by 1 (for solid components, $\phi_i = \phi_i/\bar{\phi}_S$). See Wise et al. (2008) for definitions of the nondimensional parameters.

We solve for the volume fractions of the total tumor ϕ_T, mutated viable ϕ_M, and dead ϕ_D cell species (the host and original viable cell species may be recovered by $\phi_H = 1-\phi_T$ and $\phi_V = \phi_T-\phi_D-\phi_M$, respectively). The nondimensional equations are given as follows:

$$\frac{\partial\phi_T}{\partial t}=M\nabla\cdot(\phi_T\nabla\mu)+S_T-\nabla\cdot(\mathbf{u}_S\phi_T), \tag{32}$$

$$\mu=f'(\phi_T)-\varepsilon^2\nabla^2\phi_T, \tag{33}$$

$$S_T=S_V+S_M+S_D=\left((\lambda_V^m\phi_V+\lambda_M^m\phi_M)n-\lambda_D^l\phi_D\right)Q^*(\phi_T), \tag{34}$$

where the notation $\mu = \delta E/\delta\phi_T$ denotes the cell-chemical potential.

When ε is sufficiently small, $Q^*(\phi_T) = 1$. When ε is large, cells may escape from the primary tumor; the cutoff function $Q^*(\phi_T)$ prevents spurious tumor growth that may be caused by these cells. Here, $Q^*(\phi_T) = Q(\phi_T)/\phi_T$.

The nondimensional equation for the volume fraction of dead cells is

$$\frac{\partial\phi_D}{\partial t}=M\nabla\cdot(\phi_D\nabla\mu)+S_D-\nabla\cdot(\mathbf{u}_S\phi_D), \tag{35}$$

$$S_D=((\lambda_V^a+\lambda_V^n\mathscr{H}(n_V^*-n))\phi_V+(\lambda_M^a+\lambda_M^n\mathscr{H}^*(n_M^*-n))\phi_M-\lambda_D^l\phi_D)Q^*(\phi_T) \tag{36}$$

The nondimensional equation for the volume fraction of the mutated viable cell species is

$$\frac{\partial\phi_M}{\partial t}=M\nabla\cdot(\phi_M\nabla\mu)+S_M-\nabla\cdot(\mathbf{u}_S\phi_M), \tag{37}$$

$$S_M = \left(\lambda_M^m n\phi_M - \lambda_M^n \mathscr{H}(n_M^* - n)\phi_M + \mathscr{M}^{V\to M}(\phi_V)\right) Q^*(\phi_T), \tag{38}$$

The nondimensional cell velocity is

$$\mathbf{u}_S = -k(\phi_j)\left(\nabla p - \frac{\tilde{\gamma}}{\varepsilon}\mu\nabla\phi_T\right), \tag{39}$$

where $\tilde{\gamma}$ is a nondimensional measure of the adhesion force (in our simulations, we set $k(\phi_j) = 1$). The velocity is constrained to satisfy

$$\nabla \cdot \mathbf{u}_S = S_T. \tag{40}$$

Together, Eqs. (39) and (40) constitute a Poisson equation for the pressure p:

$$-\nabla\cdot(k(\phi_j)\nabla p) = S_T - \nabla\cdot\left(k(\phi_T,\phi_D)\frac{\tilde{\gamma}}{\varepsilon}\mu\nabla\phi_T\right). \tag{41}$$

Knowing the pressure p, $\mathbf{u}_S$ can be calculated using Eq. (39).

The non-dimensional cell substrate equation is

$$0 = \nabla\cdot(D(\phi_T)\nabla n) + T_{uptake} + T_{supply}, \tag{42}$$

where it is used that cell substrate diffusion occurs on a much shorter time scale (e.g., minutes) than cell-proliferation (e.g., day) in Eq. (21). The diffusion coefficient and angiogenesis source are

$$D(\phi_T) = D_H(1 - Q(\phi_T)) + Q(\phi_T), \tag{43}$$

$$T_{uptake} = (-\nu_V^\mu\phi_V + \nu_M^\mu\phi_M)n) \tag{44}$$

$$T_{suppply} = \nu_{ves}\phi_{ves}\mathscr{P}(p)(n_C - n) \tag{45}$$

The interpolated diffusivity in Eq. (43) is appropriate when D_H is comparable to 1. If on the other hand $D_H \ll 1$ or $D_H \gg 1$, then it may be necessary to use another interpolation. ϕ_{ves} is the effective vascular density of the cell substrate delivering vessels (see Eq. (62) below).

Equations (32)–(45) are valid throughout Ω and not just on the tumor volume Ω_T. Note that no boundary conditions are required for ϕ_T or ϕ_D at the tumor boundary $\sum_T$. For outer boundary conditions (on $\sum_\infty$), we choose

$$\mu = 0, n = 1, p = 0, \tag{46}$$

$$\zeta_\infty \cdot \nabla_{\phi\Gamma} = \zeta_\infty \cdot \nabla_{\phi D} = \zeta_\infty \cdot \nabla p = 0, \tag{47}$$

where ζ_∞ is the outward-pointing unit normal on the outer boundary $\sum_\infty = \partial\Omega$. The boundary conditions $\mu = 0$ and $p = 0$ allow for the free flow of cells across this boundary.

2.7 Chemotaxis

In order to maintain homeostasis when the local concentration of oxygen or nutrient is sub-optimal, tumor cells may develop a migratory phenotype that enables relocalization to regions of higher cell substrates within the tumor (i.e., regions that are better vascularized). The rate of cell proliferation is decreased during migration. Once the cells arrive in regions of higher cell substrates, they may resume proliferation and halt their migration. Since not all cells within a tumor may develop a migratory phenotype, two subsets of viable cells are created when this situation occurs, viz., one stationary and one motile. Here, to model the effect of chemotaxis on a particular cell species, the velocity is modified as:

$$\mathbf{u}_S = -k(\phi_j)\left(\nabla p - \frac{\tilde{\gamma}}{\varepsilon}\mu\nabla\phi_\Gamma\right) + \chi\mathscr{C}(\phi_i, n)\nabla_n, \tag{48}$$

$$\mathscr{C}(\phi_i, n) = \phi_i(1 - n), \tag{49}$$

where χ is the overall strength of the taxis, and $\mathscr{C}(\phi_i, n)$ is a function that adjusts this strength based on the presence of viable original or mutated cells and the cell substrate level n. To adjust the mitosis rate, a function is used to replace the previously defined rate:

$$\lambda_i^{m*}(\phi_i) = \lambda_i^m(1 - \mathscr{C}(\phi_i, n)), \; i = \mathrm{V} \text{ or } \mathrm{M}. \tag{50}$$

This equation indicates that when the chemotaxis rate $\mathscr{C}(\phi_i, n)$ is high for a particular cell species i, then the proliferation rate $\lambda_i^{m*}(\phi_i)$ for this species is low, and vice-versa.

2.8 Mutation of species

The choice of the mutation event ($\mathbf{x}^*$, $\mathbf{t}^*$) has a random component (generated at a frequency 1/8 day^{-1}) at locations where the viable species density $\phi_V > 0.5$ and $n < 0.6$. The spatial dependency ensures that mutations are more likely to occur where cells are viable and in regions of low cell substrates, i.e., perinecrotic regions. A successful mutation covers a spherical space of radius r^*, lasting for a time δt^*. The mutation transfer function is chosen to be

$$\mathscr{M}^{V\to M}(\mathbf{x}, t, \phi_i) = g(\mathbf{x}, \mathbf{x}^*)a(t, t^*)\phi_V(\mathbf{x}, t), \tag{51}$$

where g is a Gaussian distribution function spatially located at $\mathbf{x}^*$, and a is a time activation function starting at time t^* and lasting δt^*. Precisely,

$$g(\mathbf{x}, \mathbf{x}^*) = C_{mut}\exp - \frac{\|\mathbf{x} - \mathbf{x}^*\|^2}{(r^*)^2}, \tag{52}$$

$$a(t,t^*)=\frac{4b}{(1-b)}, b=\frac{t-t^*}{(\delta t)^*} \quad (53)$$

where $C_{mut} > 0$ is a rate constant. The frequency of mutation events is set artificially high in order to observe their effects over a shorter period of simulated time; also, in the model a mutation event may not persist if the species is unable to survive.

The effects of the mutations on the phenotype are coupled nonlinearly to the tumor scale through the cellular pressure and cell substrate gradients in the microenvironment, and their effect on cell proliferation and apoptosis (Wise et al., 2008).

3 Angiogenesis

We model the physiology and evolution of tumor neovasculature in 3D using an angiogenesis model that is independent of the underlying computational grid (lattice-free). This random walk model has its origins in earlier work by Anderson and Chaplain (1998); McDougall et al. (2002) and is a refinement of previous work (Plank and Sleeman, 2003, 2004). The model was shown to create dendritic structures consistent with experimentally observed tumor capillaries (Less et al., 1991; Skinner, 1990). We couple this algorithm with the diffuse interface tumor model of Section 2, thus fully extending to 3D the work by Zheng et al. (2005).

The angiogenesis model generates a vascular network based on tumor angiogenic regulators (Takano et al., 1996), e.g., vascular endothelial growth factor (VEGF), represented by a single continuum variable that reflects the excess of pro-angiogenic regulators compared to inhibitory factors. Peri-necrotic (hypoxic) tumor cells are assumed to be a source of these regulators, stimulating the endothelial cells to proliferate and to form vessels towards the location of the tumor (Jain, 2003). In the model, the angiogenic effects of host tissue cells close to the tumor are not represented but could easily be incorporated. The migration of endothelial cells is described by chemotaxis and haptotaxis. For simplicity, we model only the leading endothelial cells, while the trailing cells follow passively with proliferation occurring at the cells close behind the tip cell.

The tumor-induced vasculature does not initially deliver cell substrates, as the vessels need to form loops (anastomose) first. Leading endothelial cells have a fixed probability of branching at each time step, and vessels may connect if a leading endothelial cell crosses the trailing path of another vessel. Only looped (anastomosed) vessels can provide a source of cell substrates in the tissue (Augustin, 2001), and they may further undergo spontaneous shutdown and regression during the growth of the tumor as the proliferation of the cancer cells in their vicinity increases the tissue solid pressure (Holash et al., 1999).

3.1 Angiogenic regulators

The concentration of angiogenic regulators, denoted by c, is governed by the diffusion-reaction equation,

$$0=D_c\nabla^2 c-\beta_d c+S_c\phi_h(c_{sat}-c) \quad (54)$$

where D_c is the diffusivity, β_d is the natural decay rate, S_c is the transfer rate of the supply from the hypoxic cells, and c_{sat} denotes the saturation level. The volume fraction of hypoxic

cells ϕ_h is defined as the volume fraction of viable cells where the cell substrate is lower than a specific threshold, which is here set to be the same as the necrotic threshold.

3.2 Angiogenesis initialization

The new capillaries form randomly at sprouts near the tumor boundary following the concentration of angiogenic regulators. The scheme first identifies all the sites where the (normalized) viable cell density is less than 0.2 and angiogenic regulator concentration is greater than 0.1, which guarantees that the sites are outside the tumor and very close to the tumor/host boundary. Then these sites are weighted by the regulator concentration and one site is randomly selected from the list. The site with the higher regulator concentration is thus selected as the vessel sprout site. The frequency of site generation was set to 5 per unit time step (day), which was calibrated to yield a reasonable number of vessels over the time course of the simulations presented herein.

3.3 Biased circular random walk

Vessels are generated based on Plank and Sleeman's biased circular random walk model (Plank and Sleeman, 2003, 2004). The trajectories of the tip endothelial cells move in a random walk on the unit circle. For two-dimensional space, the tip location (x,y) can be characterized by its speed s_{tip} and direction angle θ,

$$\frac{dx}{dt}=s_{tip}\cos\theta,\ \frac{dy}{dt}=s_{tip}\sin\theta \tag{55}$$

At each time step k the tip has a probability of turning clockwise or counter-clockwise by a small finite angle δ, or to continue in the same direction. This probability is generated through the normalized transition rate τ (θ),

$$\tau(\theta,t)=\frac{1}{\sigma^2}\exp\left(2\int\frac{\mu}{\sigma^2}d\theta\right) \tag{56}$$

where μ and σ^2 are the expectation (mean) value and the variance of the turning rate, respectively, which can be adjusted according to the statistical analysis of the capillary network. Both are functions of orientation θ and time

$$\sigma=\sigma(\theta,t)\ ,\ \mu=\mu(\theta,t). \tag{57}$$

Chemotaxis and haptotaxis can be modeled as two taxis species by taking the mean turning rate μ, such that the tips tend to reorient themselves so that they are moving up the local gradient of the species. The mean of the turning rate can be written as

$$\mu=\sum_i - d_i\sin(\theta-\theta_i^*) \tag{58}$$

where θ_i^* is the preferred orientation along the gradient of each taxis species i, and d_i is its corresponding turning coefficient which indicates the cell's ability to reorient itself due to taxis, and is therefore proportional to the magnitude of the gradient. In our study, the preferred orientations θ_{chemo}^* and θ_{hapto}^* for the chemotaxis and haptotaxis species are the positive directions of ∇c and ∇f, respectively. Therefore,

$$\mu = -d_{chemo}\sin(\theta - \theta^*_{chemo}) - d_{hapto}\sin(\theta - \theta^*_{hapto}). \quad (59)$$

In our simulations, for simplicity we fix σ to be a constant (see Table 3).

The magnitude s_{tip} of the tip cell velocity can also be set proportional to the chemotaxis and haptotaxis gradients,

$$s_{tip} = C_{chemo}\|\nabla c\| + C_{hapto}\|\nabla f\|, \quad (60)$$

where C_{chemo} and C_{hapto} are the weighting factors of the chemotaxis and haptotaxis effects, respectively. We choose a value of s_{tip} such that the complex interaction of the vasculature and the tumor can be developed in a shorter amount of simulated time. Here, for simplicity we set s_{tip} to be constant at 0.5 day^{-1}.

The model is easily extended to 3D by adding a second angle, ϕ, as the polar angle and using θ to represent the azimuthal angle. The tip location (x, y, z) is then tracked by the following equations of motion:

$$\frac{dx}{dt} = s_{tip}\cos\theta\cos\phi,\ \frac{dy}{dt} = s_{tip}\cos\theta\sin\phi,\ \frac{dz}{dt} = s_{tip}\sin\theta, \quad (61)$$

where the transition rate of ϕ can be defined independently, similar to Eq. (56).

At each time step, the local gradients of the taxis species are measured near the tip endothelial cells. For each angle (θ and ϕ), the transition rate is calculated with respect to the gradients, based on which it is determined if the cell stays at the current angle or turns clockwise or counterclockwise. Once two angles are determined, the new location of the cell is updated.

3.4 Branches, anastomoses, and vessel shutdown

A capillary has a fixed probability of branching at each time step. When branching occurs, the leading endothelial cell splits into two leading cells with the new cells reorienting by a fixed angle of 30 degrees. The two cells then continue to migrate and proliferate into new vessels. If the leading cell of one vessel crosses the trail of another vessel from a different sprout site, then anastomosis may occur (self-intersections are not allowed). This process forms a closed loop and the corresponding vessel segments between the two sprouts can now be a source of cell substrates to the surrounding tumor tissue. See Fig. 3.

The model does not include blood flow rates in the vasculature or the associated morphological changes in the vascular network, such as branching induced by shear stress. Thus, the direction of the flow is not taken into account. Rather, the model considers oxygen/nutrient extravasation after vessels anastomose, as we focus on the effect of local heterogeneity of these substances on the tumor species. Simplified models of the blood fluid dynamics in capillary networks have been developed (e.g, Pries et al. (1998); McDougall et al. (2002); Stephanou et al. (2005, 2006); McDougall et al. (2006); Bartha and Rieger (2006); Lee et al. (2006); Wu et al. (2007); Zhao et al. (2007); Sun and Munn (2008); Pries and Secomb (2008); Welter et al. (2008); Owen et al. (2009); Macklin et al. (2009)). Here, we do not describe this level of detail, which will be considered in future work.

Since the magnitude of the vessel tip cell velocity and the probability of branching at each time step are fixed, the length of each vessel segment is approximately constant.

When the solid pressure p due to tumor cell proliferation exceeds the threshold p_{crush} at a certain tumor location, then the nearby local vessels are shut down by removing them from the vasculature network (Fig. 3). Any vessel loops associated with the removed segments that are now open will discontinue supply of cell substrates. These segments can resume delivery if they become connected to new loops formed through later angiogenesis.

3.5 Effective vascular density

To determine the cell substrate supply rate constant in Eq.(45), the density of the effective vasculature (substrate-transferring) at any computational grid is determined by integration of the contribution from all the vessel segments that are supplying cell substrates. This is modeled by

$$\phi_{ves}(\mathbf{x}) = C_{ves} \sum \frac{1}{2} \left(1 - \tanh \frac{|\mathbf{x} - \mathbf{x}_c| - r_{ves}}{\epsilon_{ves}} \right) \tag{62}$$

where the vessel segment is defined by two consecutive nodes on each oxygen/nutrient-transferring vessel branch, $\mathbf{x}_c$ is the projection of $\mathbf{x}$ on the alignment of each segment axis formed by two ends of that segment, r_{ves} is the radius of the vessel, and ϵ_{ves} controls the thickness of the transition of the hyperbolic function. Projections outside the segment axis are excluded from the integration. C_{ves} is the conversion constant.

4 Hybrid continuum-discrete modeling of tumor invasion

4.1 Continuum and discrete mapping

So far we have defined viable tumor cell species that exhibit certain phenotypic characteristics as a group, including the ability to migrate under conditions unfavorable for cell homeostasis. Yet individual tumor cells may mobilize to enhance their chance of survival. Discrete cells may migrate from tumor hypoxic regions due to the downregulation of cell-cell and cell-matrix adhesiveness, representing an epithelial-to-mesenchymal transition from collective to individual motion. These discrete cells interact with each other and the environment; they may accumulate near nutrient-rich areas and then proliferate to form distant tumor lesions. Also, there could be small volume fractions of specific cell species (e.g. stem cells) that may be better described as discrete in the presence of continuum cell species.

These phenomena can be modeled using a hybrid continuum-discrete approach (Lowengrub et al. (2010)). In order to do this, the model of Section 2 is enhanced to implement a one-to-one continuum and discrete description mapping for the cell mass (or volume), so that the mass conservation is guaranteed when cells are converted to the continuum field, and vice-versa. The location is selected randomly to favor regions where viable tumor cell species are hypoxic (i.e., originating from the volume fraction ϕ_h in Eq. (54)). This is consistent with experimental observations of the effects of hypoxia (Friedl et al., 1995; Hegerfeldt et al., 2002; Kaneko et al., 2002; Friedl and Wolf, 2003). Discrete cells may also be introduced if the corresponding continuum volume fraction drops below a critical threshold within the tumor domain (this case will be considered in future work). Here, we employ a model that incorporates chemotaxis, haptotaxis, and volume exclusion such that two cells cannot occupy the same position in space. The cells may also respond to the velocity induced by the continuum volume fractions and compete with the continuum description for cell substrates.

4.1.1 Discrete cell conversion—Single cells are modeled as dots occupying discrete coordinates in space (i.e., changes in cell size and shape are not modeled). The conversion from discrete to continuous space is performed through a shape function. For any discrete cell at location $\mathbf{X}_i$, the shape function at the continuum level is:

$$G^o(\mathbf{x}, \mathbf{X}_i) = \frac{1}{2}\left(1 - \tanh\frac{|\mathbf{x} - \mathbf{X}_i| - r_c}{\epsilon_{disc}}\right) \tag{63}$$

where $\mathbf{x}$ is the location of the continuum field, and r_c is the radius of the sphere representation in the continuum field of a discrete cell. This shape function returns 1 inside the sphere and 0 outside of the sphere, with a transition from 0 to 1 at the interface, and ϵ_{disc} controls the width of the transition region.

Integrating $G^o(\mathbf{x}, \mathbf{X_i})$ over the whole domain $\mathbf{x}$ for any single cell gives the volume of the shape, converging to the volume of a sphere when ϵ_{disc} tends to zero,

$$V_c = \int G^o(\mathbf{x}, \mathbf{X}_i) d\mathbf{x} \approx \tfrac{4}{3}\pi r_c^3. \tag{64}$$

Due to numerical limitations, the volume of each computational grid is normally larger than a single tumor cell in biological reality. The conservation of volume at the continuum and discrete levels can be enforced by a scaling factor A_c:

$$A_c = V_d / V_c = (r_d / r_c)^3 \tag{65}$$

where V_d is the non-dimensionalized volume of a single real cell with a radius of r_d.

For example, if a cell has a radius $l \approx 5\mu m$ and the model computational length scale $L \approx 100\mu m$, then the non-dimensional radius $r_d = 0.05$. If we take r_c as 0.1, then $A_c = 1/8$, meaning that one discrete cell in the simulation corresponds to 8 cells at the biological scale. Once this one-to-one mapping between the continuum and discrete levels is developed, not only is the mass conserved during conversions, but also the rates and physical constants at both levels can be related.

The contribution of all discrete cells to any field location (effective cell volume fraction) can be summed up as

$$G(\mathbf{x}) = \sum_{i=1}^{N} A_c G^o(\mathbf{x}, \mathbf{X}_i), \tag{66}$$

where N is the total number of active discrete cells. This function can be used to model the effect of the discrete cells in the continuum description. For example, the cell substrate uptake by the cells can be modeled as:

$$U(\mathbf{x}) = U_c G(\mathbf{x}), \tag{67}$$

where U_c is the uptake rate constant which can be taken to be the same as the uptake rate constant for the viable species at the continuum level. The uptake term is then included in

the cell substrate transport equation (42). This applies to other quantities as well, e.g., fibronectin production.

4.1.2 Population of cells—When the local population of discrete cells becomes too large, mass is transferred to the continuum description and discrete cells are removed from this region. To determine the number of cells per unit volume, Eq. (63) is used with an appropriate radius r_{pop} to replace r_c. This gives the number of cells (local population) G_{pop} within the radius r_{pop},

$$G_{pop}(\mathbf{x}) = \sum_{i=1}^{N} G^o(\mathbf{x}, \mathbf{X}_i). \tag{68}$$

When the local population G_{pop} is large enough, any region with $G_{pop} > G^*$ (here, $G^* = 40$) is allowed to transform to the continuum form.

4.2 Dynamic conversion

To model conversions from continuum to discrete descriptions, we use a dynamic approach. An extra term $S(\mathbf{x})$ is added to the source term of the mass conservation equation (17) for the viable cell density ϕ_V. For each detected location $\mathbf{X}_i$ where discrete cells should be created, the volume fraction (or mass) is extracted at the rate,

$$S_i^{c\to d}(\mathbf{x}, \mathbf{X}_i) = C_e G^o(\mathbf{x}, \mathbf{X}_i), \tag{69}$$

where C_e is the rate of extraction. In general, C_e can be modeled as a non-uniform function, e.g., as a function of the viable cell density ϕ_V. Here, we take the formula $C_e = -C_{extract}\phi_V < 0$, where $C_{extract}$ is the extraction rate constant that prevents the continuum cell volume fraction from depleting below zero. The total volume transfer rate associated to a particular location $\mathbf{x}$ is then given by

$$S(\mathbf{x}) = \sum_{i=1}^{N} S_i^{c\to d}(\mathbf{x}, \mathbf{X}_i) \tag{70}$$

where N is the total number of extraction sites (i.e., producing N discrete cells).

Throughout the conversion, the total mass extracted from the continuum field for each extraction site $\mathbf{X}_i$ is also tracked:

$$V_i^{c\to d} = \int_{\Omega} S_i^{c\to d}(\mathbf{x}, \mathbf{X}_i) dt d\mathbf{x}, \tag{71}$$

where $\int_\Omega d\mathbf{x}$ stands for the integration over the whole continuum domain. Once the total mass exceeds the discrete cell mass volume V_c, the discrete cell is formed and released as active.

If the discrete cell population exceeds a certain level (detected as described above), then mass can be converted to the continuum description. This occurs at nutrient-rich locations, where single cells may aggregate and proliferate. The conversion can be modeled in the

same way as the formation of individual cells, except that the rate constant becomes the deposit rate constant:

$$S_i^{d\to c}(\mathbf{x},\mathbf{X}_i)=C_d G^o(\mathbf{x},\mathbf{X}_i), \tag{72}$$

where $C_d = C_{deposit}(1-\phi_V) > 0$ is the deposit rate, with $C_{deposit}$ as a constant. Note that this conversion can only occur if there is space at the continuum level, i.e., $\phi_V < 1$, to introduce the converted mass. As in the extraction process, once the total volume deposited for a particular deposition site exceeds the discrete cell volume V_d, the cell is destroyed and the process is completed for this cell. For simplicity during the conversion process, cells are tagged as inactive and excluded from interaction with other cells and the environment.

4.3 Discrete cell modeling

While discrete cells are active, they can move and interact with each other and the microenvironment. The discrete cells do not impart a force on the continuum tumor fields, but respond to the velocity induced by cell proliferation and adhesion at the continuum level. See Lowengrub et al. (2010) for a more general approach, in which force interactions between continuum and discrete fields are described.

The velocity of each cell is determined as follows:

$$\mathbf{v}=D_v\mathbf{u}_s+\mathscr{F}(f)\,(D_{chemo}\nabla n+D_{hapto}\nabla f)\,(1-n)+\mathbf{u}_{repulsive} \tag{73}$$

where D_v, D_{chemo} and D_{hapto} are rate constants that can be used to adjust several effects. $\mathbf{u}_s$ is the cell velocity, and the second and third terms describe chemotaxis and haptotaxis, respectively, where n and f are the corresponding cell substrate and fibronectin concentrations. Cell movement occurs under conditions of low cell substrates. $\mathscr{F}(f)$ modulates this movement so that it occurs when the fibronectin concentration is neither too low nor too high, e.g., it can be defined as a simple parabolic function.

Since no two cells occupy the same space, volume exclusion is modeled using a cell exclusion velocity $\mathbf{u}_{repulsive}$ based on the repulsive force. Since this force is activated when the cells are within an interaction radius Δr, we define

$$\mathbf{u}_{repulsive}=C_{disc}\left(\frac{1}{\left(\frac{|\Delta\mathbf{x}|}{\Delta r}\right)^2}-1\right)\frac{\Delta\mathbf{x}}{|\Delta\mathbf{x}|}\Delta r \tag{74}$$

where $\Delta\mathbf{x}$ is the vector pointing from one cell to another. This force is normalized with respect to the interaction radius Δr and its magnitude can be adjusted through a constant C_{disc}.

To smooth out the cell velocity and prevent abnormally large velocities, the final velocity is limited by a maximum travel distance per step time, set as 0.5 in order to be consistent with the underlying continuum field grid spacing.

5 Results

5.1 Avascular Tumor Invasion

We consider the growth of a tumor comprised of one viable species. Using the continuum model only, the growth of an initially perturbed spherical tumor in 3-D with low cell adhesion ($\gamma = 0$, Part I) is shown in Fig. 4. Note that there is an effect of cell adhesion through the Laplacian term in μ in Eq. (33). The isosurface $\phi_T = 0.5$ is plotted. The parameters are given in Table 1 (as defined in Part I (Wise et al., 2008)). The regular Heaviside function H is used for these simulations (instead of $\mathcal{H}$ as defined in Sec. 2.5.1, see below).

In this simulation, the substrate gradients contribute to variable tumor cell proliferation and necrosis but do not induce migration (e.g. chemotaxis of tumor cells). Consistent with linear analyses (Cristini et al., 2003; Li et al., 2007), the tumor is morphologically unstable due to the limited supply of cell substrates and the corresponding tumor mass loss due to necrosis in its interior. The simulation shows that in the nonlinear regime, a morphologically complex tumor emerges with repeated subspheroid growth. By acquiring this complex morphology, the tumor has effectively increased its surface area to volume ratio in order to gain access to more cell substrates from the surrounding host environment, thus overcoming diffusional limitations to growth. This effect has been observed *in vitro* (Fig. 2) (Frieboes et al., 2006)).

5.2 Vascularized Tumor Invasion

We now consider the growth of a tumor in a vascularized environment. The parameters are given in Tables 3 and 2. Note that the difference in magnitude in the necrosis rates between Table 2 and 1 is because in Eq. (36), $\mathcal{H}$ is used (instead of H as in Sec. 5.1 and Part I) to account for the continuous conversion of tumor mass into dead cells implemented for the simulations herein.

5.2.1 Base Case Without Vessel Shutdown—We first simulate the growth of a tumor with one viable species, assuming that the solid (internal tumor) pressure does not shut down any of the vessels, in order to contrast the outcome when shutdown is introduced in the subsequent simulations.

The tumor begins as a small, round avascular nodule (Fig. 5, $t = 3$). As necrosis forms in the core (darker color), angiogenic regulators diffuse from the interior to the outside, stimulating the formation of new capillaries in the vicinity of the tumor (small lines) from a pre-existing vasculature (virtually represented). Endothelial cells in these vessels proliferate up a gradient of angiogenic regulators, first forming branches and then looping to conduct blood (darker lines). As the nodule becomes surrounded by conducting vessels ($t = 8$), it is able to grow larger. The tumor shape assumes a slightly more asymmetric form ($t = 15$), determined by the heterogeneity in cell proliferation and death, which is in turn based on the availability of cell substrates in the microenvironment as a function of the vasculature (Eqs. 17). The amount of necrosis is stable as hypoxic cells gain access to substrates. Figure 6 shows that viable tumor tissue cuffs around the locations of vessels, as observed experimentally (Kunkel et al., 2001) as well as clinically (Frieboes et al., 2007;Bearer et al., 2009), with areas distal from the conducting vessels being necrotic.

The tumor is seen in later stages ($t = 54$) to continue growing uniformly and fairly compactly in time, consistent with the prediction of Cristini et al. (2003), in which non-uniformity in the environment is required for asymmetric growth of vascularized tumors. Vessels are uniformly distributed around and inside the lesion. Unlike the avascular case in

Fig. 4, the tumor morphological instability is significantly lessened. Figure 7 shows the proportion of total, viable, and dead tumor cells, Figure 8 shows the number of vessels as a function of time, and Figure 9 indicates the growth of the vascular network measured by total vessel length. The correspondence between the number of vessels and the total vessel length implies that the vessels seem to form loops before they become tortuous, reflecting the choice of parameters (Sections 3.3 and 3.4).

Given the vessel radius and length, the ratio of vessel volume to viable tumor volume can be calculated. The vessel volume is obtained by using the total length of conducting (i.e., looped) segments L_{ves} (defined as in Fig. 3):

$$V_{ves}=\pi r_{seg}^2 L_{ves} \tag{75}$$

where r_{seg} is the radius of a vessel segment represented as a cylinder. The radius of tumor tissue supported by the vasculature can then be estimated as

$$r_{sup}=\sqrt{V_V/\pi L_{ves}}=r_{seg}(V_{ves}/V_{eff})^{-1/2} \tag{76}$$

where V_{eff} is the total effective tumor species density; e.g. for the viable species,

$V_{eff}=\int_\Omega \frac{\phi_V}{\phi_S} d\mathbf{x}$.

Assuming the diameter of a biological cell to be $\approx 10\mu m$ (also taken as the diameter measure for a capillary), the ratio of vessel volume to viable tumor volume in this simulation approximates 4.5×10^{-3} over time, as shown in Fig. 10. The attainment of an almost constant ratio at later times provides a quantitative measure of the stabilizing effect of the vascularization on the morphology of the growing tumor.

5.2.2 Base Case With Vessel Shutdown—Next we simulate the growth of a tumor with one single viable species as in Section 5.2.1, but include the effects of vessel shutdown due to the solid (internal tumor) pressure. As in the previous case, the tumor begins as a small, round avascular tumor nodule (Fig. 11, $t = 1$), and becomes surrounded by new capillaries through the process of angiogenesis (e.g., $t = 8$ and $t = 20$). At some point the cell proliferation exerts enough pressure that the blood flow in some of the capillaries becomes impeded, shuts down ($t \approx 23$), and the vascular network regresses. Hypoxia is then locally increased, triggering a higher release of angiogenic regulators. The viable cells downgrade their proliferation as stipulated in Eq. (17). Eventually cell homeostasis is disrupted to such an extent that several regions of the tumor undergo necrosis, causing the tumor to regress, thus exacerbating the morphological instability through uneven shrinking of the tumor mass ($t = 25$). A similar effect has been observed through the model when simulating anti-angiogenic therapy (Cristini et al., 2005), which may shut down the tumor vasculature in an uneven manner and exacerbate tumor break-up and invasion (Rubenstein et al., 2000;Kunkel et al., 2001;Lamszus et al., 2003;Bello et al., 2004).

A new round of vessel generation is triggered at $t = 25$ induced by the production of angiogenic regulators as a result of increased hypoxia in response to continued cell proliferation and tumor necrosis. This second wave of angiogenesis leads to a larger tumor with a more complex morphology (Fig. 12, $t = 48$) than at earlier times, until the pressure from cell proliferation disrupts the blood flow ($t = 49$) once again. By this time, however, the tumor has gained enough mass so that the disruption predominantly affects the right hemisphere, which leads to tissue breakup in this region. The consequent hypoxia

upregulates angiogenesis towards the right side of the tumor, as seen at $t = 54$. Observe that the new vascular network is concentrated more to-wards the center of the tumor and not at the leading clusters, since these have better access to the surrounding (existing) host vasculature (not shown). By $t = 63$ vessels become disrupted on the left lobe, which initially shrinks and furthers the splitting of the tumor into two pieces. As cell proliferation once again increases due to enhanced vascularization, the two parts grow larger and begin to reconnect ($t = 79$). The stability of the tumor morphology and its invasiveness are directly linked to the availability of cell substrates regulated by the evolving vasculature in response to cell proliferation and death.

Fig. 13 shows the proportion of total, viable, and dead tumor volume in time. The periods of vessel shutdown and consequent tumor mass regression become apparent at regular intervals (e.g. the events at $t = 23$ and $t = 49$), in contrast to the smoother growth of the case without shutdown (Fig. 7). In spite of this effect, the overall trend indicates vigorous mass growth at a roughly super-linear rate. Fig. 14 shows that after growing steadily over a period of about 20 days, the number of new vessel sprouts drops and then increases over the next 30 days to oscillate within a small range, while the total number of looped vessels oscillates dramatically due to both branching/anastomosis and vessel shutdown. Fig. 15 indicates that the growth of the looped (conducting) network measured by total vessel length is also very rapid initially, and then seems to oscillate (within a range). As before, the correspondence between vessel number (Fig. 14) and vessel length (Fig. 15) suggests that vessel tortuosity is minimized in this simulation.

The ratio of vessel volume to viable tumor volume can be calculated as in the case with no vessel shutdown, and is shown in Fig. 16. Unlike the case in Fig. 10, the figure shows that the evolution is non-monotone. The ratio increases to a maximum value at time ≈ 30, but then decreases as the tumor and its fragments continue to grow, implying evolution to smaller fractions. The initial overshoot indicates the vascular response to the build-up of hypoxia in the initial stage of growth. Effectively, the fragmentation of the tumor mass at later times enhances the exposure of clusters and fingers of cells to the surrounding vascularized host tissue, thus decreasing the amount of hypoxic tissue in need of neovascularization.

We can also estimate the radial distance r_{sup} of viable tumor cells supported by each endothelial cell (Eq. 76). From Fig. 16, $V_{ves}/(\int_\Omega \phi_V / \tilde{\phi}_S d\mathbf{x}) \approx 3.5 \times 10^{-3}$. Assuming $\tilde{\phi}_S = 0.8$ and $r_{seg} = 5\mu m$, then $r_{sup} = r_{seg}\left(\tilde{\phi}_S \frac{V_{ves}}{\int_\Omega \phi_V \, d\mathbf{x}}\right)^{-1/2} \approx 95\mu m$, which is congruent with biological phenomena (Bussolino et al., 2003) as well as the Krogh blood perfusion model (Krogh, 1919) and the modeling of tumor cords (Bertuzzi et al., 2005;Astanin and Tosin, 2007).

5.2.3 Activation of chemotaxis, and upregulation of cell substrate uptake and proliferation—In order to study in more detail the phenomenon of tumor invasion under vascularized conditions, we begin again with a small, round tumor nodule with one viable species, whose central necrosis triggers angiogenesis (Fig. 17, $t = 3$). This case investigates the tumor-level invasive effect of chemotaxis for cells undergoing hypoxia and cell substrate starvation. When tumor cells sense an unfavorable environment, they may change their phenotype by down-grading proliferation and upgrading migration (e.g., expression of the MET proto-oncogene that encodes a tyrosine kinase that acts as the receptor for Hepatocyte Growth Factor (HGF) (Giordano et al., 1993), which has been found to be involved in cell migration), moving to regions that are more favorable for cell homeostasis (Hughes and Mcculloch, 1991;Palka et al., 1996). Once the environment becomes more propitious, proliferation may then be upgraded and migration downgraded (Pettet et al., 2001).

In this simulation, a more aggressive cell species is randomly activated in time from the original viable tumor species. Aggressiveness is characterized by two changes in phenotype (possibly triggered by genetic mutations). One change upregulates cell substrate uptake ν_M^μ and proliferation λ_M^m when microenvironmental conditions are favorable, both higher by an amount 1.5× than for the original viable tumor cells (Table 2); the tumor parameters $n_M^*, \lambda_M^n,$ and λ_M^a are the same as for the viable species. When the environmental conditions turn unfavorable, e.g., when nutrient and oxygen concentration become poor due to low or inefficient vascularization, the other phenotypic change is expressed. This change enables the tumor species to become motile and migrate away from unfavorable regions into areas that offer better conditions for cell survival, e.g., having higher concentrations of nutrient, oxygen, and growth factors, as well as lower concentrations of metabolites. The more aggressive species thus enhances its survival by upregulating migration and downregulating proliferation when necessary, to avoid becoming quiescent and being advected away from vessels as tumor tissue closer to these vessels continue proliferation. Once the aggressive species reaches a region with higher cell substrates, the species stops migration and resumes its (higher) proliferation.

The effects of the appearance and behavior of the aggressive species on the overall tumor morphology are revealing. The first appearance (darker color) occurs at $t \approx 8$, the second at $t \approx 15$. The faster proliferation of this species increases its respective mass to the point that the whole tumor becomes surrounded by it by $t = 29$. Note that some vessel shutdown is observed, e.g., at $t = 36$ (top right area of tumor). The overall mass tends to increase more uniformly than the base case with vessel shutdown. This is likely due to the enhancement of necrosis of the original viable species (which relieves the solid pressure) caused by the larger cell substrate uptake of the aggressive species. Yet the morphology is not as compact as when the vasculature was stable (without shutdown, Fig.5).

In Figure 18, 2-D slices along the tumor center ($x = 10$) are shown at $t = 36$ for the total tumor mass, original and aggressive tumor species, dead tumor mass, and pressure and nutrient. The aggressive species, which has situated itself via chemotaxis on the periphery of the tumor, has optimal access to nutrients and oxygen. Since this species is the determinant of the overall morphology due to its higher proliferation, its more stable microenvironment helps to decrease the morphological instability caused by diffusion gradients of oxygen and nutrient.

This situation is reflected in Figure 19. The proportion of aggressive species increases over time, while the original viable species volume remains stable. The periods of vessel shutdown and consequent tumor mass regression have decreased, and the total volume is smaller than in the base case after the same period of time (30 days). The number of vessel sprouts is only slightly larger (Figure 20), and indicates a roughly linear increase corresponding to the more stable tumor growth. The total length of conducting vasculature reflects this trend (Figure 21). Furthermore, the ratio of vessel volume to viable tumor volume (Fig. 22) does not decrease over time as dramatically as in the previous case, since there is less tumor mass fragmentation.

Thus, unlike the base case with vessel shutdown, the tumor morphology is more stable and invasion is significantly curtailed. The effect of the migratory, more aggressive species is essentially to “encapsulate” the tumor. Mature tumors have (e.g., prostate, breast) shown evidence of multiple clones in their population. The model suggests that in these situations, the multiple clonality of the cell population is a critical component of the overall tumor morphological stability. Here, stability may also be a result of reduced mobility of the tumor cells at the margin since migration is downregulated there due to availability of oxygen and

nutrient. Treatments that (inadvertently) target only a subset species may disrupt this stability and lead to heightened tumor invasion. Maintaining a stable vessel volume to viable tumor volume (Fig. 22) would be a quantitative measure of this.

5.2.4 Upregulation of chemotaxis only—In order to isolate the effects of cell motility on the overall tumor morphology, we study a third case. As before, the tumor starts as a small, round avascular tumor nodule with one viable species. The more aggressive species appears randomly, but this time only expresses the migratory phenotype. The tumor parameters are the same as for the viable species in Table 2. The uptake of nutrient and oxygen remains the same as in the original species. The second species upregulates cell migration when the environmental conditions become unfavorable for cell proliferation, which, as in the previous case, usually occurs in the inner areas of the tumor distal from conducting blood vessels. Also, as before, the migrating cells downregulate their proliferation until they reach regions that have higher concentrations of cell substrates, such as at the tumor/host interface.

The first appearance of the second species is at $t \approx 3$, seen at the periphery of the tumor nodule (Fig. 23, darker color). The tumor expands with increased angiogenesis, and new appearances become clearly visible by $t = 29$. The aggressive cells migrate to the surface of the tumor, where access to nutrients and oxygen are optimal. The species may combine with each other. In some cases, the species does not persist because the cells die from insufficient cell substrates before they could migrate to a more favorable location. At $t = 54$ the pressure from cell proliferation shuts down a group of vessels (center of tumor), leading to mass regression and a slightly more complex morphology ($t = 63$).

Figure 24 shows that unlike the previous case, the volume of the aggressive species remains small as a percentage of the total tumor volume, and smaller than the original viable specis, since its net proliferation is lower due to its migratory phenotype. Both the number of vessel sprouts (Figure 25) and the overall size of the conducting vasculature (Figure 26) increase smoothly over an initial period, and reflect the dramatic vessel shutdown episode around day 51. The ratio of vessel volume to viable tumor volume (Fig. 27) is now more monotonic than when the aggressive species had encapsulated the whole tumor (previous case), stabilizing at a range above 3×10^{-3} during the time of the simulation.

What we find here is that the morphology is substantially more complex than in the case when the aggressive species also increased cell substrate uptake. Essentially, the aggressive and the original species uptake the available cell substrates on equal terms. The ability to migrate by itself does not seem to confer an overriding advantage to the second species, since migration ceases once the species obtains adequate nutrient and oxygen (e.g., on the periphery of the tumor). Thus, although migration may enhance the survival of individual cells, it lowers the net proliferation of the whole species.

We also study the case where all tumor viable cells are allowed to migrate if microenvironmental conditions turn unfavorable for proliferation (Fig. 28). In a simulation of this more aggressive phenotype, with the same initial conditions as in the base case, by $t = 8$ the tumor has assumed a slightly complex shape. When the pressure from cell proliferation shuts down vessels around the same time as in the vascularized base case ($t = 25$), the tumor mass shrinks dramatically and angiogenesis is upregulated ($t = 29$). The tumor regrows with a more complex morphology, and splits into two distinct parts by $t = 54$, which then grow separately, unlike the base case with vessel shutdown in which the second wave of angiogenesis had led to a more compact mass around this time of the tumor progression.

This simulation suggests that the reason for the more complex morphology is the instability introduced by the chemotaxis of the hypoxic cells, moving from the interior of the tumor mass to the periphery where cell substrate concentration is higher. This is consistent with linear stability theory (Cristini et al., 2009), as well as clinical observation (Bearer et al., 2009).

Further, the proliferation is slower because of the chemotaxis effect, as migrating cells downregulate their proliferation. Figure 29 shows that while the overall tumor volume growth is slower than in the previous case, the proportion of viable cells is the highest of all the cases analyzed, i.e., the death of cells is minimized by their ability to migrate. The number of new vessel sprouts (Figure 30) and overall length of conducting vessels (Figure 31) do not seem to stabilize over the time period simulated while reflecting the dramatic shrinking of the tumor mass during episodes of vessel shutdown. Finally, the ratio of vessel volume to viable tumor volume (Fig. 32) is non-monotone, approximating over time the smallest value of all the cases studied (2×10^{-3}). This indicates that the tumor relies more on the established (host) vasculature by employing the ability to actively invade cluster-like into the surrounding tissue in order to maximize cell homeostasis.

5.2.5 Invasion of discrete cells—We further study the effect of individual cell chemotaxis and haptotaxis on the tumor morphology and invasiveness as a result of hypoxia-induced transitions to individual cell motion. The parameters are given in Table 4. Fig. 33 shows the evolution of a vascularized tumor using the hybrid tumor model described in Section 4. Discrete cells (small dots) are released from hypoxic (perinecrotic) regions of the continuum tumor description (solid surfaces) ($t \approx 2.00$). This mimics a hypoxia-induced epithelial-mesenchymal transition from collective to individual cell behavior. Single cells move away from the tumor bulk and up gradients of oxygen, which is supplied at the far-field boundary (host tissue) and from the newly formed vasculature (dark curves) ($t \approx 8.00$). Vessel sprouts are also shown as light-colored curves. As the discrete cells evolve, they degrade and remodel the extracellular matrix by laying down fibronectin macromolecule networks. The cells respond to the remodeled microenvironment by forming single-file like strands of pallisading cells from low oxygen (perinecrotic regions) to high oxygen areas ($t \approx 12.00$). As the cells reach oxygen-releasing vessels, their motility is downgraded and their proliferation is upgraded. As the cell density increases, the discrete cells are converted to continuum mass ($t \approx 16.00$). Tumor microsatellites can be seen forming around the neovasculature ($t \approx 20.00$). The vasculature responds to the cell-proliferation pressure, with vessels shutting off and the vasculature regressing if the cell pressure is sufficiently high. This can be seen to occur around some of the newly formed continuum clusters ($t \approx 24.00$).

The resulting multifocal tumor morphology is more complex than in the previous cases. The results compare well with histopathology data for human brain tumor specimens, including the growth of tumor cell clusters “cuffing” conducting blood vessels (Frieboes et al., 2007) and the infiltration of cell strands that move away from the bulk tumor into healthy tissue in regions where neovascularization has not yet occurred (Bearer et al., 2009).

6 Summary and Future Work

This work provides evidence that cancer invasion may be a predictable and quantifiable function of heterogeneity in the 3D tumor cellular microenvironment, beyond and in addition to the particular genetic and phenotypic characteristics of individual tumor cells. Through the model we show that specific forms of tumor invasion driven by downregulation of cell proliferation and upregulation of motility can be quantitatively linked to the effects of heterogeneity in cell substrates, such as oxygen and nutrients. The results are in agreement with recently obtained experimental and clinical data (e.g., Frieboes et al. (2007); Bearer et

al. (2009)). Tumor formation requires genetically damaged cells that proliferate when they should not, or that survive when they should die. Cellular malfunction in turn creates local environmental conditions that chronically challenge cell homeostasis, e.g., hypoxia and acidosis. In response, further genetic and epigenetic changes may be triggered in order to promote survival under these extreme conditions. These changes modulate cell proliferation and cell substrate uptake, as well as migration. This understanding supports the notion of restraining tumor invasion through normalization of vasculature (Jain, 2001b; Pennacchietti et al., 2003; Cristini et al., 2005) and the microenvironment (Nelson and Bissell, 2006; Kenny et al., 2007; Spencer et al., 2007). This concept of tumor progression does not alter the fundamental role of genetic malfunction or phenotypic change in cancer, particularly in tumorigenesis; rather, it supports the idea that genetic and epigenetic changes during the course of cancer progression are also a *means to an end*, namely, survival of cells in stressful conditions.

Recent experiments (Gatenby et al., 2006) indicate that the tumor morphological instability predicted by the model may occur *in vivo*. Boundaries of tumors grown subcutaneously in a mouse model, visible through a dorsal window, show the formation of “bulbs” growing outward (corresponding to a low wavenumber instability (Cristini et al., 2003)) towards regions of higher cell substrates as the mass develops. The boundaries also contain a fractal component, mainly noise, at a smaller, cellular scale. Variations in values of pH, measured inside and outside the tumors, suggest corresponding variations in cell substrates, e.g., glucose, since pH can be a measure of metabolic activity as a result of nutrient consumption (Alberts et al., 2002). Oxygen tension levels may also follow pH trends (Carlsson and Acker, 1988), although there is evidence that local pH and pO_2 levels may not always correlate (Helmlinger et al., 1997). The experimental data (Gatenby et al., 2006) show that whereas pH levels are fairly uniform outside the tumor, there exist wide variations inside the tumor mass. Corresponding variations of cell substrates inside the tumor are expected as well, leading to tumor regions proliferating faster than others. This differential proliferation (Cristini et al., 2005) may cause the formation of tumor bulbs that grow to become unstable, as predicted by the model and *in vitro* experiments (Frieboes et al., 2006).

Note that in our simulations, the vessel shutdown is overestimated as we focus on the effects of vascular and cell substrate inhomogeneity on tumor morphology. Also, for simplicity the effects of tumor fibronectin degradation and MDE production were not included in the simulations; results including these effects are for the most part qualitatively similar to Macklin et al. (2009).

The complex interplay of molecular- and tissue-scale dynamics in cancer may have profound, unforeseen effects on therapy, suggesting the need for more physically based, fully two- and three-dimensional modeling of tumors that can help to develop new therapy strategies to control tumor morphology, e.g., to enforce compact, noninvasive resectable lesions. For example, drug transport to tumors may be compromised by an irregular tumor-generated vasculature (Frieboes et al., 2009; Sinek et al., 2009) and by high interstitial pressure (Jain, 2001a). Nanotechnology has been invoked as a potential remedy to address some of these issues. Nevertheless, using two-dimensional nonlinear simulations, Sinek et al. (2004) predicted that spatially and temporally uniform application of chemotherapeutic drugs via nanoparticles may also lead to tumor fragmentation.

In the future we plan to model the effect of specific genetic mutations on tumor morphology to explore postulated quantitative links between genotype and morphology, and to further study the effects of therapy in the tumor microenvironment. The correspondence between specific genotypic abnormalities and phenotypic characteristics may be unclear, such as the ability to invade or develop resistance to cytotoxic agents (Benjamin et al., 2003). Here, the

model establishes a basic relationship between tumor morphology and phenotype via heterogeneity of the mass exchange and cellular activity such as migration and proliferation and cell substrate uptake rates. From a phenomenological standpoint, these inhomogeneities, which are genetic or epigenetic in origin, are a direct cause of tumor-level invasiveness. While this is consistent with experimental observation, further study is needed to establish a definitive causal link so that morphological characteristics of the tumor boundary may serve as indicators of the underlying cell physiology and be predictive of tumor growth and invasion. Tumor morphology could also be used as a clinical prognostic factor by indicating the extent of hypoxia and, therefore, the potential for tumors to respond to oxygen-dependent treatments.

Here, the results of the simulations could only be quantitatively compared with experimental observations. Informing the model parameters with values measured directly from *in vitro* and *in vivo* data and comparing the model results with the corresponding outcomes is needed to improve the formulation as well as its predictive value. The study of tumor invasion and response to therapy based on these parameters may then ultimately translate into clinical application by providing a means to enable more accurate prognosis and selection of treatment on a patient-specific basis.

Acknowledgments

VC acknowledges partial funding from Cullen Trust for Health Care, Department of Defense, and the NIH. JL acknowledges partial support from the National Institutes of Health (NIH). VC and JL gratefully acknowledge partial support from the National Science Foundation (NSF) Division of Mathematical Sciences. The authors also thank the reviewers for their valuable comments.

References

Abbott R, Forrest S, Pienta K. Simulating the hallmarks of cancer. Art. Lif 2006;12:617–634.

Alarcón T, Byrne H, Maini P. A cellular automaton model for tumour growth in inhomogeneous environment. J. Theor. Biol 2003;225:257–274. [PubMed: 14575659]

Alarcón T, Byrne H, Maini P. A multiple scale model for tumor growth. Multiscale Model. Sim 2005;3:440–475.

Alberts, B.; Johnson, A.; Lewis, J.; Raff, M.; Roberts, K.; Walter, P. Molecular Biology of the Cell. 4th Edition. New York: Garland Science; 2002.

Ambrosi D, Duperray A, Peschetola V, Verdier C. Traction patterns of tumor cells. J. Math. Biol 2009;58:163–181. [PubMed: 18392826]

Ambrosi D, Preziosi L. On the closure of mass balance models for tumor growth. Math. Mod. Meth. Appl. Sci 2002;12:737–754.

Ambrosi D, Preziosi L. Cell adhesion mechanisms and stress relaxation in the mechanics of tumours. Biomech. Model. Mechanobiol 2009;8:397–413. [PubMed: 19115069]

Andersen H, Mejlvang J, Mahmood S, Gromova I, Gromov P, Lukanidin E, Kriajevska M, Mellon J, Tulchinsky E. Immediate and delayed effects of e-cadherin inhibition on gene regulation and cell motility in human epidermoid carcinoma cells. Mol. Cell. Biol 2005;25:9138–9150. [PubMed: 16199889]

Anderson A, Chaplain M. Continuous and discrete mathematical models of tumor-induced angiogenesis. Bull. Math. Biol 1998;60:857–900. [PubMed: 9739618]

Anderson A, Quaranta V. Integrative mathematical oncology. Nature Reviews Cancer 2008;8:227–244.

Anderson A, Weaver A, Commmings P, Quaranta V. Tumor morphology and phenotypic evolution driven by selective pressure from the microenvironment. Cell 2006;127:905–915. [PubMed: 17129778]

Araujo R, McElwain D. A history of the study of solid tumour growth: The contribution of mathematical modelling. Bull. Math. Biol 2004;66:1039–1091. [PubMed: 15294418]

Araujo R, McElwain D. A mixture theory for the genesis of residual stresses in growing tissues I: A general formulation. SIAM J. Appl. Math 2005a;65:1261–1284.

Araujo R, McElwain D. A mixture theory for the genesis of residual stresses in growing tissues II: Solutions to the biphasic equations for a multicell spheroid. SIAM J. Appl. Math 2005b;66:447–467.

Armstrong N, Painter K, Sherratt J. A continuum approach to modeling cell-cell adhesion. J. Theor. Biol 2006;243:98–113. [PubMed: 16860344]

Astanin S, Tosin A. Mathematical model of tumour cord growth along the source of nutrient. Math. Model. Nat. Phenom 2007;2:153–177.

Augustin H. Tubes, branches, and pillars: The many ways of forming a new vasculature. Circ. Research 2001;89:645–647.

Bartha K, Rieger H. Vascular network remodeling via vessel cooption, regression and growth in tumors. J. Theor. Biol 2006;241:903–918. [PubMed: 16545398]

Bauer T, Liu W, Fan F, Camp E, Yang A, Somcio R, Bucana C, Callahan J, Parry G, Evans D, Boyd D, Mazar A, Ellis L. Targeting of urokinase plasminogen activator receptor in human pancreatic carcinoma cells inhibits c-met- and insulin-like growth factor-1 receptor-mediated migration and invasion and orthotopic tumor growth in mice. Cancer Res 2005;65:7775–7781. [PubMed: 16140945]

Bearer E, Lowengrub J, Chuang Y, Frieboes H, Jin F, Wise S, Ferrari M, Agus D, Cristini V. Multiparameter computational modeling of tumor invasion. Cancer Res 2009;69:4493–4501. [PubMed: 19366801]

Bello L, Lucini V, Costa F, Pluderi M, Giussani C, Acerbi F, Carrabba G, Pannacci M, Caronzolo D, Grosso S, Shinkaruk S, Colleoni F, Canron X, Tomei G, Deleris G, Bikfalvi A. Combinatorial administration of molecules that simultaneously inhibit angiogenesis and invasion leads to increased therapeutic efficacy in mouse models of malignant glioma. Clin. Cancer Res 2004;10:4527–4537. [PubMed: 15240545]

Bellomo N, Li N, Maini P. On the foundations of cancer modelling: selected topics, speculations, and perspectives. Math. Models Meth. Appl. Sci 2008;4:593–646.

Benjamin R, Capparella J, Brown A. Classification of glioblastoma multiforme in adults by molecular genetics. The Cancer Journal 2003;9:82–90. [PubMed: 12784873]

Bertuzzi A, Fasano A, Gandolfi A. A mathematical model for tumor cords incorporating the flow of interstitial fluid. Math. Models Meth. Applied Sci 2005;11:1735–1777.

Breward C, Byrne H, Lewis C. The role of cell-cell interactions in a two-phase model for avascular tumour growth. J. Math. Biol 2002;45:125–152. [PubMed: 12181602]

Breward C, Byrne H, Lewis C. A multiphase model describing vascular tumor growth. Bull. Math. Biol 2003;65:609–640. [PubMed: 12875336]

Brizel D, Scully S, Harrelson J, Layfield L, Bean J, Prosnitz L, Dewhirst M. Tumor oxygenation predicts for the likelihood of distant metastases in human soft tissue sarcoma. Cancer Res 1996;56:941–943. [PubMed: 8640781]

Brizel D, Sibley G, Prosnitz L, Scher R, Dewhirst M. Tumor hypoxia adversely affects the prognosis of carcinoma of the head and neck. Int. J. Radiat. Oncol. Biol. Phys 1997;38:285–289. [PubMed: 9226314]

Bussolino, F.; Arese, M.; Audero, E.; Giraudo, E.; Marchiò, S.; Mitola, S.; Primo, L.; Serini, G. Biological Aspects of Tumour Angiogenesis. Vol. Ch. 1. London: Chapman and Hall/CRC; 2003. Cancer Modelling and Simulation; p. 1-22.

Byrne H, Alarcón T, Owen M, Webb S, Maini P. Modeling aspects of cancer dynamics: A review. Phi. Trans. R. Soc. A 2006;364:1563–1578.

Byrne H, Chaplain M. Growth of nonnecrotic tumors in the presence and absence of inhibitors. Mathl. Biosci 1995;130:151–181.

Byrne H, Chaplain M. Growth of necrotic tumors in the presence and absence of inhibitors. Mathl. Biosci 1996;135:187–216.

Byrne H, King J, McElwain D, Preziosi L. A two-phase model of solid tumour growth. Appl. Math. Letters 2003;16:567–573.

Byrne H, Preziosi L. Modelling solid tumour growth using the theory of mixtures. Math. Med. Biol 2003;20:341–366. [PubMed: 14969384]

Cairns R, Kalliomaki T, Hill R. Acute (cyclic) hypoxia enhances spontaneous metastasis of kht murine tumors. Cancer Res 2001;61:8903–8908. [PubMed: 11751415]

Carlsson J, Acker H. Relations ph, oxygen partial pressure and growth in cultured cell spheroids. Int. J. Cancer 1988;42:715–720. [PubMed: 3182108]

Chaplain M, Graziano L, Preziosi L. Mathematical modelling of the loss of tissue compression responsiveness and its role in solid tumor development. Math. Med. Biol 2006;23:197–229. [PubMed: 16648146]

Condeelis J, Singer R, Segall J. The great escape: When cancer cells hijack the genes for chemotaxis and motility. Annu. Rev. Cell Dev. Biol 2005;21:695–718. [PubMed: 16212512]

Cristini V, Frieboes H, Gatenby R, Caserta S, Ferrari M, Sinek J. Morphologic instability and cancer invasion. Clin. Cancer Res 2005;11:6772–6779. [PubMed: 16203763]

Cristini, V.; Frieboes, H.; Li, X.; Lowengrub, J.; Macklin, P.; Sanga, S.; Wise, S.; Zheng, X. Nonlinear modeling and simulation of tumor growth. In: Bellomo, N.; Chaplain, M.; de Angelis, E., editors. Modelling and simulation in science, engineering and technology. Boston: Birkhaeuser; 2008. p. 113-182.

Cristini V, Li X, Lowengrub J, Wise S. Nonlinear simulations of solid tumor growth using a mixture model: invasion and branching. J. Math. Biol 2009;58:723–763. [PubMed: 18787827]

Cristini V, Lowengrub J, Nie Q. Nonlinear simulation of tumor growth. J. Math. Biol 2003;46:191–224. [PubMed: 12728333]

Debnath J, Brugge J. Modelling glandular epithelial cancers in three-dimensional cultures. Nature Reviews Cancer 2005;5:675–688.

Debnath J, Mills K, Collins N, Reginato M, Muthuswarmy S, Brugge J. The role of apoptosis in creating and maintaining luminal space within normal and oncogene-expressing mammary acini. Cell 2002;111:29–40. [PubMed: 12372298]

Deisboeck T, Zhang L, Yoon J, Costa J. In silico cancer modeling: is it ready for prime time? Nature Clin. Practice Oncol 2009;6:34–42.

DeJaeger K, Kavanagh M, Hill R. Relationship of hypoxia to metastatic ability in rodent tumors. Br. J. Cancer 2001;84:1280–1285. [PubMed: 11336482]

Derycke L, van Marck V, Depypere H, Bracke M. Molecular targets of growth, differentiation, tissue integrity, and ectopic cell death in cancer cells. Cancer Biother. Radiopharm 2005;20:579–588. [PubMed: 16398610]

Durand R. Intermittent blood flow in solid tumours - an under-appreciated source of 'drug resistance'. Cancer Metastasis Rev 2001;20:57–61. [PubMed: 11831648]

Eble J, Haier J. Integrins in cancer treatment. Curr. Cancer Drug Targets 2006;6:89–105. [PubMed: 16529540]

Elvin P, Garner A. Tumour invasion and metastasis: challenges facing drug discovery. Curr. Opin. Pharmacol 2005;5:374–381. [PubMed: 15955738]

Erler J, Bennewith K, Nicolau M, Dornhoefer N, Kong C, Le Q-T, Chi J-T, Jeffrey S, Giaccia A. Lysyl oxidase is essential for hypoxia-induced metastasis. Nature 2006;440:1222–1226. [PubMed: 16642001]

Esteban M, Maxwell P. If, a missing link between metabolism and cancer. Nature Med 2005;11:1047–1048. [PubMed: 16211034]

Fasano, A.; Bertuzzi, A.; Gandolfi, A. Mathematical modelling of tumour growth and treatment. Springer: Milan, Ch; 2006. Complex systems in biomedicine; p. 71-108.

Forsythe J, Jiang B, Iyer NF, Agani SL, Koos R, Semenza G. Activation of vascular endothelial growth factor gene transcription by hypoxia-inducible factor 1. Mol. Cell. Biol 1996;16:4604–4613. [PubMed: 8756616]

Franks S, Byrne H, King J, Underwood J, Lewis C. Modeling the early growth of ductal carcinoma in situ of the breast. J. Math. Biol 2003a;47:424–452. [PubMed: 14605857]

Franks S, Byrne H, Mudhar H, Underwood J, Lewis C. Mathematical modeling of comedo ductal carcinoma in situ of the breast. Math. Med. Biol 2003b;20:277–308. [PubMed: 14667048]

Frieboes H, Edgerton M, Fruehauf J, Rose F, Worrall L, Gatenby R, Ferrari M, Cristini V. Prediction of drug response in breast cancer using integrative experimental/computational modeling. Cancer Research 2009;69:4484–4492. [PubMed: 19366802]

Frieboes H, Lowengrub J, Wise S, Zheng X, Macklin P, Bearer E, Cristini V. Computer simulation of glioma growth and morphology. NeuroImage 2007;37:S59–S70. [PubMed: 17475515]

Frieboes H, Zheng X, Sun C-H, Tromberg B, Gatenby R, Cristini V. An integrated computational/experimental model of tumor invasion. Cancer Res 2006;66:1597–1604. [PubMed: 16452218]

Friedl P. Prespecification and plasticity: shifting mechanisms of cell migration. Curr. Opin. Cell Biol 2004;16:14–23. [PubMed: 15037300]

Friedl P, Hegerfeldt Y, Tilisch M. Collective cell migration in morphogenesis and cancer. Int. J. Dev. Biol 2004;48:441–449. [PubMed: 15349818]

Friedl P, Noble P, Walton P, Laird D, Chauvin P, Tabah R, Black M, Zaenker K. Migration of coordinated cell clusters in mesenchymal and epithelial cancer explants in vitro. Cancer Res 1995;55:4557–4560. [PubMed: 7553628]

Friedl P, Wolf A. Tumor cell invasion and migration: diversity and escape mechanisms. Nat. Rev. Cancer 2003;3:362–374. [PubMed: 12724734]

Friedman A, Bellomo N, Maini P. Mathematical analysis and challenges arising from models of tumor growth. Math. Models Meth. Appl. Sci 2007;17:1751–1772.

Gatenby R, Gawlinski E, Gmitro A, Kaylor B, Gillies R. Acid-mediated tumor invasion: a multidisciplinary study. Cancer Res 2006;66:5216–5223. [PubMed: 16707446]

Gatenby R, Smallbone K, Maini P, Rose F, Averill J, Nagle R, Worrall L, Gillies R. Cellular adaptations to hypoxia and acidosis during somatic evolution of breast cancer. Br. J. Cancer 2007;97:646–653. [PubMed: 17687336]

Gerisch A, Chaplain M. Mathematical modelling of cancer cell invasion of tissue: local and non-local models and the effect of adhesion. J. Theor. Biol 2008;250:684–704. [PubMed: 18068728]

Giordano S, Zhen Z, Medico E, Gaudino G, Galimi F, Comoglio P. Transfer of motogenic and invasive response to scatter factor/hepatocyte growth factor by transfection of human met protooncogene. Proc. Natl. Acad. Sci. USA 1993;90:649–653. [PubMed: 8380644]

Graeber T, Osmanian C, Jacks T, et al. Hypoxia-mediated selection of cells with diminished apoptotic potential in solid tumors. Nature 1996;379:88–91. [PubMed: 8538748]

Harris A. Hypoxia-a key regulatory factor in tumor growth. Nat. Rev. Cancer 2002;2:38–47. [PubMed: 11902584]

Hashizume H, Baluk P, Morikawa S, McLean J, Thurston G, Roberge S, Jain R, McDonald D. Openings between defective endothelial cells explain tumor vessel leakiness. Am. J. Pathol 2000;156:1363–1380. [PubMed: 10751361]

Hatzikirou H, Deutsch A, Schaller C, Simon M, Swanson K. Mathematical modeling of glioblastoma tumour development: A review. Math. Models Meth. Appl. Sci 2005;15:1779–1794.

Hayot C, Debeir O, Ham PV, Damme MV, Kiss R, Decaestecker C. Characterization of the activities of actin-affecting drugs on tumor cell migration. Toxicol. Appl. Pharma 2006;211:30–40.

Höckel M, Schlenger K, Aral B, Mitze M, Schaffer U, Vaupel P. Association between tumor hypoxia and malignant progression in advanced cancer of the uterine cervix. Cancer Res 1996;56:4509–4515. [PubMed: 8813149]

Höckel M, Schlenger K, Hoeckel S, Vaupel P. Hypoxic cervical cancers with low apoptotic index are highly aggressive. Cancer Res 1999;59:4525–4528. [PubMed: 10493500]

Höckel M, Schlenger K, Vaupel P. Tumor hypoxia: definitions and current clinical, biologic, and molecular aspects. J. Natl. Cancer Inst 2001;93:266–276. [PubMed: 11181773]

Hegerfeldt Y, Tusch M, Brocker E, Friedl P. Collective cell movement in primary melanoma explants: plasticity of cell-cell interaction, 1-integrin function, and migration strategies. Cancer Res 2002;62:2125–2130. [PubMed: 11929834]

Helmlinger G, Yuan F, Dellian M, Jain R. Interstitial ph and po2 gradients in solid tumors in vivo: high-resolution measurements reveal a lack of correlation. Nat. Med 1997;3:177–182. [PubMed: 9018236]

Holash J, Maisonpierre P, Compton D, Boland P, Alexander C, Zagzag D, Yancopoulos G, Wiegand S. Vessel cooption, regression, and growth in tumors mediated by angiopoietins and vegf. Science 1999;284:1994–1998. [PubMed: 10373119]

Huang Q, Shen H, Ong C. Emodin inhibits tumor cell migration through suppression of the phosphatidylinositol 3-kinase-cdc42/rac1 pathway. Cell. Mol. Life Sci 2005;62:1167–1175. [PubMed: 15928809]

Hughes F, Mcculloch A. Quantification of chemotactic response of quiescent and proliferating fibroblasts in boyden chambers by computer-assisted image analysis. J. Histochem. Cytochem 1991;39:243–246. [PubMed: 1987269]

J R, Sameni M, Ziegler G, Sloane B. Pericellular ph affects distribution and secretion of cathepsin b in malignant cells. Cancer Res 1994;54:6517–6625. [PubMed: 7987851]

Jain R. Determinants of tumor blood flow: a review. Cancer Res 1988;48:2641–2658. [PubMed: 3282647]

Jain R. Physiological barriers to delivery of monoclonal antibodies and other macromolecules in tumors. Cancer Res 1990;50:814s–819s. [PubMed: 2404582]

Jain R. Delivery of molecular medicine to solid tumors: lessons from in vivo imaging of gene expression and function. J. Control. Release 2001a;74:7–25. [PubMed: 11489479]

Jain R. Normalizing tumor vasculature with anti-angiogenic therapy: a new paradigm for combination therapy. Nat. Med 2001b;7:987–989. [PubMed: 11533692]

Jain R. Molecular regulation of vessel maturation. Nature Med 2003;9:685–693. [PubMed: 12778167]

Jiang Y, Pjesivac-Grbovic J, Cantrell C, Freyer J. A multiscale model for avascular tumor growth. Biophys. J 2005;89:3884–3894. [PubMed: 16199495]

Kaneko K, Satoh K, Masamune A. T. myosin light chain kinase inhibitors can block invasion and adhesion of human pancreatic cancer cell lines. Pancreas 2002;24:34–41. [PubMed: 11741180]

Keller P, Pampaloni F, Stelzer E. Life sciences require the third dimension. Curr. Op. Cell Biol 2006;18:117–124. [PubMed: 16387486]

Kenny P, Lee G, Bissell M. Targeting the tumor microenvironment. Front. Biosci 2007;12:3468–3474. [PubMed: 17485314]

Kim Y, Stolarska M, Othmer H. A hybrid model for tumor spheroid growth in vitro i: Theoretical development and early results. Math. Meth. App. Sci 2007;17:1773–1798.

Kopfstein L, Christofori G. Metastasis: cell-autonomous mechanisms versus contributions by the tumor microenvironment. Cell. Mol. Life Sci 2006;63:449–468. [PubMed: 16416030]

Krogh A. The number and distribution of capillaries in muscles with calculations of the oxygen pressure head necessary for supplying the tissue. J. Physiol 1919;52:409–415. [PubMed: 16993405]

Kunkel P, Ulbricht U, Bohlen P, M.A. Brockmann RF, Stavrou D, Westphal M, Lamszus K. Inhibition of glioma angiogenesis and growth in vivo by systemic treatment with a monoclonal antibody against vascular endothelial growth factor receptor-2. Cancer Res 2001;61:6624–6628. [PubMed: 11559524]

Lah T, Alonso M, van Noorden C. Antiprotease therapy in cancer: hot or not? Exp. Op. Biol. Ther 2006;6:257–279.

Lamszus K, Kunkel P, Westphal M. Invasion as limitation to anti-angiogenic glioma therapy. Acta Neurochir Suppl 2003;88:169–177. [PubMed: 14531575]

Landau, L. Statistical Physics. Oxford: Butterworth-Heinemann; 1984.

Lee D, Rieger H, Bartha K. Flow correlated percolation during vascular remodeling in growing tumors. Phys. Rev. Lett 2006;96:058104. [PubMed: 16486998]

Less J, Skalak T, Sevick E, Jain R. Microvascular architecture in a mammary carcinoma: branching patterns and vessel dimensions. Cancer Res 1991;51:265–273. [PubMed: 1988088]

Li X, Cristini V, Nie Q, Lowengrub J. Nonlinear three-dimensional simulation of solid tumor growth. Disc. Dyn. Contin. Dyn. Syst. B 2007;7:581–604.

Lockett J, Yin S, Li X, Y H, Meng, Sheng S. Tumor suppressive maspin and epithelial homeostasis. J. Cell. Biochem 2006;97:651–660. [PubMed: 16329135]

Lowengrub J, Frieboes H, Jin F, Chuang Y, Li X, Macklin P, Wise S, Cristini V. Nonlinear modeling of cancer: Bridging the gap between cells and tumors. Nonlinearity 2010;23:R1–R91.

Macklin P, Lowengrub J. Nonlinear simulation of the effect of microenvironment on tumor growth. J. Theor. Biol 2007;245:677–704. [PubMed: 17239903]

Macklin P, McDougall S, Anderson A, Chaplain M, Cristini V, Lowengrub J. Multiscale modeling and nonlinear simulation of vascular tumour growth. J. Math. Biol 2009;58:765–798. [PubMed: 18781303]

McDougall S, Anderson A, Chaplain M. Mathematical modeling of dynamic adaptive tumour-induced angiogenesis: Clinical applications and therapeutic targeting strategies. J. Theor. Biol 2006;241:564–589. [PubMed: 16487543]

McDougall S, Anderson A, Chaplain M, Sherratt J. Mathematical modelling of flow through vascular networks: implications for tumour-induced angiogenesis and chemotherapy strategies. Bull. Math. Biol 2002;64:673–702. [PubMed: 12216417]

McLean G, Carragher N, Avizienyte E, Evans J, Brunton V, Frame M. The role of focal-adhesion kinase in cancer: A new therapeutic opportunity. Nat. Rev. Cancer 2005;5:505–515. [PubMed: 16069815]

Nagy J. The ecology and evolutionary biology of cancer: A review of mathematical models of necrosis and tumor cell diversity. Math. Biosci. Eng 2005;2:381–418. [PubMed: 20369929]

Nelson C, Bissell M. Of extracellular matrix, scaffolds, and signaling: tissue architecture regulates development, homeostasis, and cancer. Annu. Rev. Cell Dev. Biol 2006;22:287–309. [PubMed: 16824016]

Owen M, Alarcón T, Maini P, Byrne H. Angiogenesis and vascular remodeling in normal and cancerous tissues. J. Math. Biol 2009;58:689–721. [PubMed: 18941752]

Palka J, Adelmann-Grill B, Francz P, Bayreuther K. Differentiation stage and cell cycle position determine the chemotactic response of fibroblasts. Folia Histochem. Cytobiol 1996;34:121–127. [PubMed: 8967956]

Pennacchietti S, Michieli P, Galluzzo M, Giordano S, Comoglio P. Hypoxia promotes invasive growth by transcriptional activation of the met protooncogene. Cancer Cell 2003;3:347–361. [PubMed: 12726861]

Pettet G, Please C, Tindall M, McElwain D. The migration of cells in multicell tumor spheroids. Bull. Math. Biol 2001;63:231–257. [PubMed: 11276525]

Plank M, Sleeman B. A reinforced random walk model of tumour angiogenesis and anti-angiogenic strategies. Math. Med. Biol 2003;20:135–181. [PubMed: 14636027]

Plank M, Sleeman B. Lattice and non-lattice models of tumour angiogenesis. Bull. Math. Biol 2004;66:1785–1819. [PubMed: 15522355]

Please C, Pettet G, McElwain D. A new approach to modeling the formation of necrotic regions in tumors. Appl. Math. Lett 1998;11:89–94.

Please C, Pettet G, McElwain D. Avascular tumour dynamics and necrosis. Math. Models Appl. Sci 1999;9:569–579.

Polette M, Gilles C, de Bentzmann S, Gruenert D, Tournier J, Birembaut P. Association of fibroblastoid features with the invasive phenotype in human bronchial cancer cell lines. Clin. Exp. Metastasis 1998;16:105–112. [PubMed: 9514091]

Postovit L, Adams M, Lash G, Heaton J, Graham C. Oxygen-mediated regulation of tumor cell invasiveness. involvement of a nitric oxide signaling pathway. J. Biol. Chem 2002;277:35730–35737. [PubMed: 12107174]

Preziosi L, Tosin A. Multiphase and multiscale trends in cancer modelling. Math. Model. Nat. Phenom 2009a;4:1–11.

Preziosi L, Tosin A. Multiphase modelling of tumour growth and extracellular matrix interaction: mathematical tools and applications. J. Math. Biol 2009b;58:625–656. [PubMed: 18853162]

Pries A, Secomb T. Modeling structural adaptation of microcirculation. Microcirculation 2008;15:753–764. [PubMed: 18802843]

Pries A, Secomb T, Gaehtgens P. Structural adaptation and stability of microvascular networks: theory and simulations. Am. J. Physiol. Heart Cir. Physiol 1998;275:H349–H360.

Putz E, Witter K, Offner S, P S, Zippelius A, Johnson J, Zahn R, Riethmüller G, Pantel K. Phenotypic characteristics of cell lines derived from disseminated cancer cells in bone marrow of patients with solid epithelial tumors: establishment of working models for human micrometastases. Cancer Res 1999;59:241–248. [PubMed: 9892213]

Quaranta V, Rejniak K, Gerlee P, Anderson A. Invasion emerges from cancer cell adaptation to competitive microenvironments: Quantitative predictions from multiscale mathematical models. Sem. Cancer Biol 2008;18:338–348.

Quaranta V, Weaver A, Cummings P, Anderson A. Mathematical modeling of cancer: The future of prognosis and treatment. Clinica Chimica Acta 2005;357:173–179.

Ramanathan A, Wang C, Schreiber S. Perturbational profiling of a cell-line model of tumorigenesis by using metabolic measurements. PNAS 2005;102:5992–5997. [PubMed: 15840712]

Ribba B, Colin T, Schnell S. A multiscale mathematical model of cancer, and its use in analyzing irradiation therapies. Theor. Biol. Med. Model 2006;3:7. [PubMed: 16472396]

Ridley A, Schwartz M, Burridge K, Firtel R, Ginsberg M, Borisy G, Parsons J, Horwitz A. Cell migration: Integrating signals from front to back. Science 2003;302:1704–1709. [PubMed: 14657486]

Rofstad E, Halsør E. Hypoxia-associated spontaneous pulmonary metastasis in human melanoma xenographs: involvement of microvascular hotspots induced in hypoxic foci by interleukin. Br. J. Cancer 2002;86:301–308. [PubMed: 11870523]

Rofstad E, Rasmussen H, Galappathi K, Mathiesen B, Nilsen K, Graff B. Hypoxia promotes lymph node metastasis in human melanoma xenografts by up-regulating the urokinase-type plasminogen activator receptor. Cancer Res 2002;62:1847–1853. [PubMed: 11912164]

Roose T, Chapman SJ, Maini P. Mathematical models of avascular tumor growth. SIAM Review 2007;49:179–208.

Roose T, Netti P, Munn L, Boucher Y, Jain R. Solid stress generated by spheroid growth using a linear poroelastic model. Microvascular Res 2003;66:204–212.

Rowlinson, J.; Widom, B. Molecular Theory of Capillarity. Oxford: Clarendon Press; 1982.

Rubenstein J, Kim J, Ozawa T, Zhang K, Westphal M, Deen D, Shuman M. Anti-vegf antibody treatment of glioblastoma prolongs survival but results in increased vascular cooption. Neoplasia 2000;2:306–314. [PubMed: 11005565]

Sahai E. Mechanisms of cancer cell invasion. Curr. Opin. Genet. Dev 2005;15:87–96. [PubMed: 15661538]

Sanga S, Frieboes H, Zheng X, Gatenby R, Bearer E, Cristini V. Predictive oncology: a review of multidisciplinary, multiscale in silico modeling linking phenotype, morphology and growth. NeuroImage 2007;37:S120–S134. [PubMed: 17629503]

Sanga S, Sinek J, Frieboes H, Ferrari M, Fruehauf J, Cristini V. Mathematical modeling of cancer progression and response to chemotherapy. Expert Rev. Anticancer Ther 2006;6:1361–1376. [PubMed: 17069522]

Seftor E, Meltzer P, Kirshmann D, Pe'er J, Maniotis A, Trent J, Folberg R, Hendrix M. Molecular determinants of human uveal melanoma invasion and metastasis. Clin. Exp. Metastasis 2002;19:233–246. [PubMed: 12067204]

Shweiki D, Itin A, Soffer D, Keshet E. Vascular endothelial growth factor induced by hypoxia may mediate hypoxia-initiated angiogenesis. Nature 1992;359:843–845. [PubMed: 1279431]

Sierra A. Metastases and their microenvironments: linking pathogenesis and therapy. Drug Resist. Updates 2005;8:247–257.

Sinek J, Frieboes H, Zheng X, Cristini V. Two-dimensional chemotherapy simulations demonstrate fundamental transport and tumor response limitations involving nanoparticles. Biomedical Microdevices 2004;6:297–309. [PubMed: 15548877]

Sinek J, Sanga S, Zheng X, Frieboes H, Ferrari M, Cristini V. Predicting drug pharmacokinetics and effect in vascularized tumors using computer simulation. J. Math. Biol 2009;58:485–510. [PubMed: 18781304]

Skinner S. Microvascular architecture of experimental colon tumors in the rat. Cancer Res 1990;50:2411–2417. [PubMed: 2317825]

Spencer V, Xu R, Bissell M. Extracellular matrix, nuclear and chromatin structure, and gene expression in normal tissues and malignant tumors: a work in progress. Adv. Cancer Res 2007;97:275–294. [PubMed: 17419950]

Stephanou A, McDougall S, Anderson A, Chaplain M. Mathematical modelling of flow in 2d and 3d vascular networks: Applications to anti-angiogenic and chemotherapeutic drug strategies. Math. Comput. Model 2005;41:1137–1156.

Stephanou A, McDougall S, Anderson A, Chaplain M. Mathematical modeling of the influence of blood rheological properties upon adaptive tumour-induced angiogenesis. Math. Comput. Model 2006;44:96–123.

Stolarska M, Kim Y, Othmer H. Multiscale models of cell and tissue dynamics. Phil. Trans. Roy. Soc. A 2009;367:3525–3553. [PubMed: 19657010]

Sun C, Munn L. Lattice-boltzmann simulation of blood flow in digitized vessel networks. Comp. and Math. Appl 2008;55:1594–1600.

Sundfor K, Lyng H, Rofstad E. Tumour hypoxia and vascular density as predictors of metastasis in squamous cell carcinoma of the uterine cervix. Br. J. Cancer 1998;78:822–827. [PubMed: 9743308]

Takano S, Yoshii Y, Kondo S, Suzuki H, Maruno T, Shirai S, Nose T. Concentration of vascular endothelial growth factor in the serum and tumor tissue of brain tumor patients. Cancer Res 1996;56:2185–2190. [PubMed: 8616870]

Tannock I. Tumor physiology and drug resistance. Cancer Metastasis Rev 2001;20:123–132. [PubMed: 11831640]

Tester A, Ruangpani N, Anderson R, Thompson E. Mmp-9 secretion and mmp-2 activation distinguish invasive and metastatic sublines of a mouse mammary carcinoma system showing epithelial-mesenchymal transition traits. Clin. Exp. Metastasis 2000;18:553–560. [PubMed: 11688960]

Tosin A. Multiphase modeling and qualitative analysis of the growth of tumor cords. Networks Heterogen. Media 2008;3:43–84.

Tracqui P. Biophysical models of tumor growth. Rep. Prog. Phys 2009;72:056701.

van Kempen L, Ruiter D, van Muijen G, Coussens L. The tumor microenvironment: a critical determinant of neoplastic evolution. Eur. J. Cell. Biol 2003;82:539–548. [PubMed: 14703010]

Vaupel P, Haugland H, Nicklee T, Morrison A, Hedley D. Hypoxia-inducible factor-1 alpha is an intrinsic marker for hypoxia in cervical cancer xenografts. Cancer Res 2001;61:7394–7398. [PubMed: 11606368]

Ward J, King J. Mathematical modelling of avascular tumour growth. IMA J. Math. Appl. Medicine Biol 1997;14:36–69.

Ward J, King J. Mathematical modelling of avascular-tumour growth ii: modelling growth saturation. Math. Med. Biol 1999;16:171–211.

Welter M, Bartha K, Rieger H. Emergent vascular network inhomogenities and resulting blood flow patterns in a growing tumor. J. Theor. Biol 2008;250:257–280. [PubMed: 17996256]

Wise S, Lowengrub J, Frieboes H, Cristini V. Three-dimensional multispecies nonlinear tumor growth– i. model and numerical method. J. Theor. Biol 2008;253:524–543. [PubMed: 18485374]

Wolf K, Friedl P. Molecular mechanisms of cancer cell invasion and plasticity. Br. J. Dermatology 2006;154:11–15.

Wu, J.; Zhou, F.; Cui, S. Simulation of microcirculation in solid tumors. Complex Med. Eng. 2007; CME 2007. IEEE/ICME Int. Conf.; 2007. p. 1555-1563.

Yamaguchi H, Wyckoff J, Condeelis J. Cell migration in tumors. Curr. Op. Cell Biol 2005;17:559–564. [PubMed: 16098726]

Yin S, Lockett J, Meng Y, Biliran H, Blouse G, Li X, Reddy N, Zhao Z, Lin X, Anagli J, Cher M, Sheng S. Maspin retards cell detachment via a novel interaction with the urokinase-type plasminogen activator/urokinase-type plasminogen activator receptor system. Cancer Res 2006;66:4173–4181. [PubMed: 16618739]

Young S, Hill R. Effects of reoxygenation of cells from hypoxic regions of solid tumors: anticancer drug sensitivity and metastatic potential. J. Natl. Cancer Inst 1990;82:338–339. [PubMed: 2406450]

Young S, Marshall R, Hill R. Hypoxia induces dna overreplication and enhances metastatic potential of murine tumor cells. Proc. Natl. Acad. Sci. USA 1988;85:9533–9537. [PubMed: 3200838]

Yu J, Rak J, Coomber B, Hicklin D, Kerbel R. Effect of p53 status on tumor response to antiangiogenic therapy. Science 2002;295:1526–1528. [PubMed: 11859195]

Zhang L, Strouthos C, Wang Z, Deisboeck T. Simulating brain tumor heterogeneity with a multiscale agent-based model: Linking molecular signatures, phenotypes and expansion rate. Math. Comp. Model 2009;49:307–319.

Zhao G, Wu J, Xu S, Collins M, Long Q, Koenig C, Jiang Y, Wang J, Padhani A. Numerical simulation of blood flow and interstitial fluid pressure in solid tumor microcirculation based on tumor-induced angiogenesis. Mech. Sinica 2007;23:477–483.

Zheng X, Wise S, Cristini V. Nonlinear simulation of tumor necrosis, neo-vascularization and tissue invasion via an adaptive finite-element/level-set method. Bull. Math. Biol 2005;67:211–259. [PubMed: 15710180]

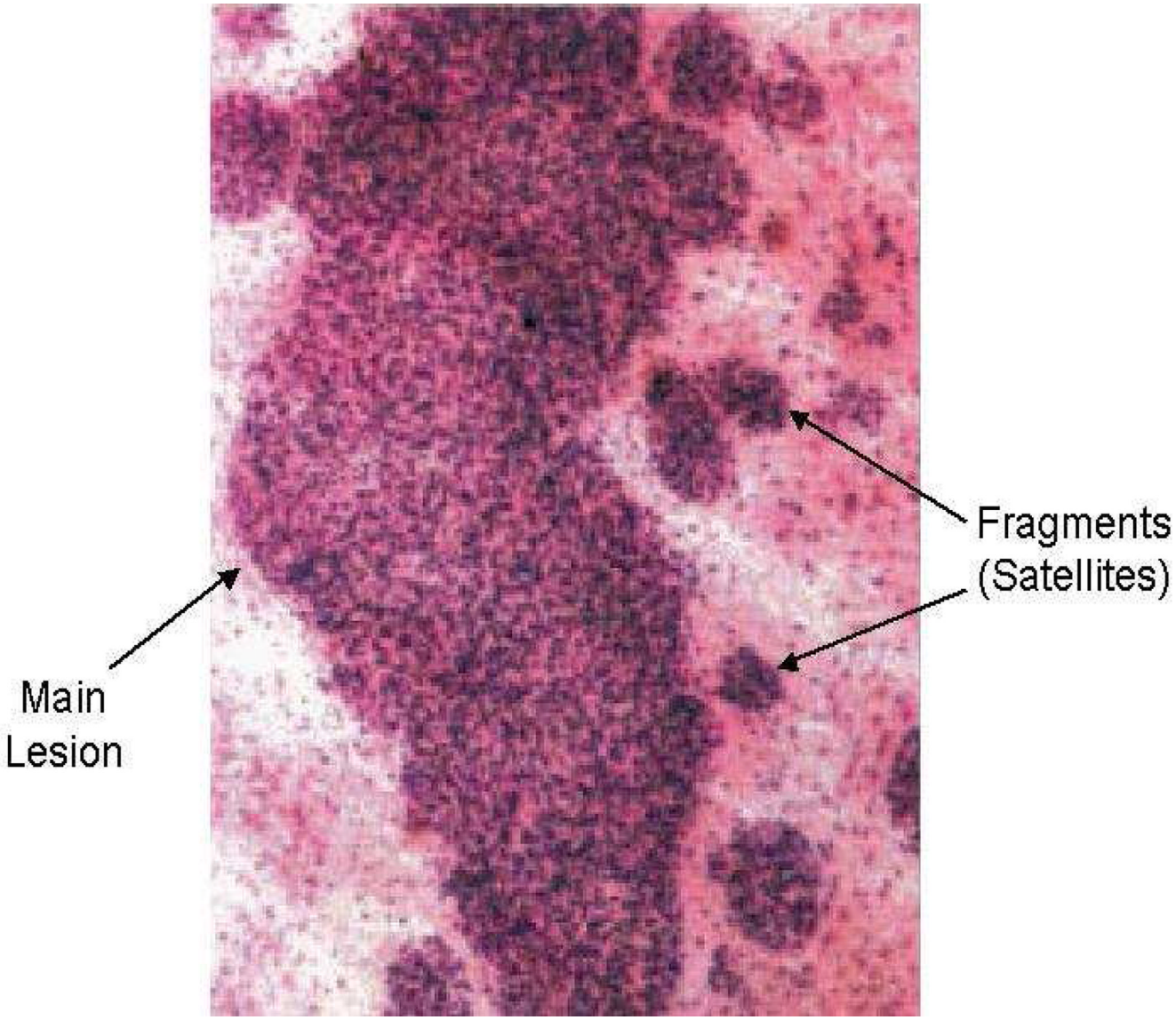

Fig. 1.

Human glioblastoma tumor growing in mice treated with anti-angiogenic therapy. Unlike untreated mice, the tumor is surrounded by numerous smaller satellite tumors that have separated from the main tumor, some of them cuffing around conducting vessels, as well as individual cells. Reprinted from *Cancer Res.*, Vol. 61, Kunkel et al., p. 6626, with permission from the American Association for Cancer Research.

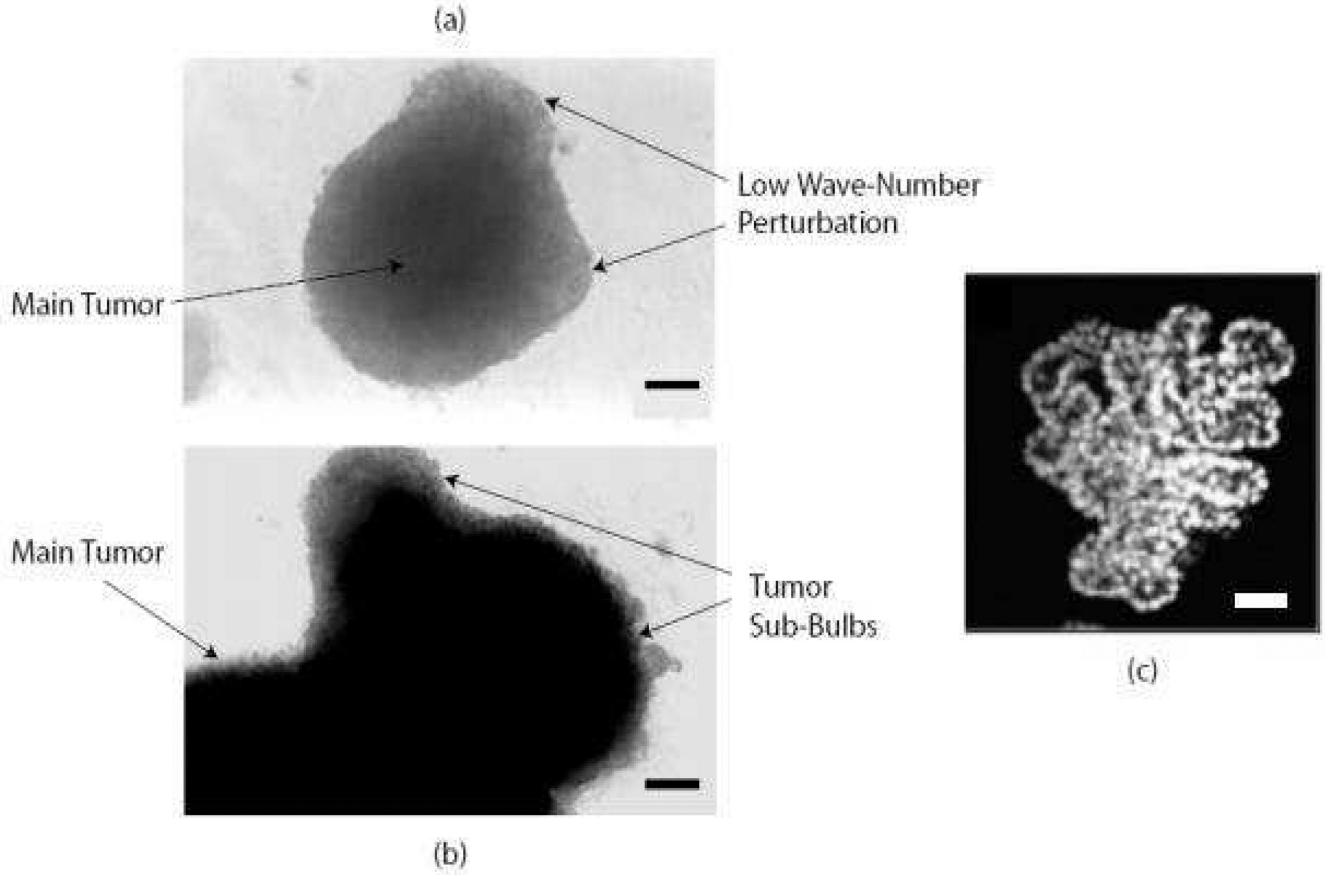

Fig. 2.

Left: human glioblastoma spheroids growing in culture. Low wave-number perturbations on the tumor surface are clearly visible in the top photograph, while recursive bulb formation is observed in the bottom photograph. Bar, 130 μm. Adapted from *Cancer Res.*, Frieboes et al. (Frieboes et al., 2006), with permission from the American Association for Cancer Research. Right: transformed human mammary epithelial cells growing in culture form a complicated structure characterized by recursive acinus formation. Bar, 50 μm. Reprinted with permission from Cell, Vol. 111, Debnath et al., p. 35, Copyright © 2002, with permission from Elsevier.

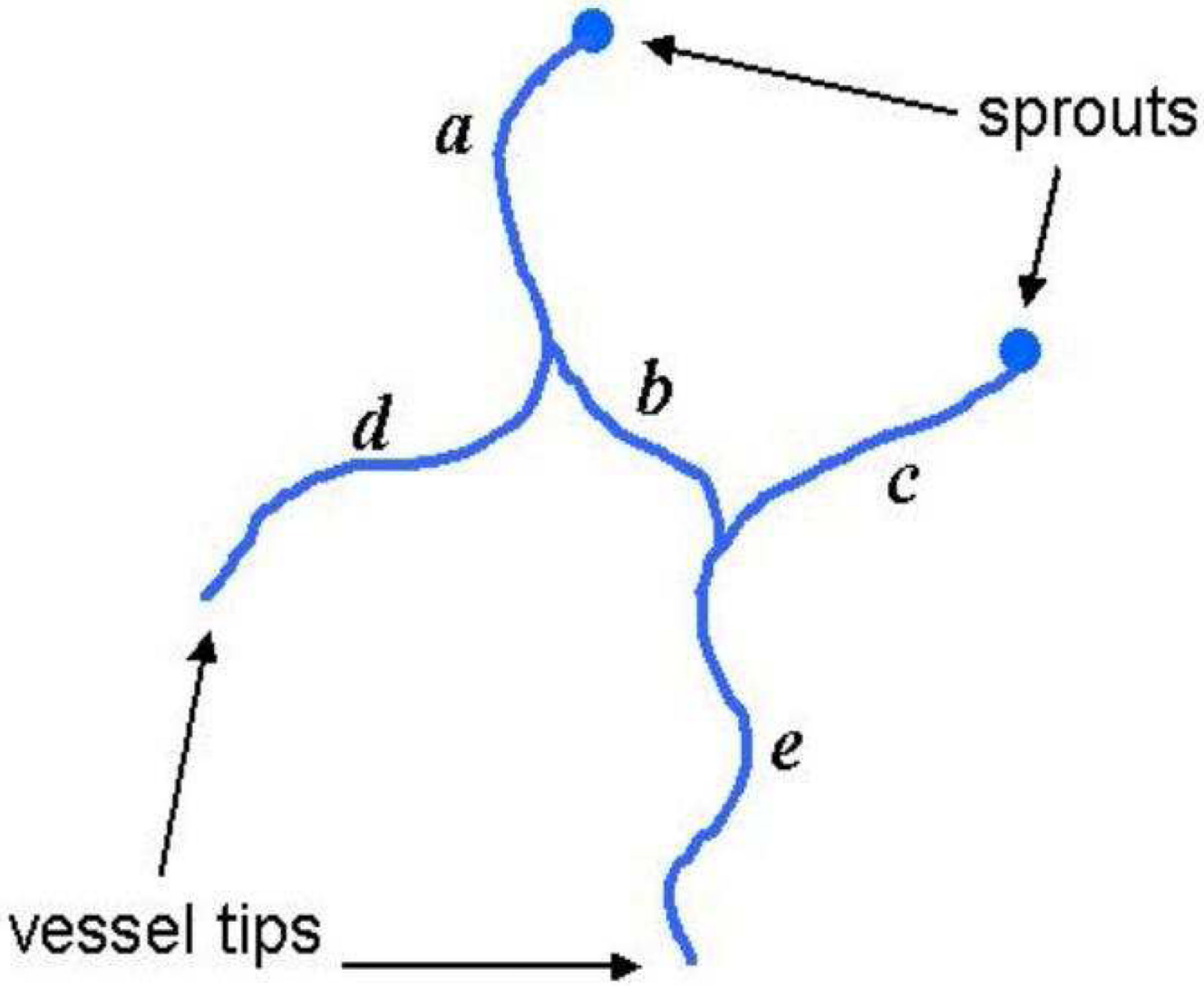

Fig. 3.

Example of vessels and sprouts. The diagram shows two sprouts and five vessels labeled *a* through *e*. A sprout originates from a blood-conducting host vessel (not shown) in response to angiogenic stimuli. In this example, segments *a*, *b*, and *c* form one loop, i.e., they connect two sprouts and can therefore conduct blood. Segments *d* and *e* are open, i.e., without flow. Thus, there are 3 looped (*a*, *b*, and *c*) and two unlooped (*d* and *e*) vessels. In the case that segment *b* were to be crushed by the tumor solid pressure, such as may occur during high proliferation of a viable cell species, the flow would shutdown in segments *a* and *c* in addition to *b*. A shutdown would also occur if segments *a* or *c* were to be crushed.

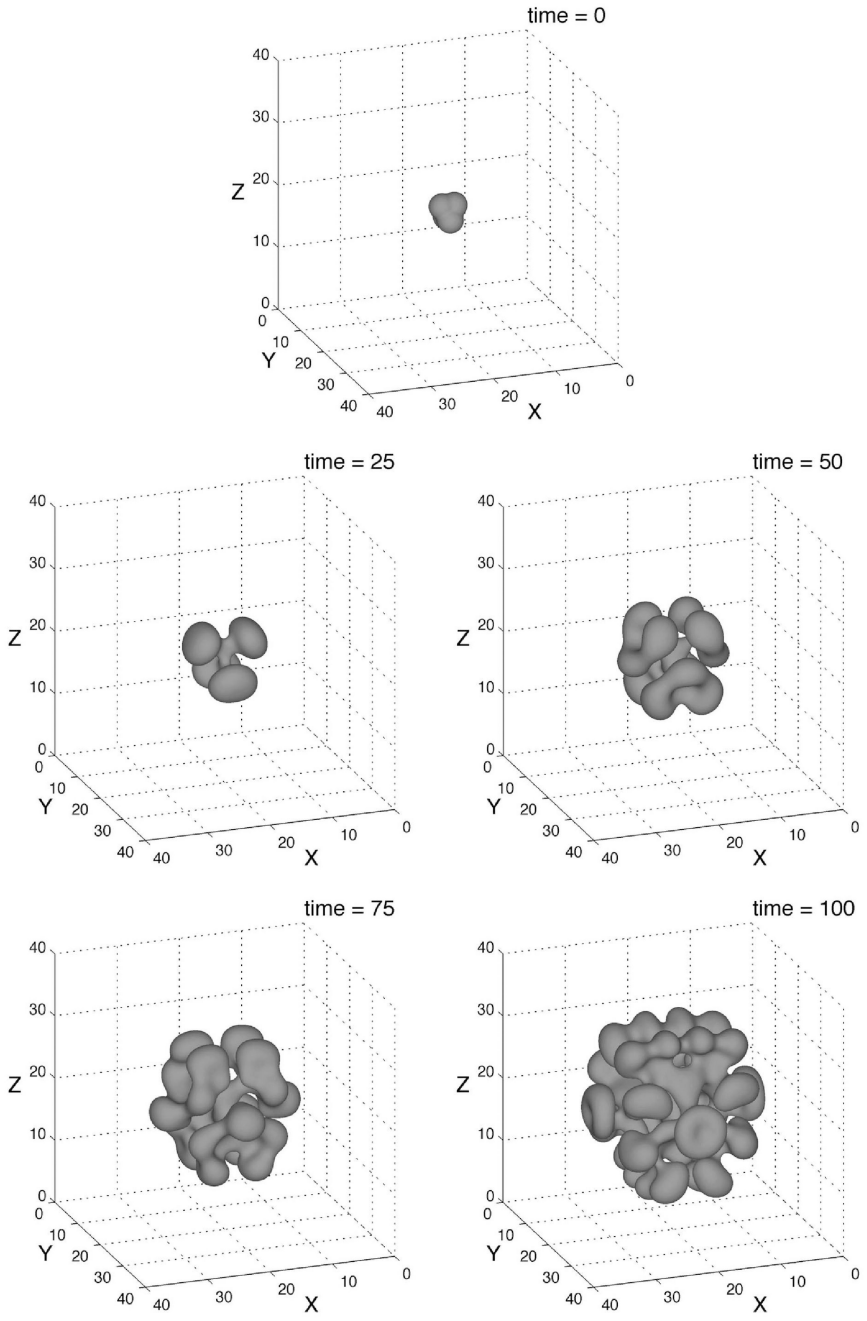

Fig. 4.

Avascular tumor invasion. Growth of a two-plus-four mode avascular tumor in 3-D with low cell adhesion (Part I, $\gamma = 0$). The $\phi_V = 0.5$ isosurface is shown. Parameters are set as in Table 1. The model predicts that this tumor morphological instability, which increases the overall surface area to volume ratio, enables the tumor to improve its access to cell substrates from the surrounding host vasculature (not shown).

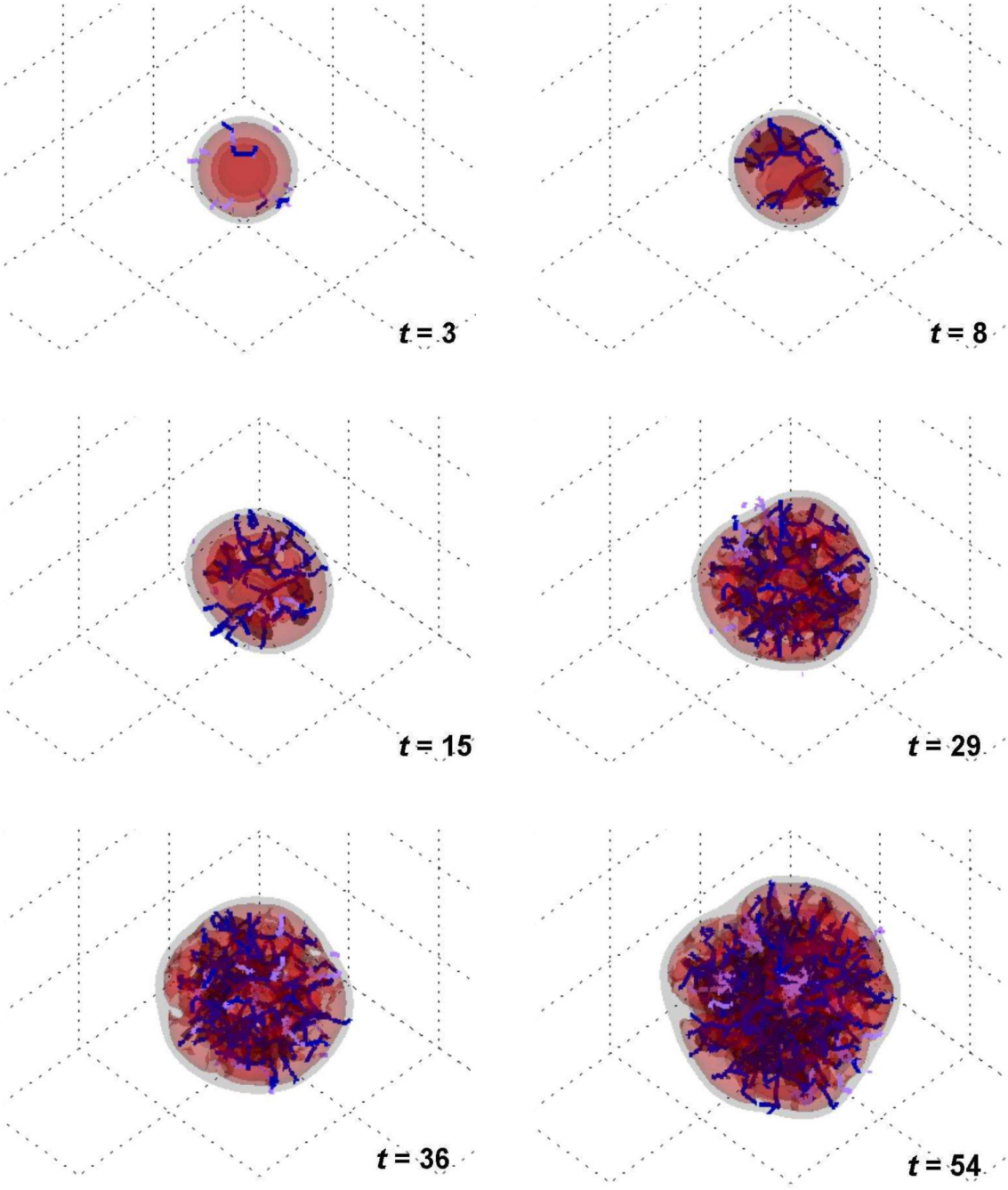

Fig. 5.

Base case without vessel shutdown. Simulation of vascularized tumor growth with one viable cell species. The tumor grows uniformly and compactly over time as the surrounding capillary vasculature is stimulated through angiogenesis to supply it with increasing oxygen and nutrient. Tumor morphological instability is lessened compared to the avascular case in Fig. 4, since hypoxic cells are better able to gain access to oxygen and nutrients. Viable tumor tissue (orange/red color) is shown in 3-D contours representing density values of 0.1, 0.2, and 0.6 (min.: 0.0; max.: 1.0). Conducting vesels: blue; non-conducting: gray. Time unit = 1 day. (Grid length = 500 μ*m*).

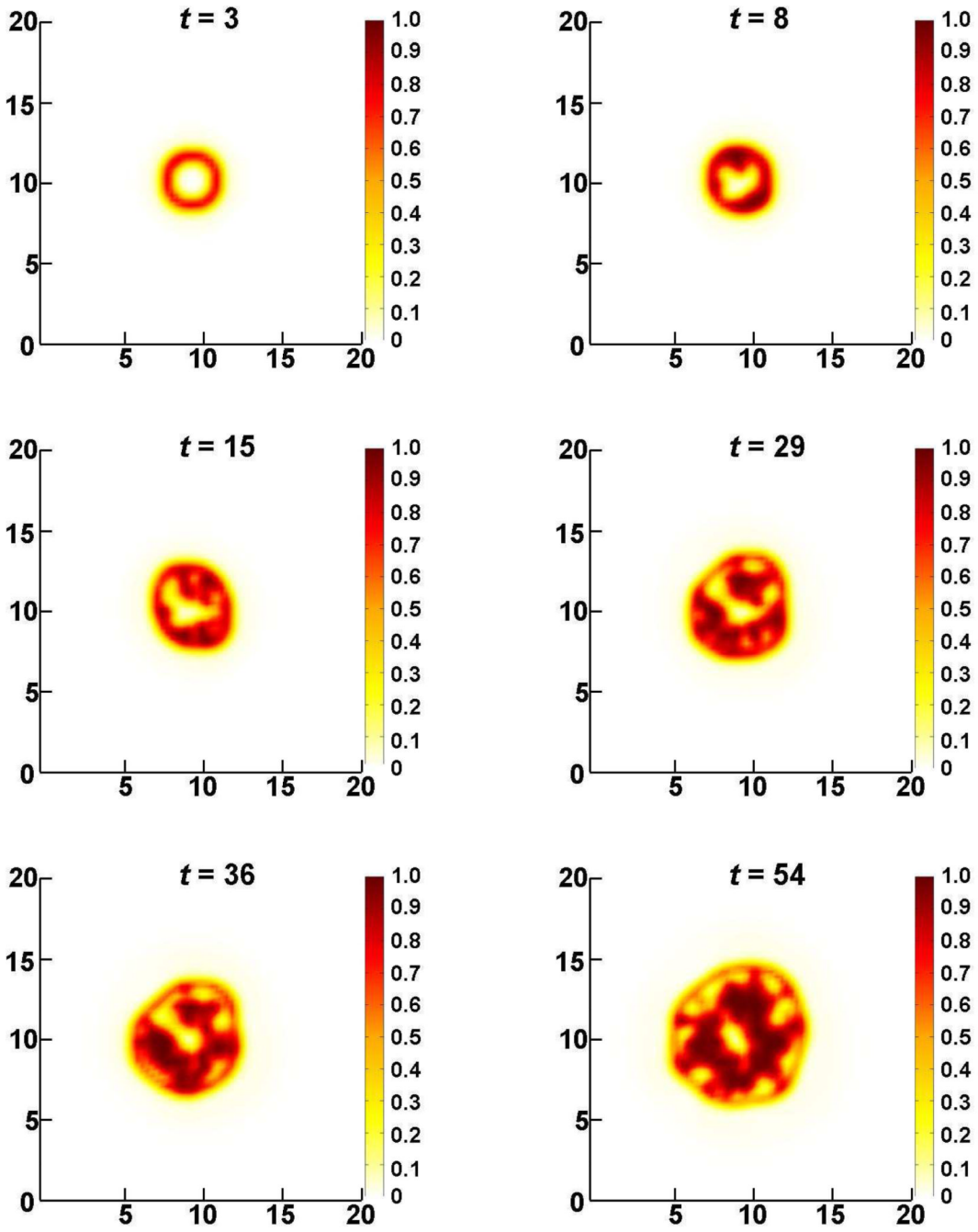

Fig. 6.

Base case without vessel shutdown. Slices of tumor (plane $x = 10$) at various times of growth show that viable tumor tissue cuffs around the vessel locations (darker areas), as observed clinically (Frieboes et al., 2007), with areas more distal from the vessels being dead. Color coding: density of viable tissue; highest=1.0. (Unit length = 100 μ*m*).

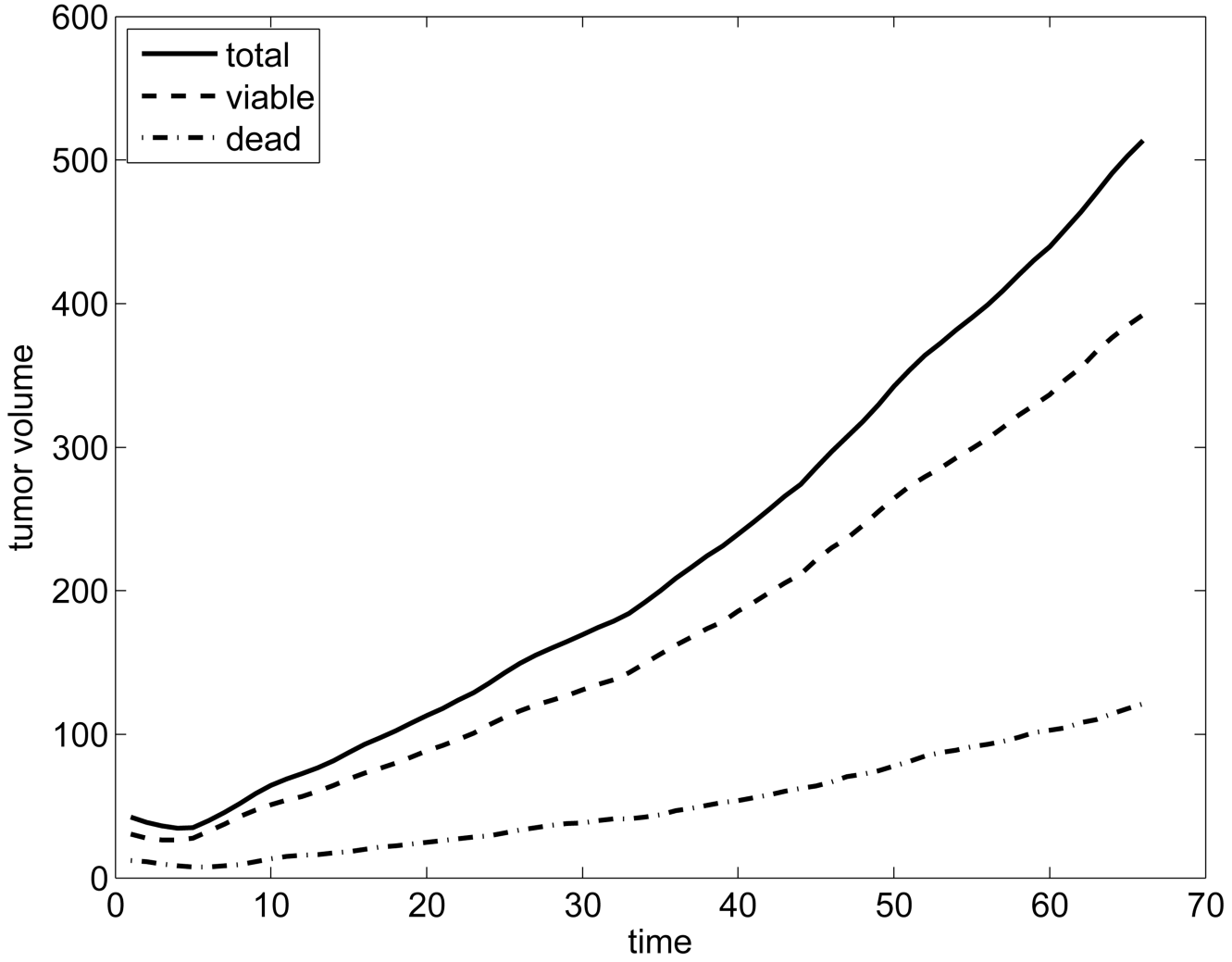

Fig. 7.
Base case without vessel shutdown: tumor volume (unit = 0.001 mm^3) per time.

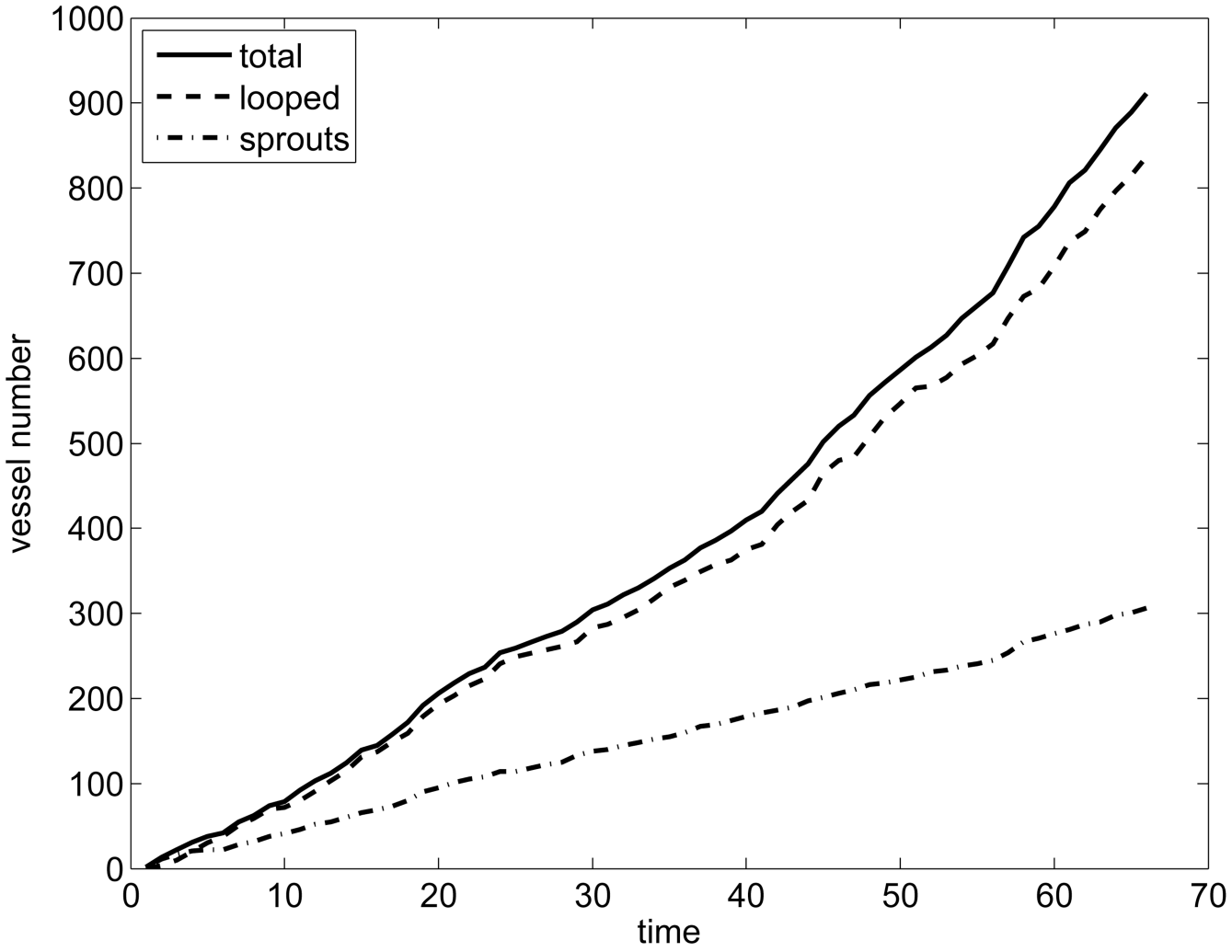

Fig. 8.
Base case without vessel shutdown: number of vessels as a function of time. Looped vessels supply oxygen and nutrients.

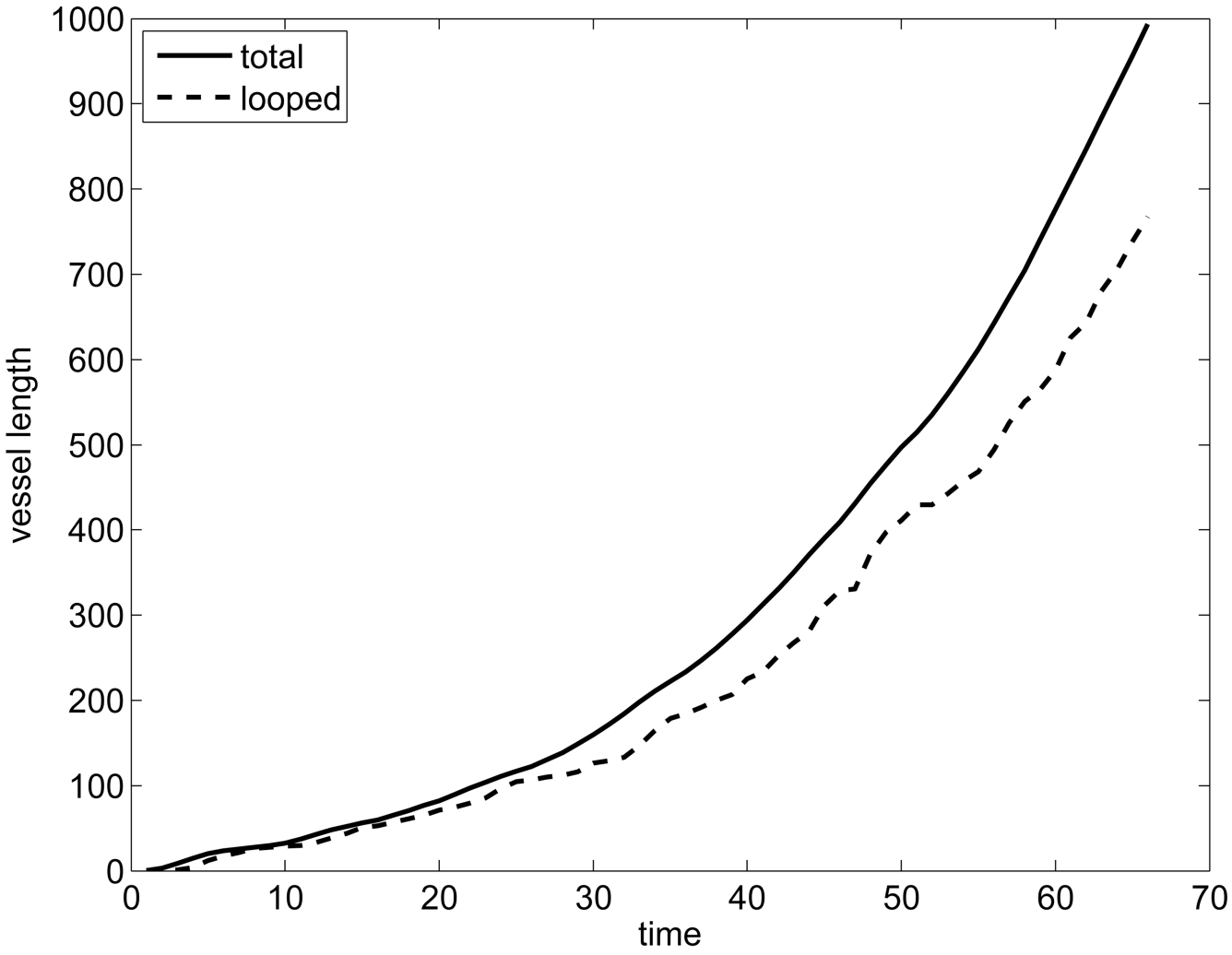

Fig. 9.
Base case without vessel shutdown: growth of the vascular network (unit = 100 μm).

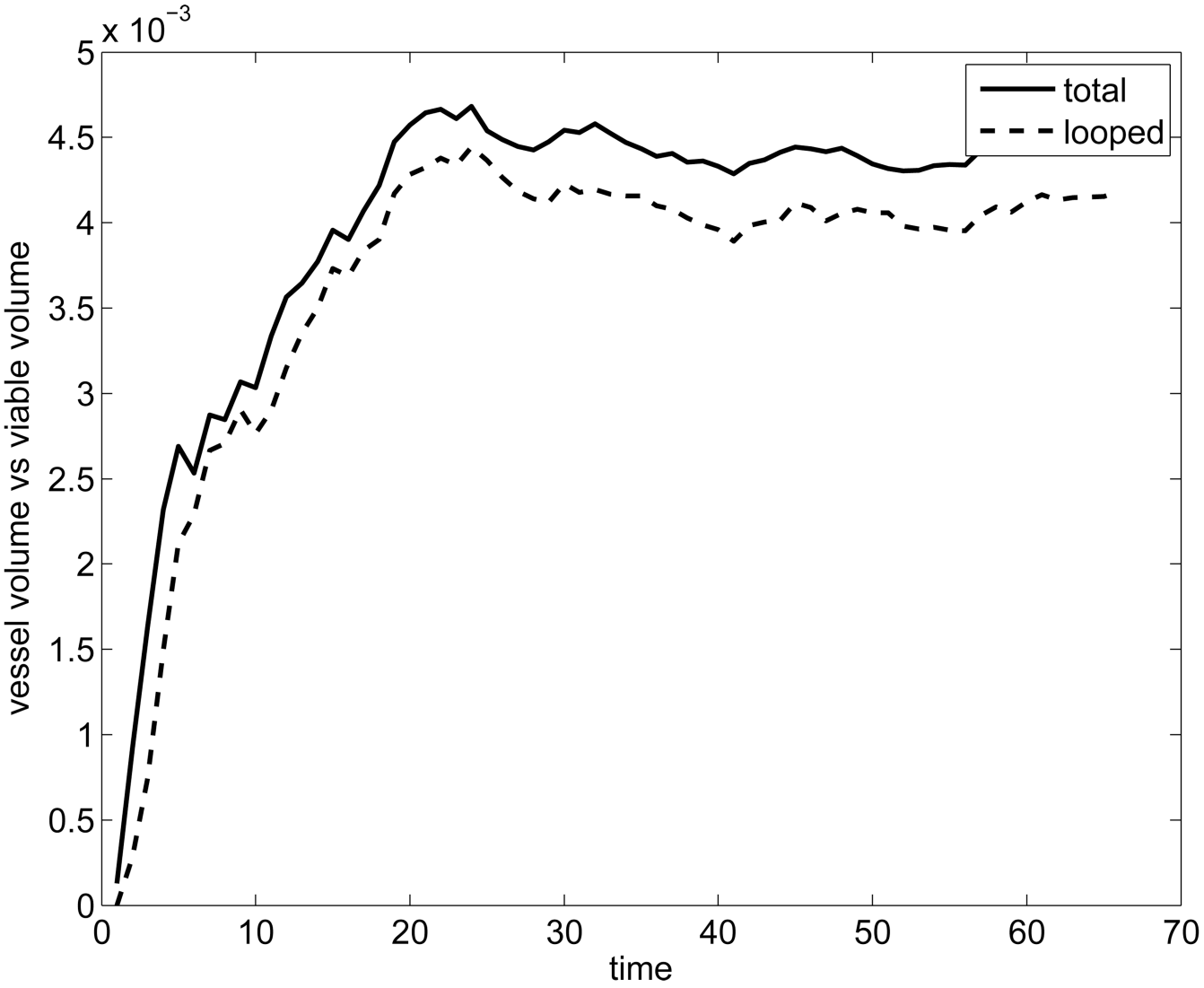

Fig. 10.
Base case without vessel shutdown: vessel volume per viable tumor volume stabilizes after the initial period of angiogenesis.

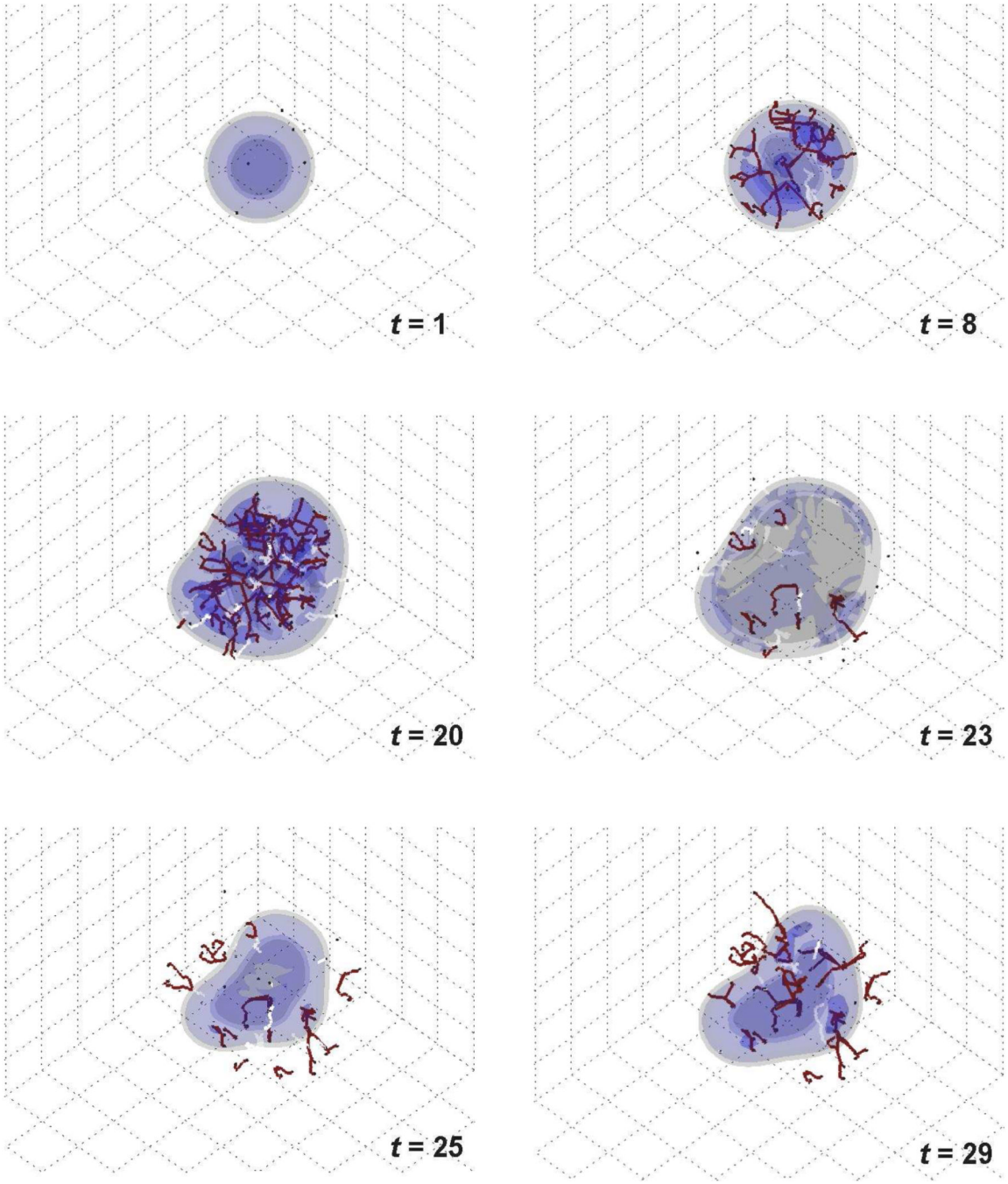

Fig. 11.

Base case with vessel shutdown. Simulation of vascularized tumor growth with one viable cell species. Stability of the tumor morphology and its invasiveness are directly linked to the availability of cell substrates regulated by the dynamically evolving vasculature. At time t = 23, the supply of cell substrates is shut off by the collapse of vessels due to increasing pressure from the surrounding proliferating cells. The tumor mass then undergoes temporary regression (t = 25). By t = 29, neovascularization is apparent in response to the increased hypoxia in the interior of the tumor. Viable tumor tissue (blue color) is shown in 3-D contours representing density values of 0.1, 0.2, and 0.6 (min.: 0.0; max.: 1.0); complete

absence of viable tissue is shown in gray. Conducting vessels: brown; non-conducting: white. Time unit = 1 day. (Grid length = 200 μ*m*).

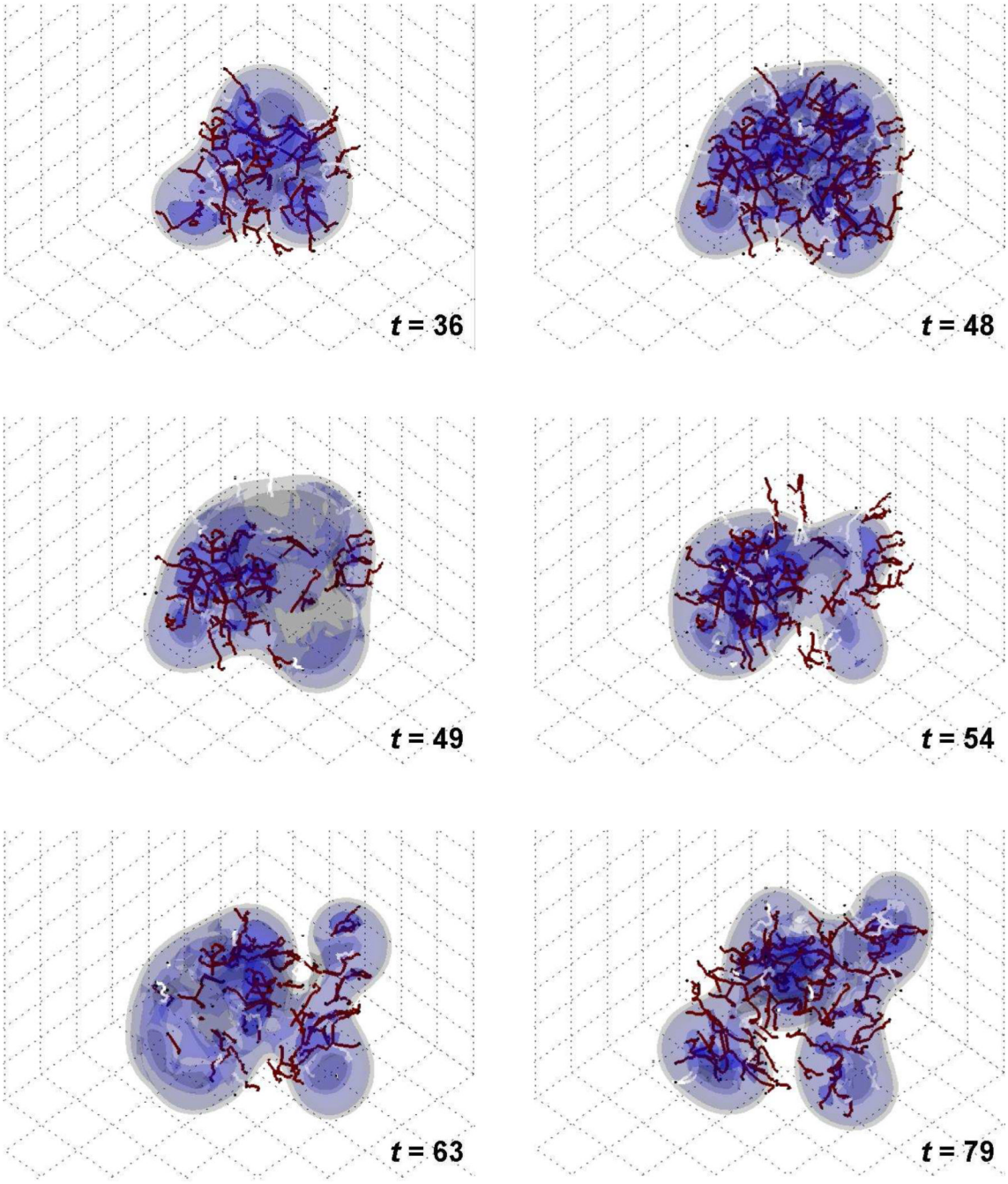

Fig. 12.

Base case with vessel shutdown, continued. By $t = 48$ the tumor has re-grown and is once again highly vascularized. At $t = 49$ the vessels in the right hemisphere are crushed by the tumor cells. The tumor morphology becomes more unstable, breaking up into two pieces ($t = 63$). Renewed vascularization eventually helps to restabilize the mass ($t = 79$). (Grid length = 200 μ*m*).

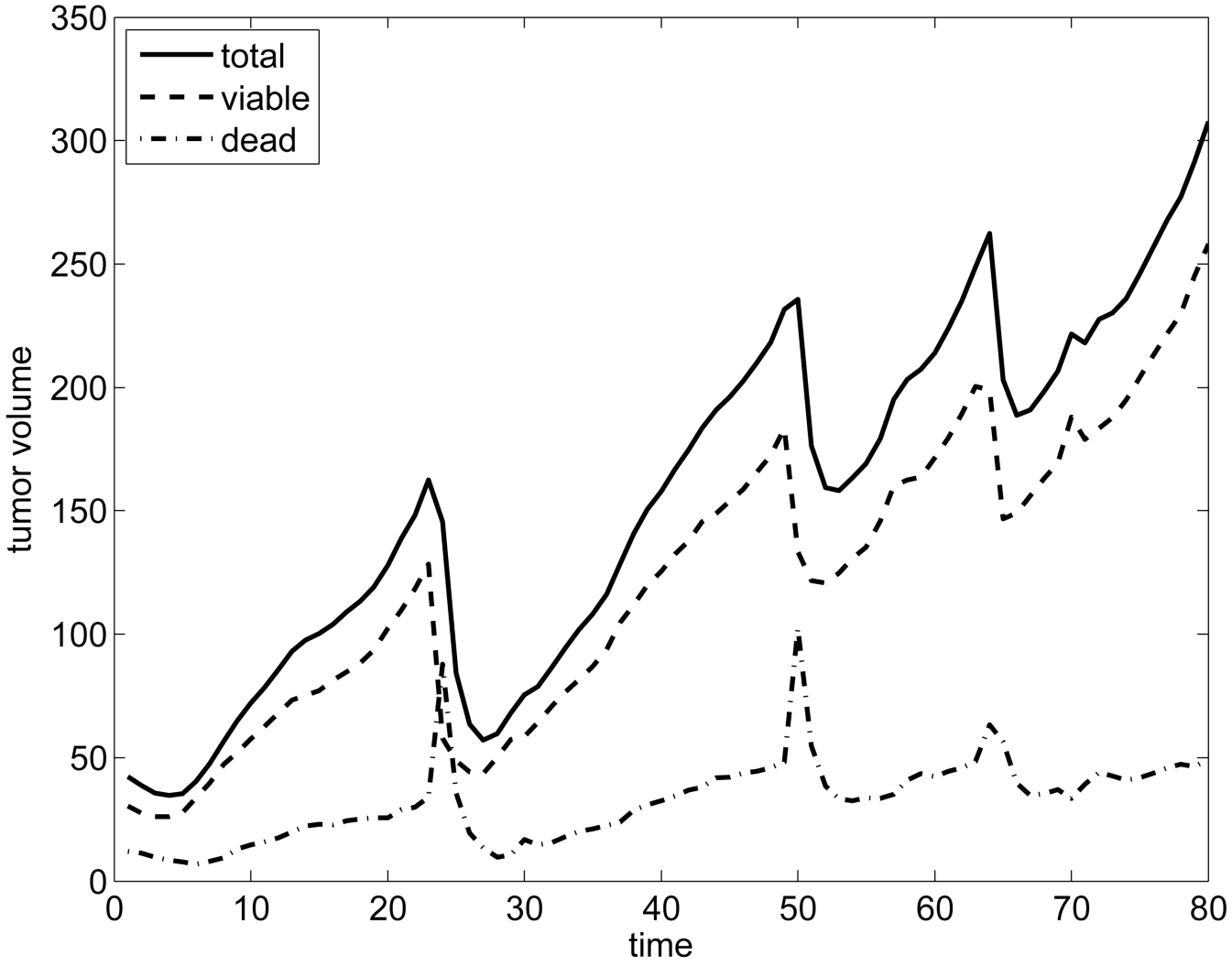

Fig. 13.
Base case with vessel shutdown: tumor volume (unit = 0.001 mm^3) per time. The periods of vessel shutdown and consequent tumor mass regression become apparent at regular intervals. In spite of this effect, the overall trend indicates vigorous mass growth.

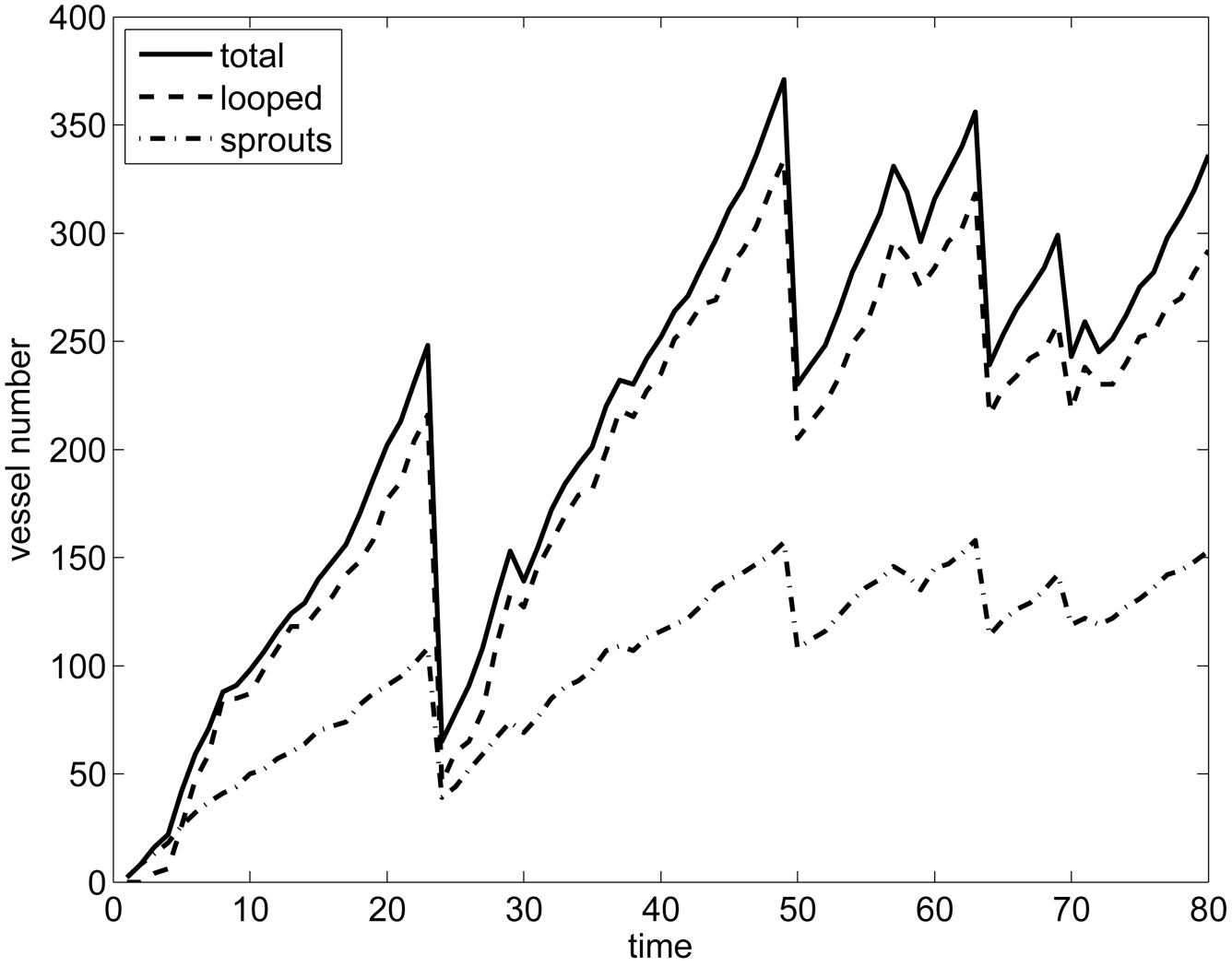

Fig. 14.

Base case with vessel shutdown: number of vessels as a function of time. After an initial rapid increase in vascularization, the number of vessel sprouts stabilizes later in time, while the number of looped vessels oscillates due to branching/anastomosis and periodic shutdown.

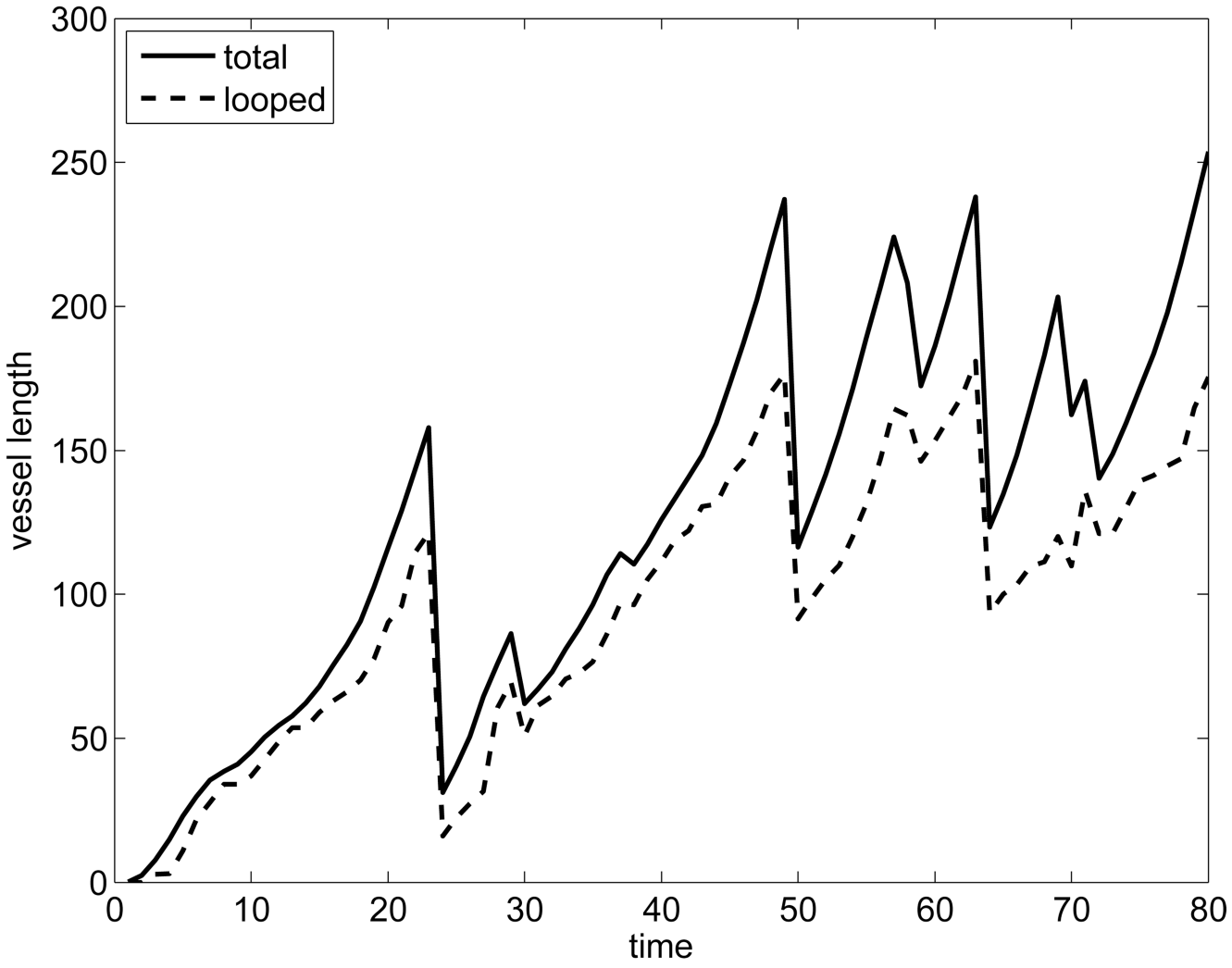

Fig. 15.
Base case with vessel shutdown: the growth of the looped vasculature is very rapid initially, and then seems to stabilize (within a range) at later times (unit = 100 μm).

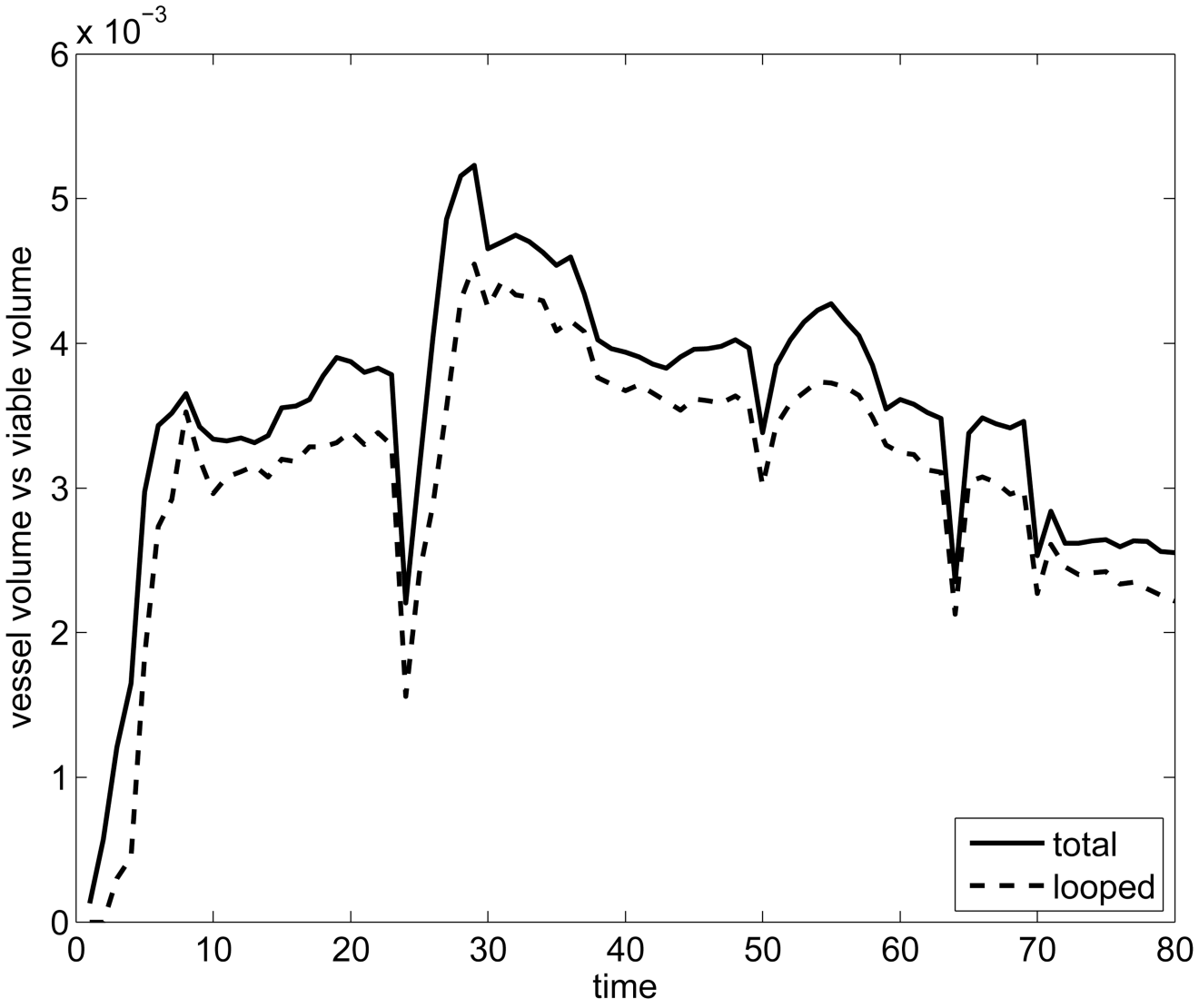

Fig. 16.

Base case with vessel shutdown: vessel volume per viable tumor volume is non-monotone, reflecting a rapid increase in the vascular network at early times to a maximum within a month, and then a slow decrease as the tumor mass fragments, gaining further access to nutrient in the vascularized host tissue surrounding the tumor. Periodic sharp decreases reflect the effects of vessel shutdown with consequent viable tissue loss.

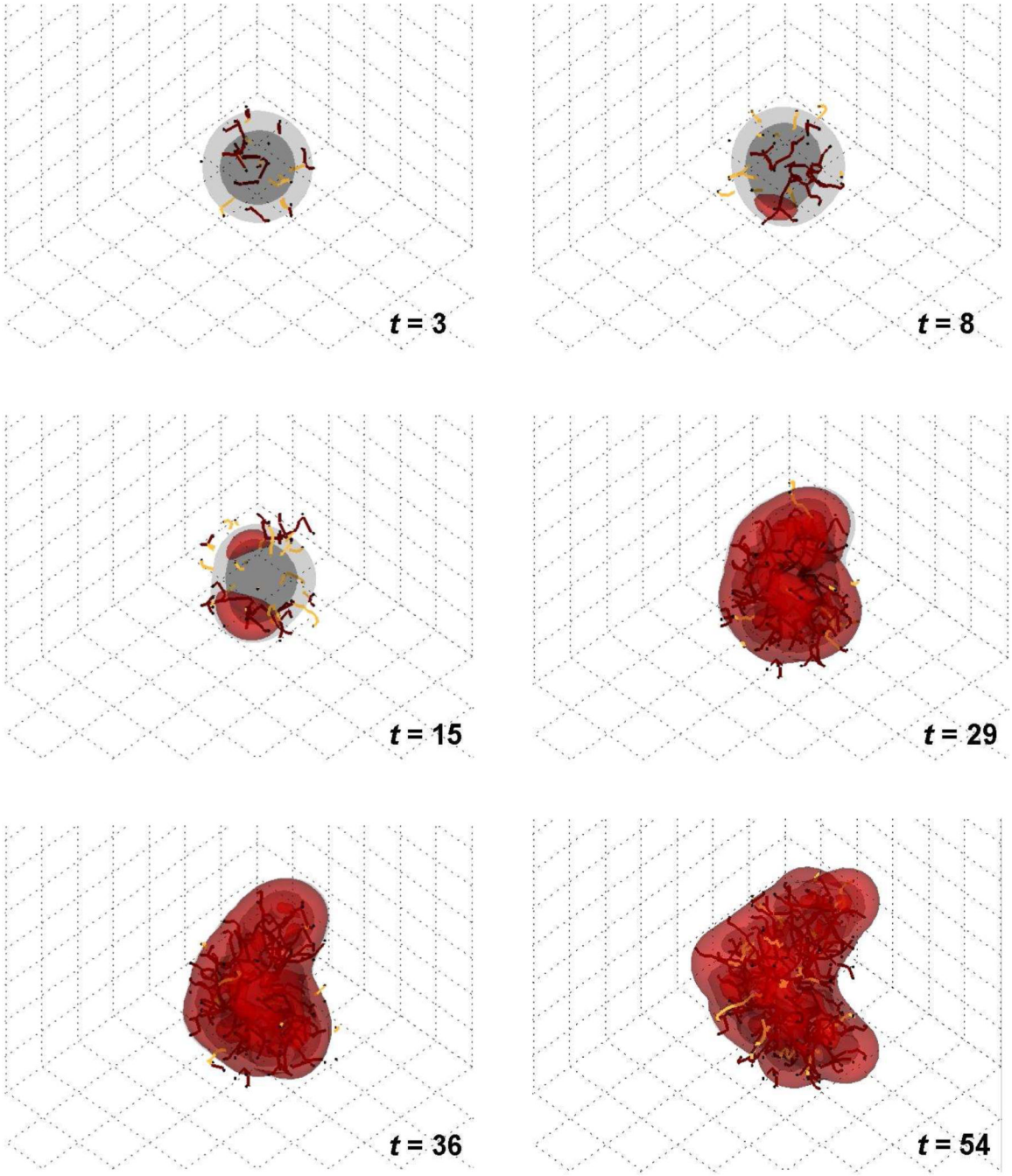

Fig. 17.

Tumor with two viable cell species plus vessel shutdown. The secondary aggressive species (red) activates chemotaxis and upregulates cell substrate uptake and proliferation (1.5× compared to the original species) in order to enhance survival. The secondary species ends up encapsulating the tumor, leading to a morphology that is more stable than in the single species case, yet more invasive than in the case with no vessel shutdown. Original viable tumor tissue (gray color) is shown in 3-D contours representing density values of 0.1, 0.2, and 0.6 (min.: 0.0; max.: 1.0). Conducting vessels: brown; non-conducting: yellow. Time unit = 1 day.

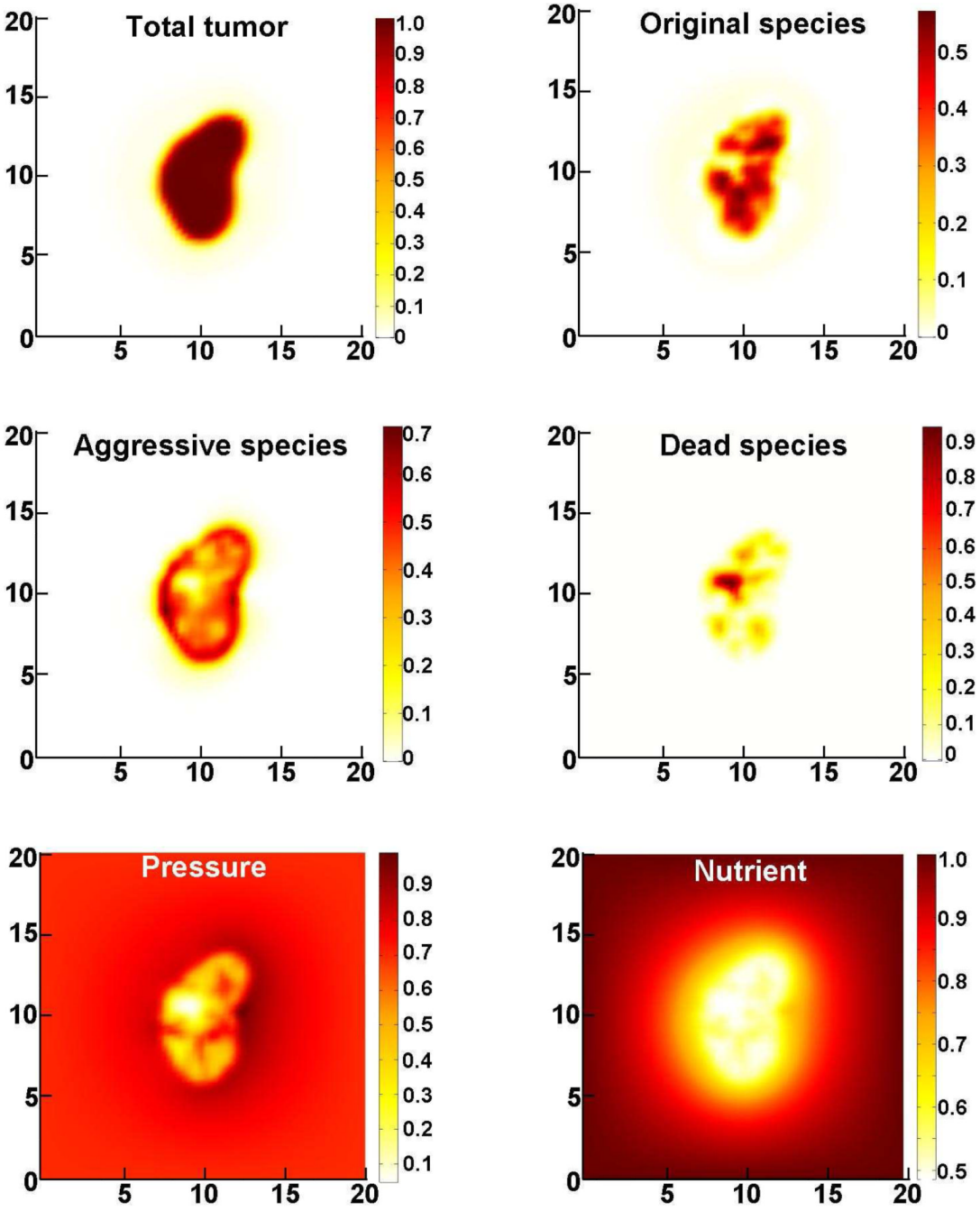

Fig. 18.

Slices of tumor (plane $x = 10$) with two viable cell species at time $t = 36$. The aggressive species, which has by this time situated itself via chemotaxis mainly on the periphery of the tumor, has optimal access to cell substrates. Since this species is the determinant of the overall morphology due to its combined higher proliferation and migratory capacity, it effectively minimizes the morphological instability of the overall tumor due to diffusion gradients of nutrient and oxygen. Color coding: magnitude. (Unit length = 100 μ*m*).

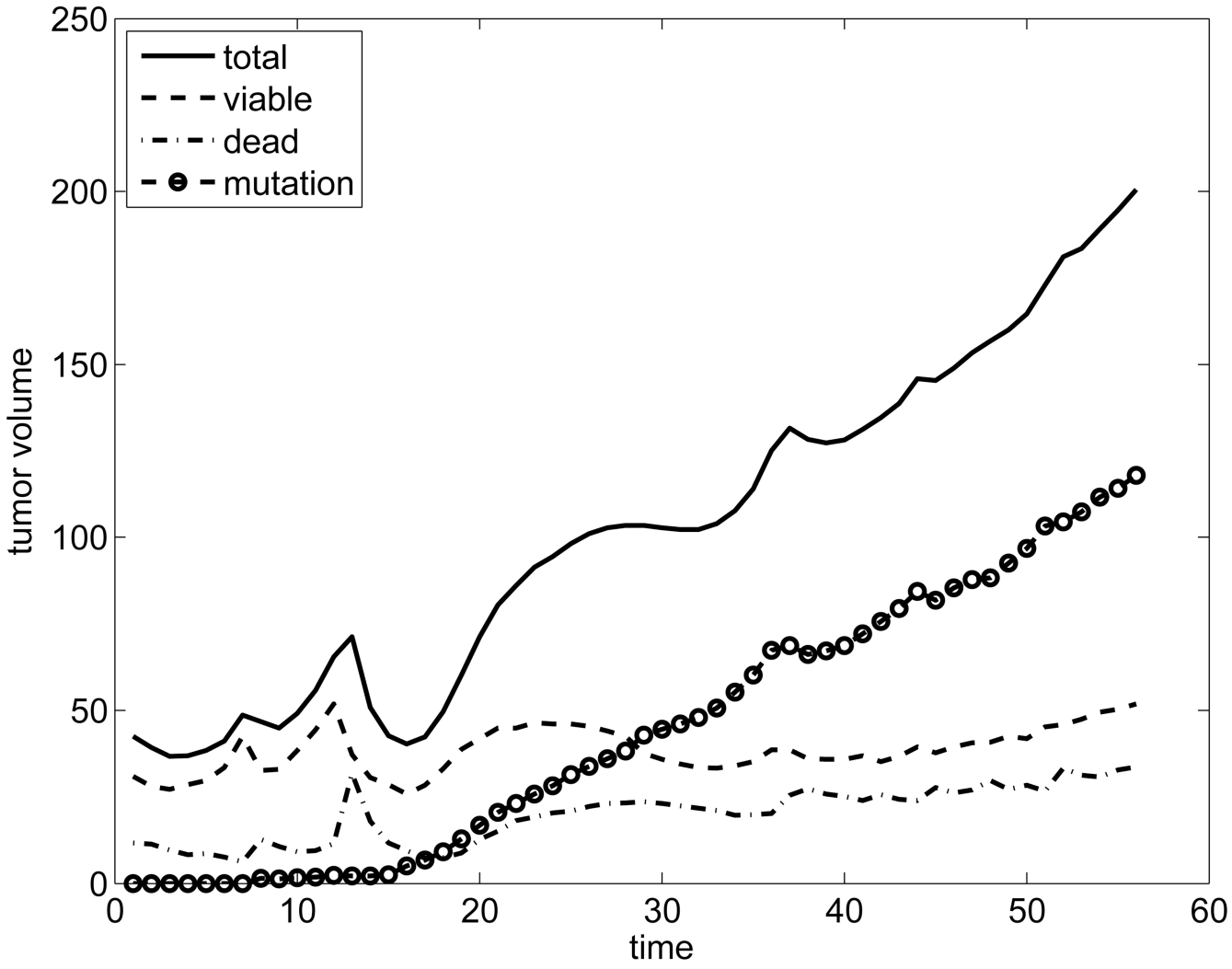

Fig. 19.

Tumor with two viable cell species. The proportion of aggressive species increases uniformly over time, while the original viable species remains stable (unit = 0.001 mm^3). The periods of vessel shutdown and consequent tumor mass regression are shorter compared to the base case (Figure 13).

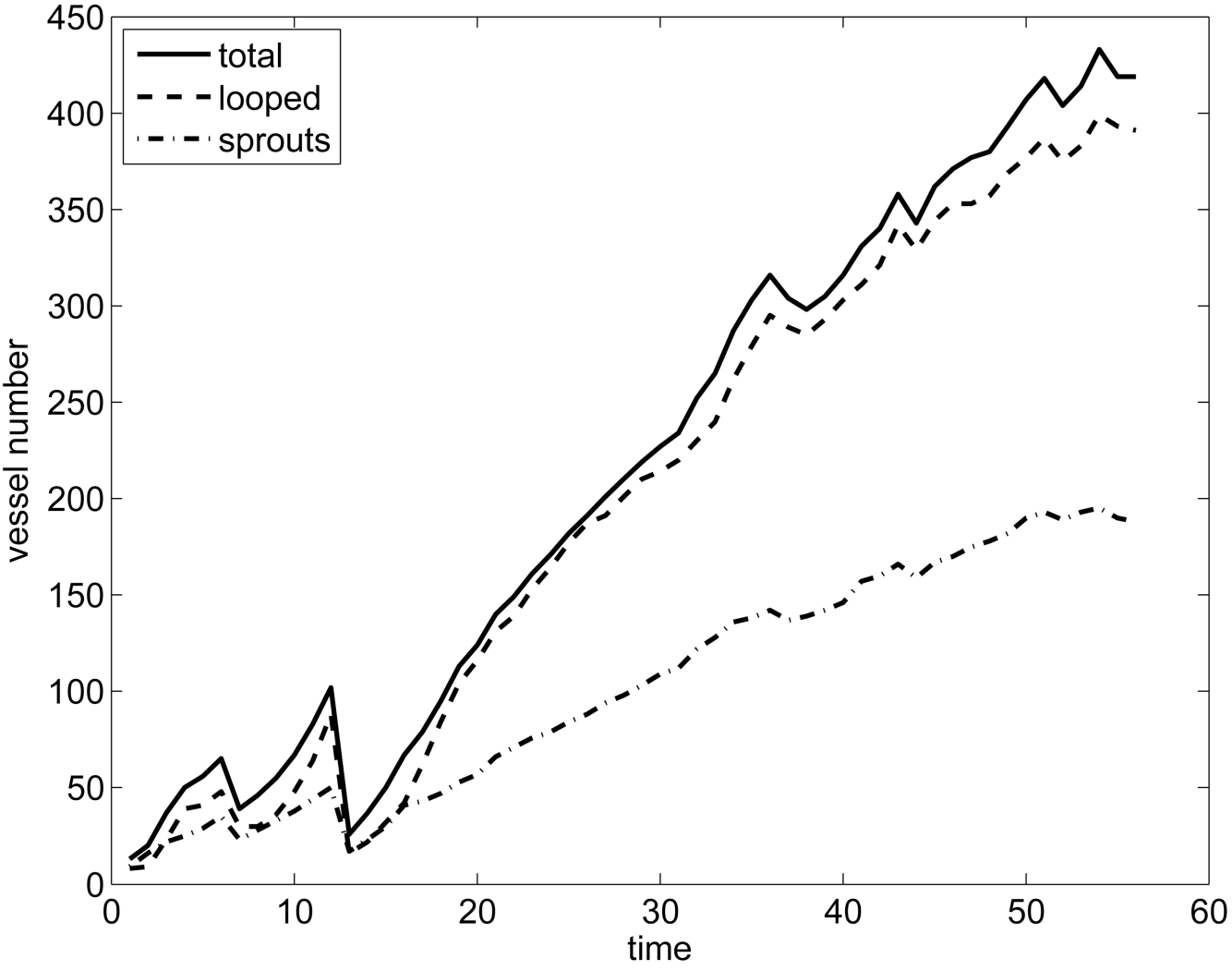

Fig. 20.
Tumor with two viable cell species. The number of vessel sprouts indicates a roughly linear increase corresponding to the more stable tumor volume growth.

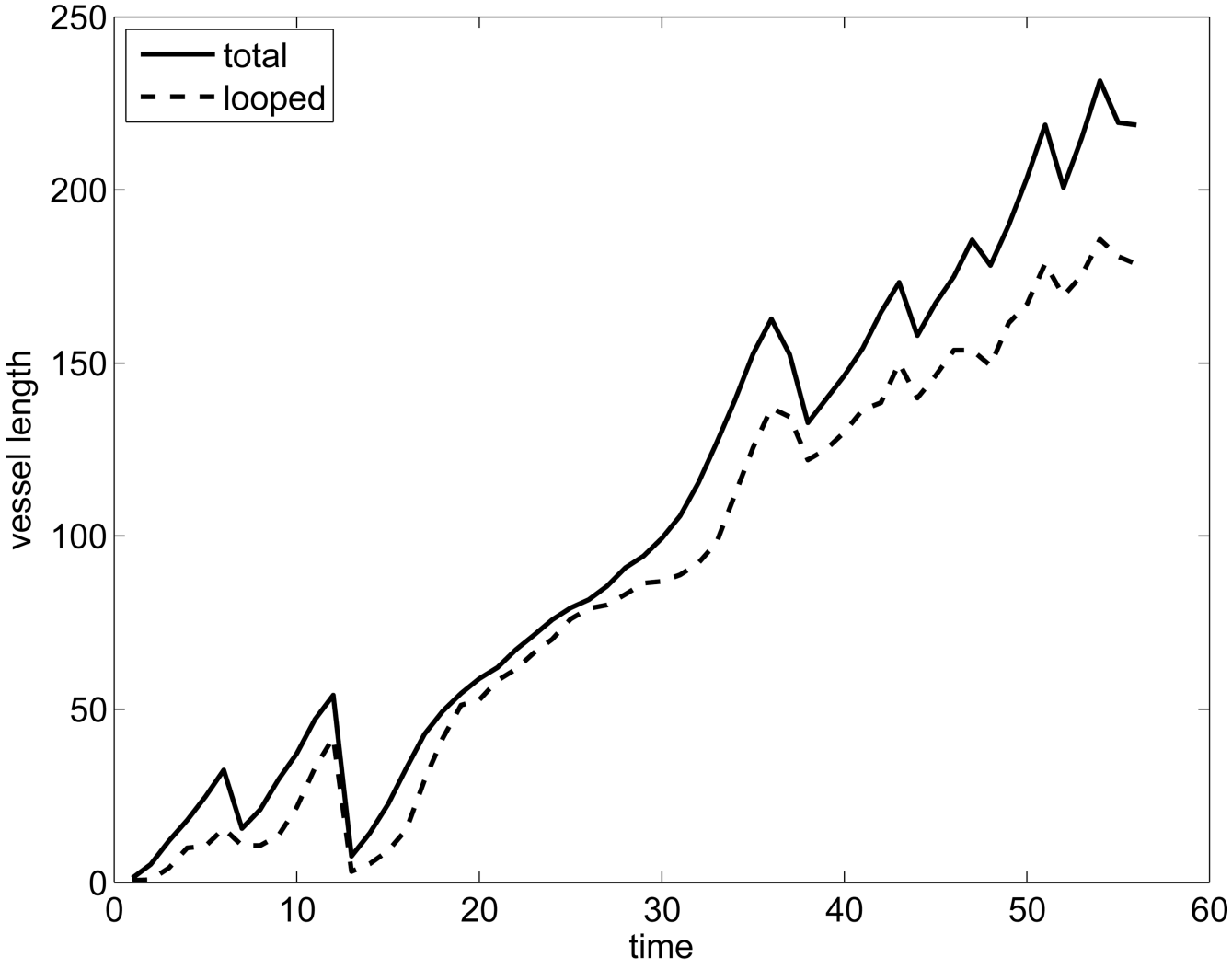

Fig. 21.
Tumor with two viable cell species. The total length of conducting vasculature increases roughly linearly with time (unit = 100 μm).

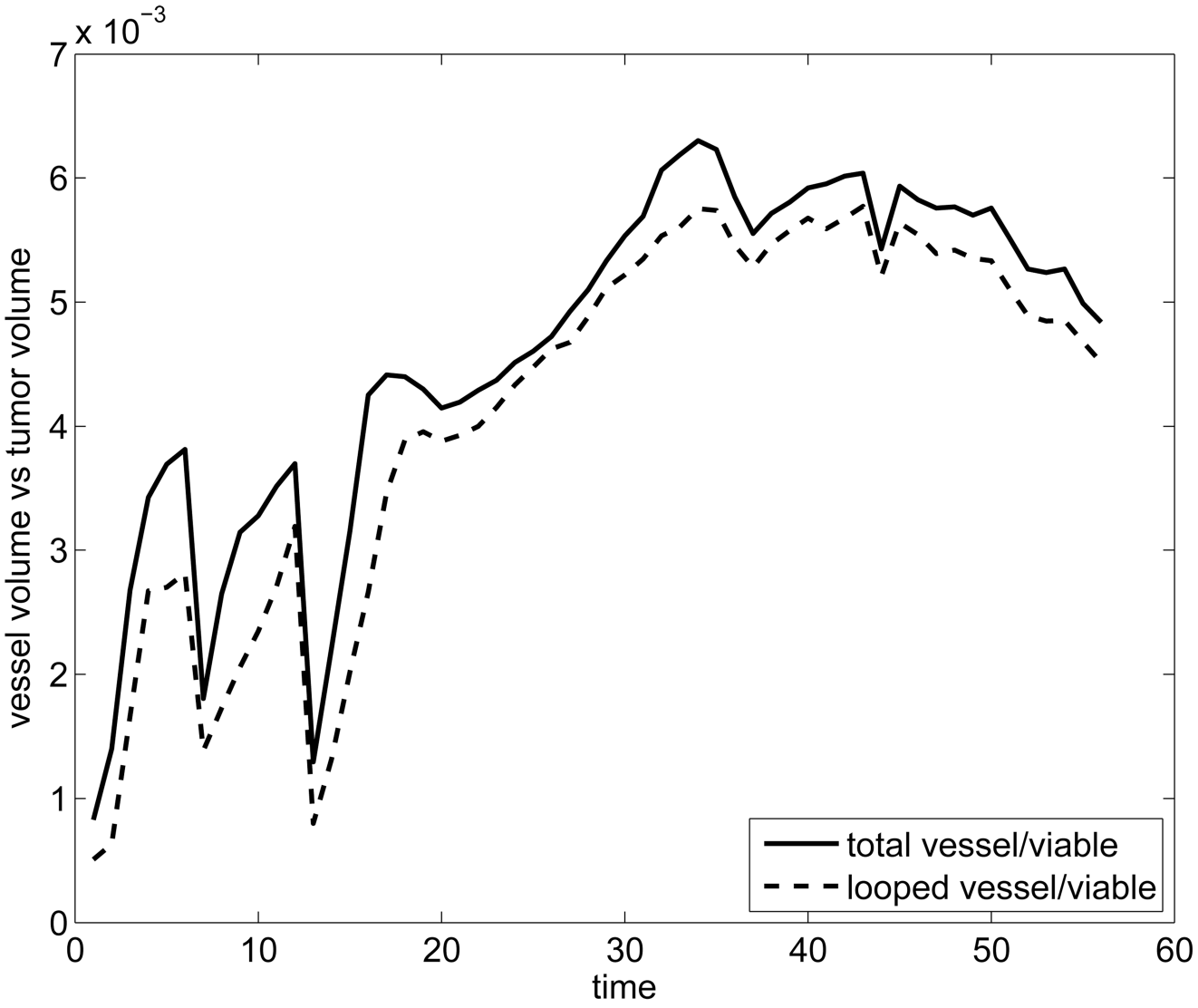

Fig. 22.

Tumor with two viable cell species. The vessel volume per viable tumor volume seems to reach a maximum for a longer period of time as compared to the base case with vessel shutdown, as a result of reduced tumor fragmentation. The sharp drops indicate periods of vessel regression.

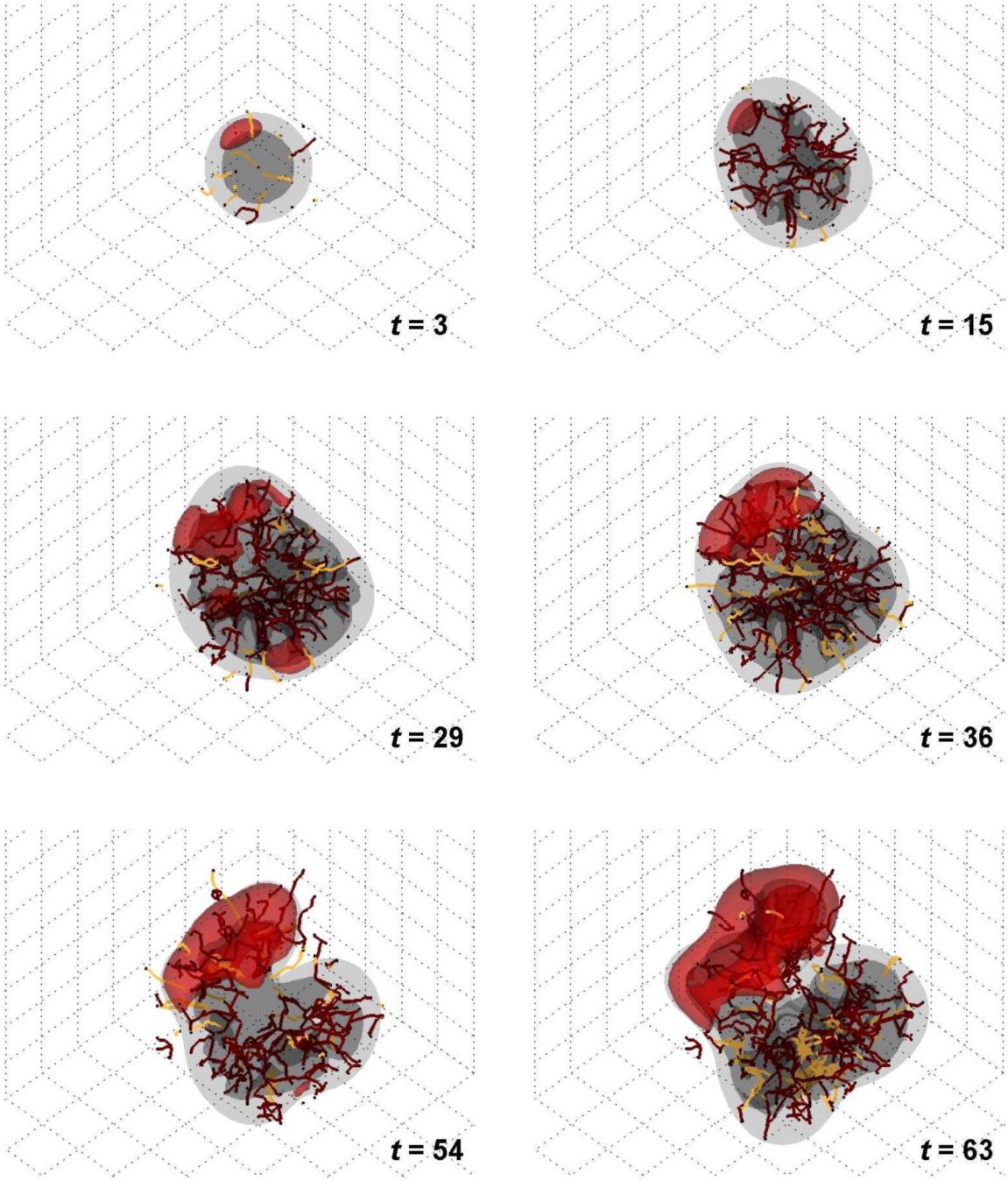

Fig. 23.

Tumor with mutation that activates chemotaxis only. Upregulation of chemotaxis through a secondary mutated species (red) in regions of insufficient cell substrates. The tumor morphology is substantially more unstable compared to the case when the secondary species also had higher proliferation and cell substrate uptake. The two viable species essentially compete for the limited cell substrates in the microenvironment, with the mutated species collecting towards the top part of the tumor. Viable tumor tissue (gray color) is shown in 3-D contours representing density values of 0.1, 0.2, and 0.6 (min.: 0.0; max.: 1.0). Conducting vessels: brown; non-conducting: yellow. Time unit = 1 day. (Grid length = 200 μ*m*).

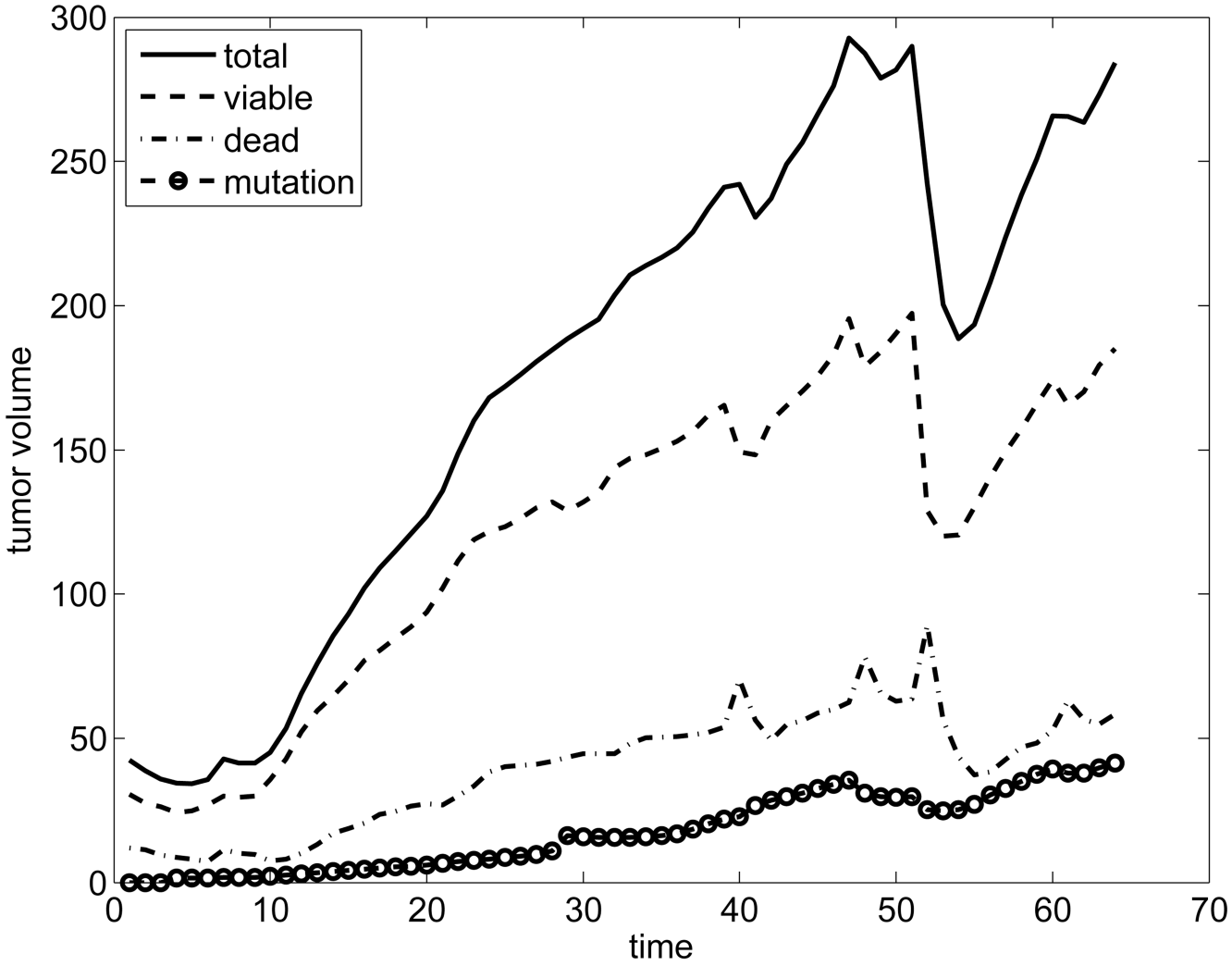

Fig. 24.
The volume of the mutated species (with the chemotactic phenotype) remains small as a percentage of the total tumor volume for the simulation in Fig. 23 (unit = 0.001 mm^3).

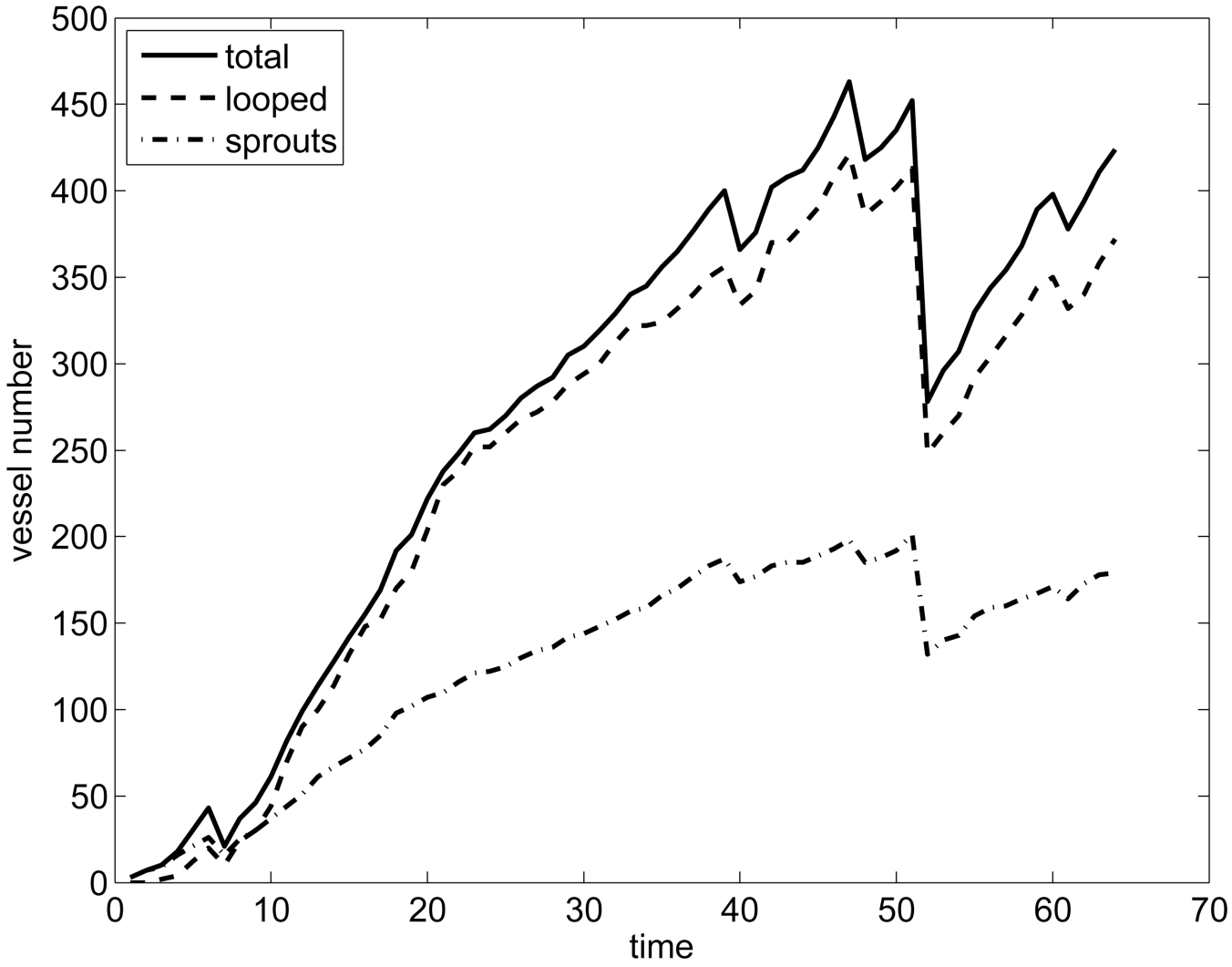

Fig. 25.
The number of new vessels increases smoothly over an initial period of time for the simulation in Fig. 23, and reflects the vessel shutdown episode at $t = 51$.

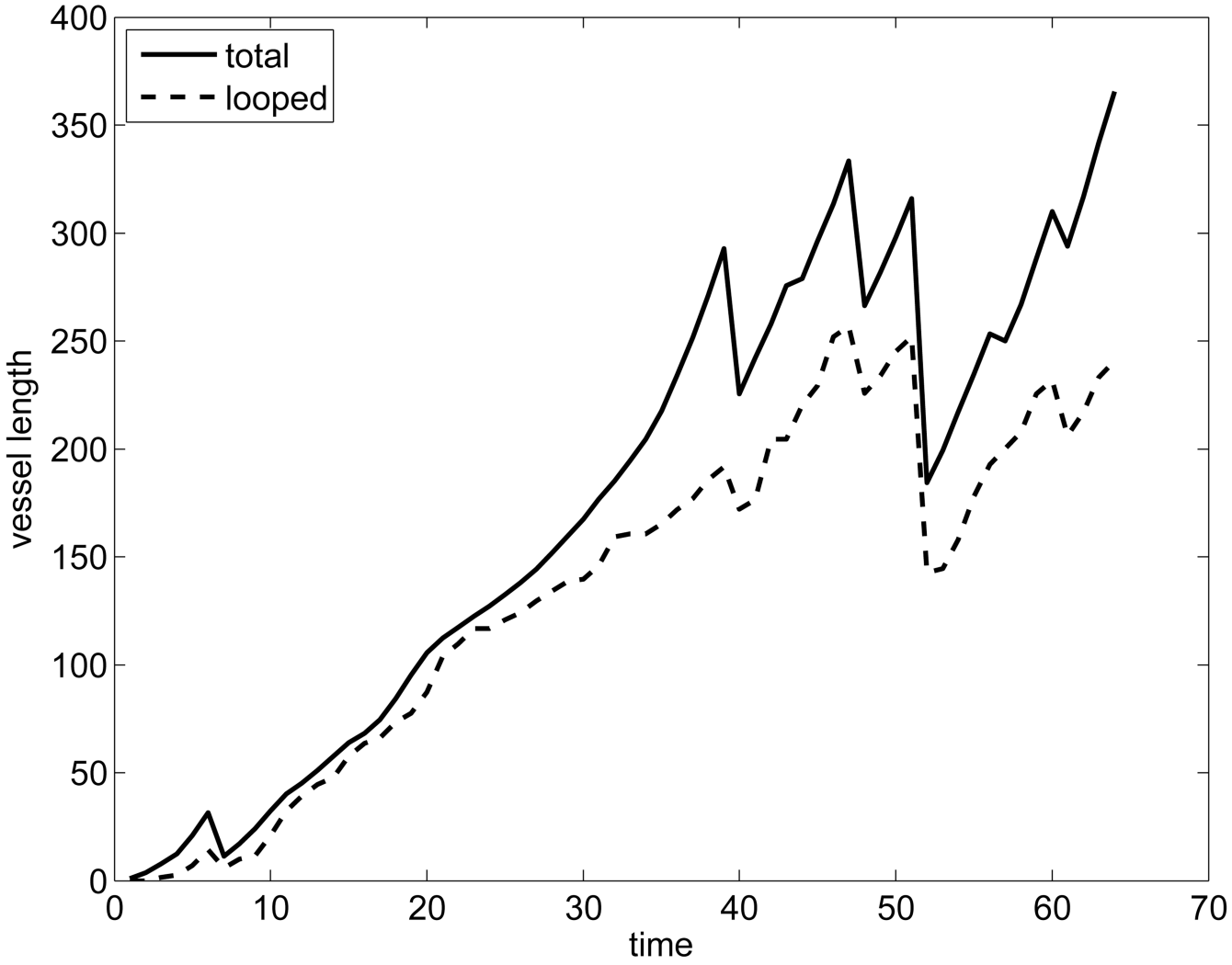

Fig. 26.

For the simulation in Fig. 23, the length of conducting vessels initially increases more smoothly as a function of time (unit = 100 μm) compared to the base case with vessel shutdown.

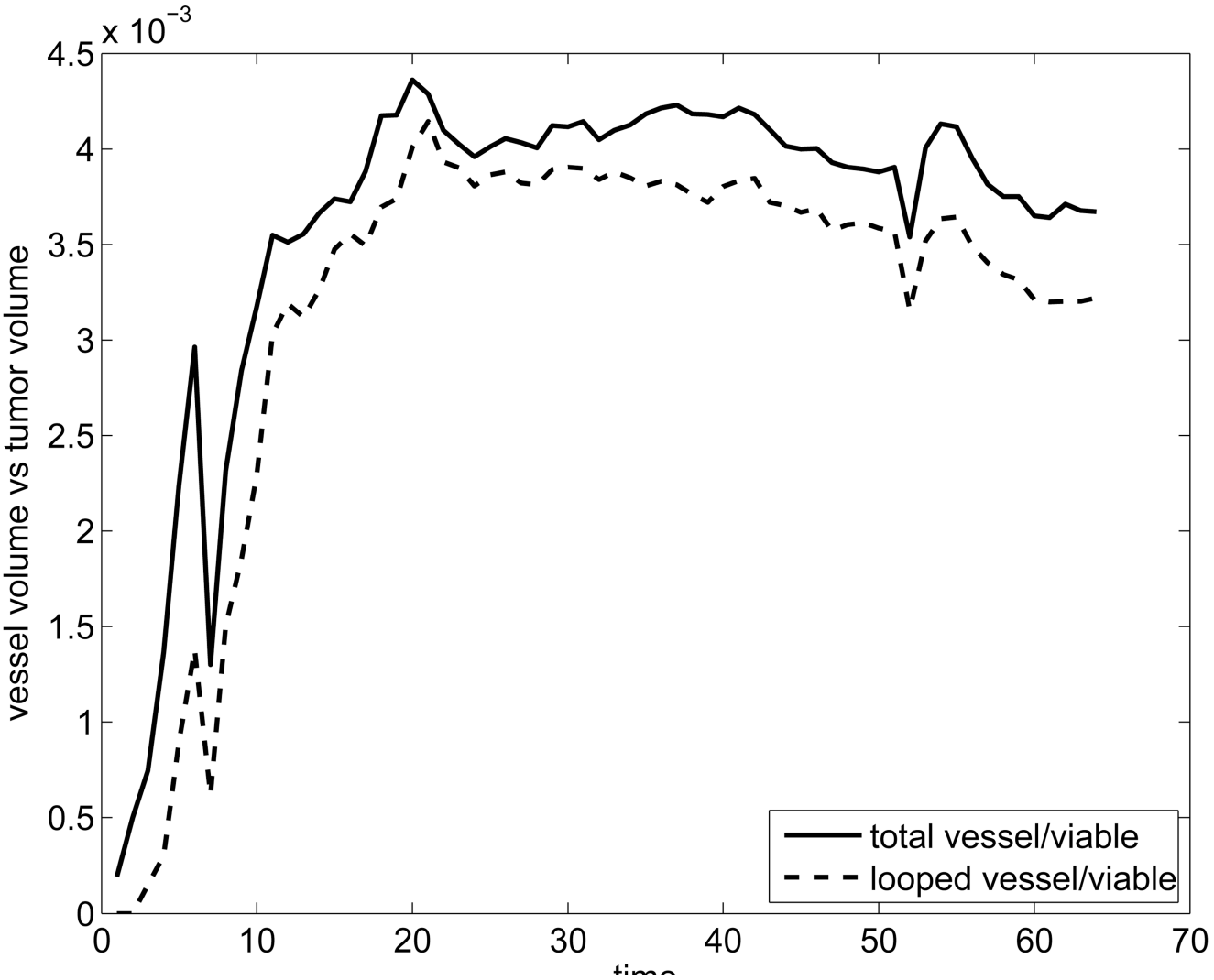

Fig. 27.
Vessel volume per viable tumor volume for the simulation in Fig. 23. The ratio stabilizes at a range above 3×10^{-3}.

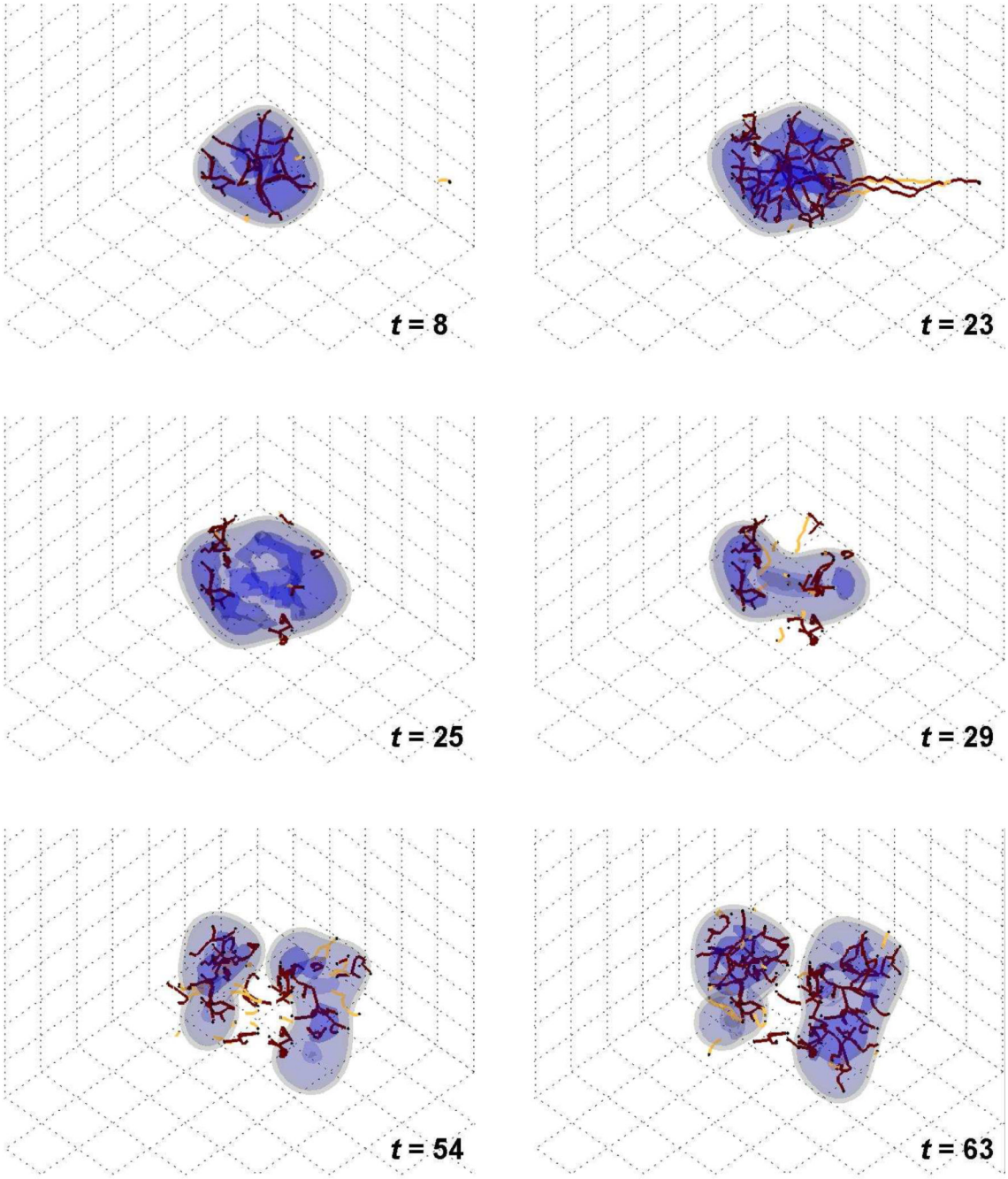

Fig. 28.

Tumor with one viable species, with upregulation of chemotaxis in regions of insufficient cell substrates. This condition produces the most unstable tumor morphology of all the cases studied, with tumor cluster-like fragmentation enabling better access to cell substrates in the surrounding (vascularized) host environment. Viable tumor tissue (blue color) is shown in 3-D contours representing density values of 0.1, 0.2, and 0.6 (min.: 0.0; max.: 1.0); complete absence of viable tissue is shown in gray. Conducting vessels: brown; non-conducting: yellow. Time unit = 1 day. (Grid length = 200μ*m*).

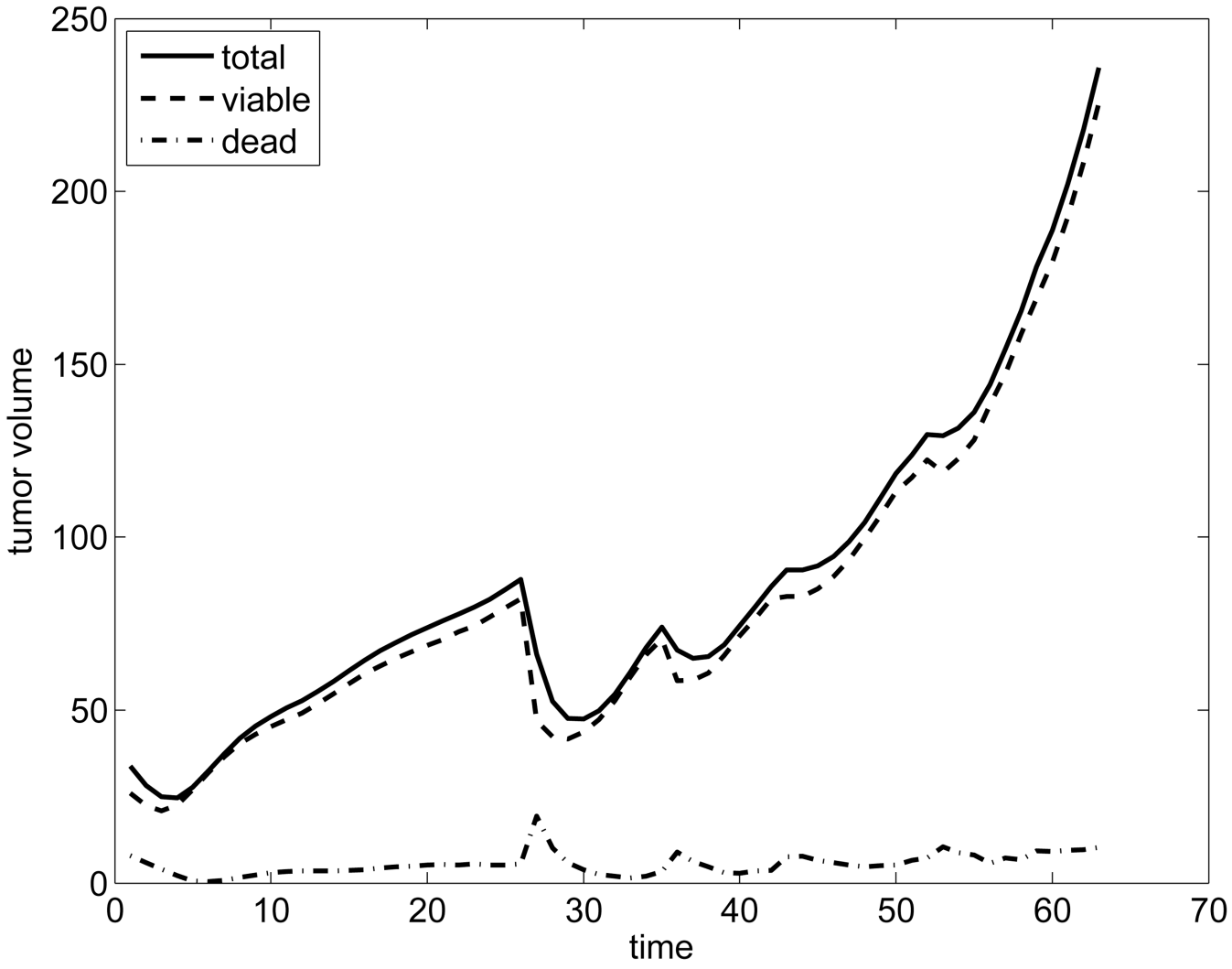

Fig. 29.
When all tumor cells have a chemotactic phenotype, the proportion of viable cells is the highest (unit = 0.001 mm^3).

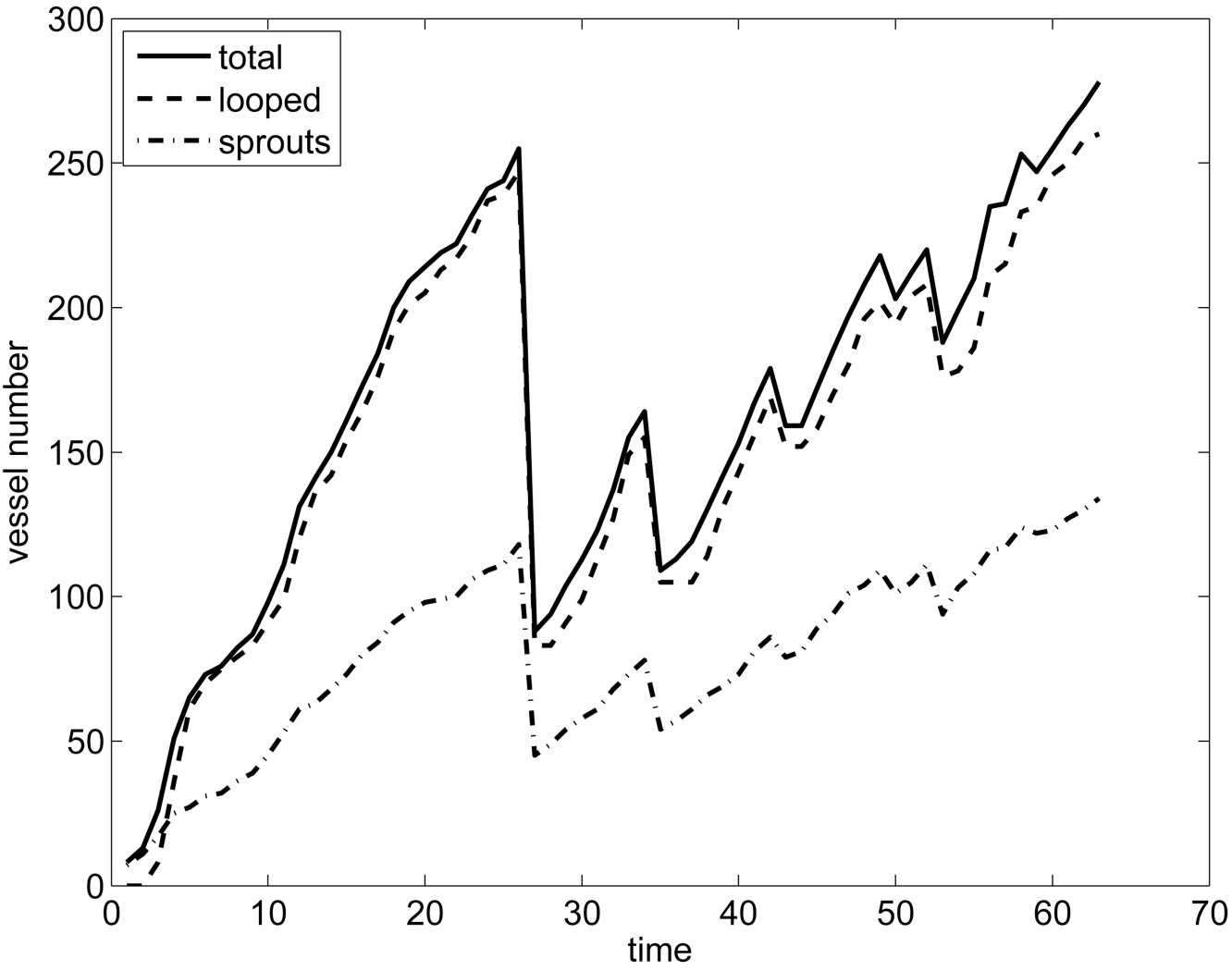

Fig. 30.
The number of new vessels dramatically reflects the shrinking and break-up of the tumor mass during episodes of vessel shutdown for the simulation in Fig. 28.

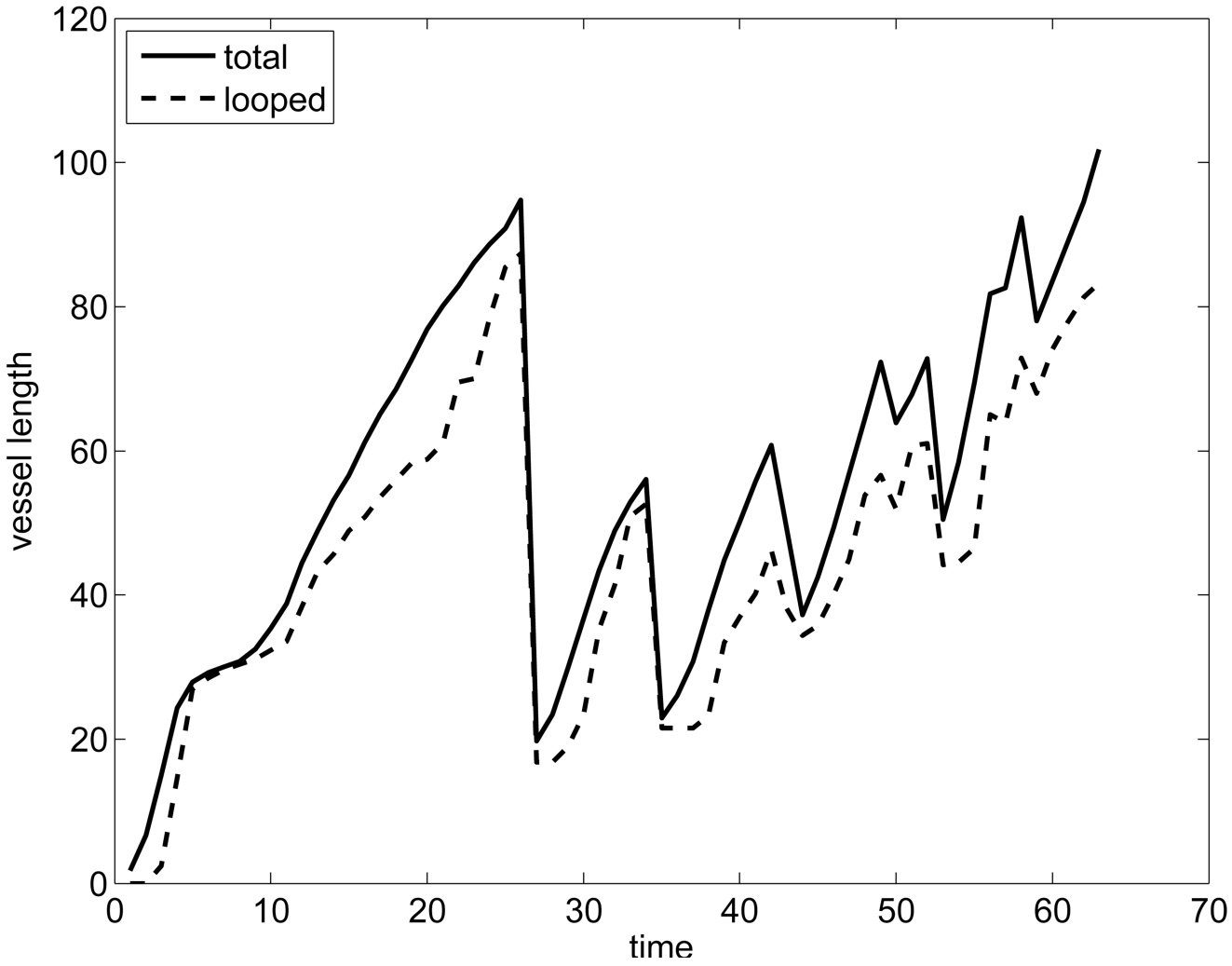

Fig. 31.
The overall length of conducting vessels varies over time as a function of the episodes of vessel shutdown (unit = 100 μm) for the simulation in Fig. 28.

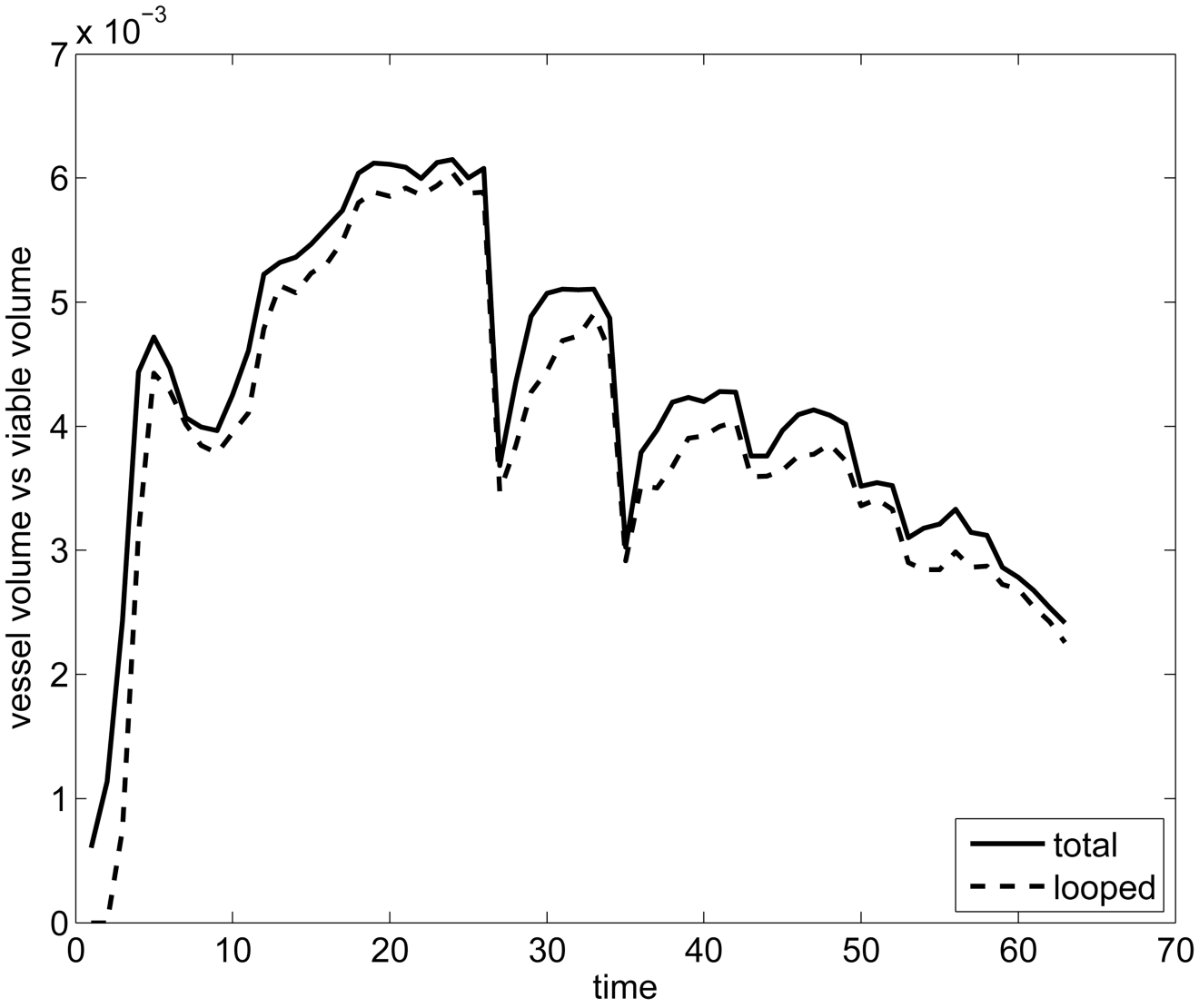

Fig. 32.
Vessel volume per viable tumor volume for the simulation in Fig. 28. The ratio is non-monotone and tends to the lowest value of all the cases studied.

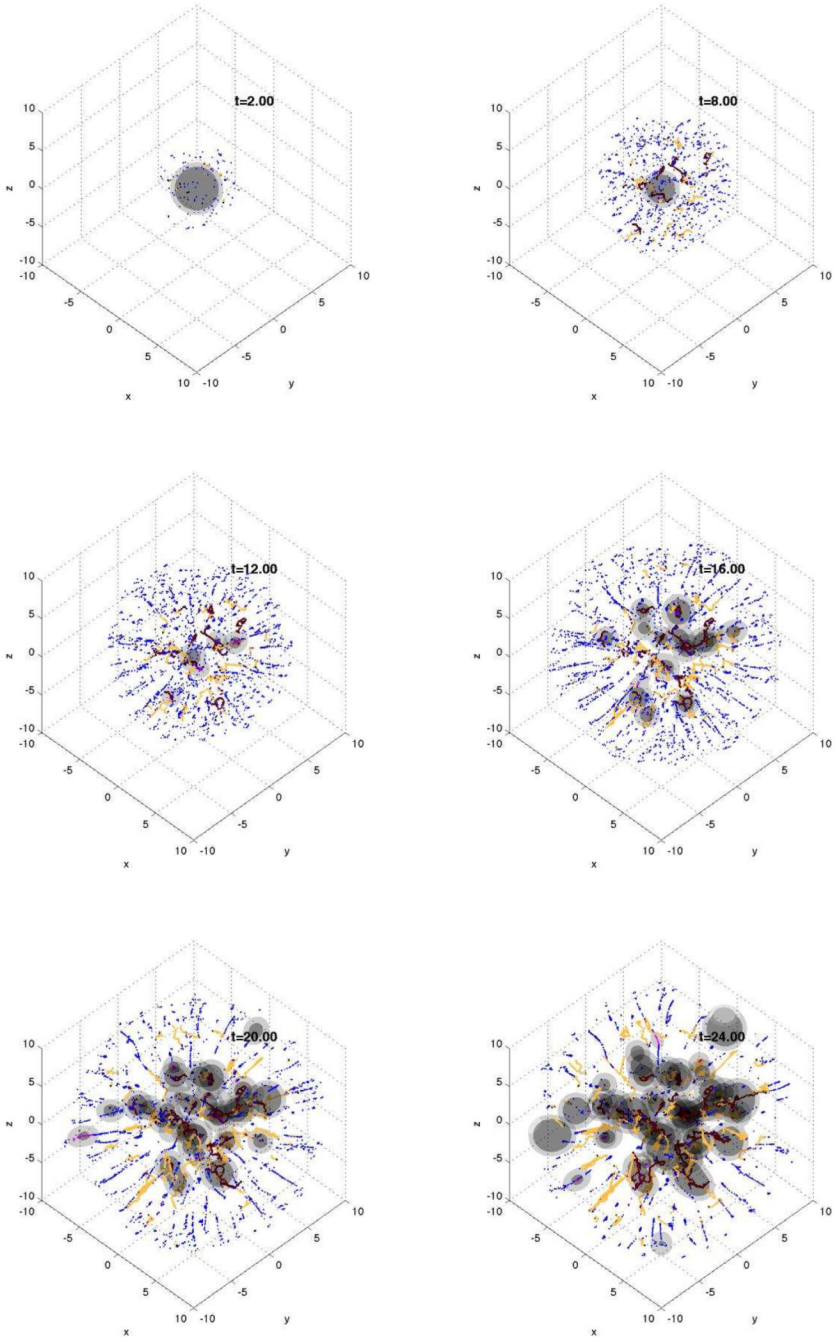

Fig. 33.

Evolution of a vascularized tumor using a hybrid continuum-discrete model for tumor cells. Discrete cells (dots) are released from hypoxic regions of the continuous tumor regions (gray surfaces). Discrete cells are converted back to continuum volume fractions when their density is sufficiently large. Vessel sprouts (light lines) and newly formed vessels (dark lines) releasing oxygen and nutrients (dark) are shown. The infiltrating cells form a palisading pattern as they invade the surrounding healthy tissue, where levels of oxygen and nutrient are higher, as is observed to occur *in vivo* in regions where neo-vascularization has not yet occurred (Bearer et al., 2009). Time unit = 1 day. (Grid unit = 200μ*m*).

Table 1

Nondimensional parameters (as defined in Wise et al. (2008) used in the avascular tumor simulation in Fig. 4.

$\nu_P^H = \bar{\nu}_P^H / \bar{\nu}_U$	0.5	$\nu_P^T = \bar{\nu}_P^T / \bar{\nu}_U$	0.0
$D_H = \bar{D}_H / \bar{D}_T$	1.0	$n_N = \bar{n}_N / \bar{n}_\infty$	0.4
$\lambda_A = \bar{\lambda}_A / \bar{\lambda}_M$	0.0	$\lambda_N = \bar{\lambda}_N / \bar{\lambda}_M$	3.0
$\lambda_L = \bar{\lambda}_L / \bar{\lambda}_M$	1.0	$\gamma \approx \tilde{\gamma} / (6\sqrt{2})$	0.0
M	10.0	ε	0.1

Table 2

Nondimensional parameters of the tumor species used for the vascularized tumor simulations shown in Figs. 5 through 32.

λ_V^m	1.0	n_V^*	0.5
λ_V^n	300	λ_V^a	0.0
λ_D^l	1.5	M	10
ε	0.1	$\tilde{\gamma}$	0.0
ν_V^u	10	D_{H}	1.0
χ	10	C_{mut}	10

Table 3

Nondimensional angiogenesis parameters used for the vascularized tumor simulations shown in Figs. 5 through 32.

ν_{ves}	20	D_c	2
β_d	6	S_c	10^3
c_{sat}	1	r_{ves}	0.4
ε_{ves}	0.1	C_{ves}	1
C_{chemo}	5	C_{hapto}	0
σ	$\sqrt{2}$	p_{crush}	0.5

Table 4

Nondimensional parameters used for the discrete tumor cell simulation shown in Fig. 33.

$C_{extract}$	0.5	$C_{deposit}$	2.0
D_{chemo}	20	D_{hapto}	8
D_v	2	C_{disc}	1